Fall 1-31-2015

Optical properties of strain-engineered multilayer Si/SiGe nanostructures

Selina Akter Mala
New Jersey Institute of Technology

Copyright Warning & Restrictions

The copyright law of the United States (Title 17, United States Code) governs the making of photocopies or other reproductions of copyrighted material.

Under certain conditions specified in the law, libraries and archives are authorized to furnish a photocopy or other reproduction. One of these specified conditions is that the photocopy or reproduction is not to be "used for any purpose other than private study, scholarship, or research." If a, user makes a request for, or later uses, a photocopy or reproduction for purposes in excess of "fair use" that user may be liable for copyright infringement,

This institution reserves the right to refuse to accept a copying order if, in its judgment, fulfillment of the order would involve violation of copyright law.

Please Note: The author retains the copyright while the New Jersey Institute of Technology reserves the right to distribute this thesis or dissertation

Printing note: If you do not wish to print this page, then select "Pages from: first page # to: last page #" on the print dialog screen

ABSTRACT

OPTICAL PROPERTIES OF STRAIN-ENGINEERED MULTILAYER Si/SiGe NANOSTRUCTURES

by
Selina Akter Mala

The long carrier radiative lifetimes in indirect band gap semiconductors such as crystalline Si (c-Si) and Ge impede the development of efficient light-emitting devices and lasers. Multilayer Si/SiGe nanostructures are considered to be the strong candidates for efficient and high-speed optoelectronic devices integrated into CMOS platforms. Since c-Si and Ge have a considerable lattice mismatch of ~ 4.2%, $Si/Si_{1-x}Ge_x$ ($x < 0.5$) nanostructures in the form of nano-layers (NLs) or cluster multilayers (CMs) modify the band structure and create non-uniform strain distribution. Engineering of $Si/Si_{1-x}Ge_x$ nanostructures with the predicted composition and interface abruptness, which controls spatial separation between electrons and holes and carrier radiative recombination rate, is critical in producing the desired fast and efficient photoluminescence (PL) peaked around 0.8-0.9 eV. This study investigates the structural, optical, and thermal properties of $Si/Si_{1-x}Ge_x$ nanostructures with different layer thicknesses, Ge compositions, and SiGe heterointerface abruptness.

A comprehensive experimental and theoretical analysis of Raman scattering in various $Si/Si_{1-x}Ge_x$ multilayered nanostructures with well-defined Ge composition (x) and layer thicknesses is presented. Using Raman and transmission electron microscopy data, Si/SiGe intermixing and strain are discussed and modeled. The studied samples exhibit significant dependence of the Raman scattering intensity on the excitation light penetration depth. Local temperature and thermal conductivity are calculated by

analyzing the measured Stokes and anti-Stokes Raman spectra, and the developed model of heat dissipation in the samples under an intense laser illumination is in a good agreement with the experiment. A correlation is found between the SiGe/Si volume fraction ratio and thermal conductivity, which is explained and suggestions are made of applications of the developed model in the field of thermoelectric, electronic, and optoelectronic devices.

In this thesis, PL measurements are focused on specifically designed $Si/Si_{1-x}Ge_x$ nanostructures with a single 3-5 nm thick $Si_{1-x}Ge_x$ layer with $x \approx 8\%$ incorporated into $Si/Si_{0.6}Ge_{0.4}$ CMs. Under pulsed laser excitation, the PL decay associated with the $Si_{0.92}Ge_{0.08}$ NL is found to be nearly a 1000 times faster compared to that in $Si/Si_{0.6}Ge_{0.4}$ CMs, and the SiGe NL PL intensity does not saturate as a function of excitation energy density up to 50 mJ/cm^2. These dramatic differences in the observed PL properties are attributed to the difference in the structures of the Si/SiGe NL and CM heterointerfaces. A model considering Si/SiGe heterointerface composition and explaining the fast and slow time-dependent recombination rates is proposed and found to be in excellent agreement with the experimental data.

OPTICAL PROPERTIES OF STRAIN-ENGINEERED MULTILAYER Si/SiGe NANOSTRUCTURES

by
Selina Akter Mala

A Dissertation
Submitted to the Faculty of
New Jersey Institute of Technology
In Partial Fulfillment of the requirements for the degree of
Doctor of Philosophy in Electrical Engineering

Helen and John C. Hartmann Department of
Electrical and Computer Engineering

January 2015

APPROVAL PAGE

OPTICAL PROPERTIES OF STRAIN-ENGINEERED MULTILAYER Si/SiGe NANOSTRUCTURES

Selina Akter Mala

Dr. Leonid Tsybeskov, Dissertation Advisor — Date
Professor of Electrical and Computer Engineering, NJIT

Dr. Haim Grebel, Committee Member — Date
Professor of Electrical and Computer Engineering, NJIT

Dr. Durgamadhab Misra, Committee Member — Date
Professor of Electrical and Computer Engineering, NJIT

Dr. Marek Sosnowski, Committee Member — Date
Professor of Electrical and Computer Engineering, NJIT

Dr. Andrei Sirenko, Committee Member — Date
Professor of Physics, NJIT

BIOGRAPHICAL SKETCH

Author: Selina Akter Mala

Degree: Doctor of Philosophy

Date: January, 2015

Undergraduate and Graduate Education:

- Doctor of Philosophy in Electrical Engineering
  New Jersey Institute of Technology, Newark, NJ, 2015

- Bachelor of Science in Electrical Engineering
  Bangladesh University of Engineering and technology, Dhaka, Bangladesh, 2006

Major: Electrical Engineering

Presentations and Publications:

- Journal Publications

Selina A. Mala, Leonid Tsybeskov, David J. Lockwood, Xiaohua Wu, and Jean-Marc Baribeau, "Raman scattering in Si/SiGe nanostructures: chemical composition, strain, intermixing, and heat dissipation," Journal of Applied Physics, 116, 014305, 2014.

Selina A. Mala, Leonid Tsybeskov, David J. Lockwood, Xiaohua Wu, and Jean-Marc Baribeau, "Fast and intense photoluminescence in a SiGe nano-layer embedded in multilayers of Si/SiGe clusters," Applied Physics Letters, 103, 033103, 2013.

Selina A. Mala, Leonid Tsybeskov, David J. Lockwood, Xiaohua Wu, and Jean-Marc Baribeau, "Carrier recombination in tailored multilayer $Si/Si_{1-x}Ge_x$ nanostructures," Physica B: Condensed Matter, 453, 29, 2014.

- Conference Proceedings Publications

Selina A. Mala, Leonid Tsybeskov, Jean-Marc Baribeau, Xiaohua Wu, and David J. Lockwood, "Quantitative analysis of Raman spectra in Si/SiGe nanostructures," Material Research Society Proceedings, 1510, 2013.

Leonid Tsybeskov, H.-Y. Chang, Selina A. Mala, Ted I. Kamins, Xiaohua Wu, and David J. Lockwood, "Structural and optical properties of Si/Ge nanowire heterojunctions," ECS Transactions, 53, 2013.

David J. Lockwood, Xiaohua Wu, Jean-Marc Baribeau, Selina A. Mala, Nikhil Modi, and Leonid Tsybeskov, "Fast and slow light-emitting silicon-germanium nanostructures," ECS Transactions, 53, 2013.

- Oral Conference Presentation

Selina A. Mala, Leonid Tsybeskov, David J. Lockwood, Jean-Marc Baribeau, and Xiaohua Wu, "Evaluating heat dissipation in Si/SiGe nanostructures using Raman scattering," American Physical Society Meeting, Baltimore, MD, March 2013.

- Poster Conference Presentations

Selina A. Mala, Leonid Tsybeskov, David J. Lockwood, Xiaohua Wu, and Jean-Marc Baribeau, "Carrier recombination in tailored multilayers $Si/Si_{1-x}Ge_x$ nanostructures," Graduate Studies Association Research Day, Newark, NJ, October 2014.

Selina A. Mala, Leonid Tsybeskov, David J. Lockwood, Xiaohua Wu, and Jean-Marc Baribeau, "Quantitative analysis of Raman spectra in $Si/Si_{1-x}Ge_x$ nanostructures," Graduate Studies Association Research Day, Newark, NJ, October 2013.

Selina A. Mala, Leonid Tsybeskov, Jean-Marc Baribeau, Xiaohua Wu, and David J. Lockwood, "Quantitative analysis of Raman spectra in Si/SiGe nanostructures," Material Research Society Proceedings, Boston, MA, November 2012.

To my parents,

my sister Dr. Nilufa Rahim,

who made everything possible

ACKNOWLEDGMENT

First and foremost, I would like to sincerely thank my dissertation advisor, Dr. Leonid Tsybeskov, for all his support, guidance, and encouragement. I can remember that he used to say “good” every time after seeing my work. This “one word” has given me a huge inspiration throughout this journey. His patience and understanding coupled with his experience have contributed to the successful completion of my studies. Ever since, Dr. Leonid Tsybeskov has supported me not only by providing teaching and research assistantship over five years, but also academically and emotionally through the rough road to finish this thesis. He helped me to come up with the thesis topic and guided me over the years of development. During the most difficult times when writing this thesis, he gave me the moral support and the freedom I needed to move on.

I would like to thank Dr. Haim Grebel, Dr. Durga Misra, Dr. Andrei Sirenko, and Dr. Marek Sosnowski for serving as members of my dissertation committee and their fruitful discussions. I am grateful to Dr. Andrei Sirenko for his thought-provoking advising in Raman scattering and Dr. Marek Sosnowski for his advising in SiGe growth techniques.

I would like to express my gratitude to our collaborators for providing the samples. I am ever grateful to Dr. David Lockwood and Dr. Jean-Mark Baribeau for their valuable comments and suggestions throughout this research.

I would like to thank my friend and colleague, Tazima Selim Chowdhury for her enormous support in this journey. I would like to thank my lab members, Dr. H.-Y. Chang, Dr. Nikhil Modi, and Xiaolu Wang for inspiring me all the way. I am grateful to Sumana Pai, Vani Vedula, Lipilekha Mukherjee, Lalithya Narla, and Priya Muralidharan

for their help and encouragement. I would like to especially thank my student, Mahjabin Alam. She has helped me at every step in difficult time.

Last, but not least, I am thankful to my parents for their tremendous and unconditional support. Their beliefs have given me the courage to achieve my dreams. I would like to thank my husband, Rahman Faizur Rafique for his support, understanding, and encouragement. I would like to express my heartfelt gratitude to my brothers-in-law, Abdul Jalil, Abdullah Ahmed, and Nasir Uddin Bhuyian for their support and encouragement throughout my journey. I am thankful to my sister, Nargis Akter and brothers, Nurul Amin and Zaed Ibne Rahim for their continuous inspiration and encouragement. I am always grateful to my lovable nephews and nieces, Sanjana, Sajid, Shayaan, Adiyaan, and Aleena for making my life colorful. I would like to especially thank to my younger sister, Faria Sharmin for being with me in time of need. She has given me the courage to face the toughest time of my life. I will never forget her contributions. I would like to express my deepest gratitude to my elder sister, Nilufa Rahim for her constant guidance and encouragement. Thank you so much for your support and invaluable inspiration all the way.

TABLE OF CONTENTS

TABLE OF CONTENTS
(Continued)

LIST OF TABLES

LIST OF FIGURES

LIST OF FIGURES
(Continued)

Figures **Page**

LIST OF FIGURES
(Continued)

LIST OF FIGURES
(Continued)

Figures **Page**

LIST OF FIGURES
(Continued)

Figures **Page**

CHAPTER 1

INTRODUCTION

The development of a light emitter compatible with Si based complementary metal-oxide- semiconductor (CMOS) circuit technology and fast optical interconnects is important for the new generations of microprocessors and computers. During the last several decades, efficient light emission using silicon nanocrystals [1, 2], silicon/silicon dioxide superlattices (SLs) [3-5], erbium in silicon [6], iron disilicide [7], strained Ge on Si [8], and different forms of $Si/Si_{1-x}Ge_x$ nanostructures (NSs) [9] has been a topic of significant interest. Such $Si/Si_{1-x}Ge_x$ NSs with $0.1<x<0.5$ emit light at the desired optical communication wavelength of 1.3−1.55 μm spectral region, and they are compatible with standard CMOS processes. $Si/Si_{1-x}Ge_x$ NSs are extensively used in many devices including advanced transistors, photodetectors, electro-optical modulators, thermo-electric generators, and THz and near infra-red light emitters [9, 10].

The major problem in the growth of low-defect density $Si/Si_{1-x}Ge_x$ NSs is the 4.2% lattice mismatch between Si and Ge. This problem can be solved using $Si_{1-x}Ge_x$ nanometer-thick layers (NLs) with thicknesses below the strain-relaxation critical thickness and properly chosen composition x [10]. Another option is $Si/Si_{1-x}Ge_x$ cluster multilayers (CMs), where a higher Ge content x and critical thicknesses are possible due to a non-uniform strain distribution and diffused Si/SiGe heterointerfaces [11, 12]. Early work was mostly concentrated on introducing $Si/Si_{1-x}Ge_x$ NSs with $x \leq 0.2$ into the CMOS environment with the smallest number of defects and reduced strain [13]. Later, it was recognized that $Si/Si_{1-x}Ge_x$ NSs with x approaching 0.5 can provide additional advantages in charge carrier confinement, and they can be grown in the form

of NLs, clusters, and cluster multilayers with a low density of structural defects [14]. This type of growth (similar to Stranski-Krastanov growth) typically requires a growth temperature of ~550−600 ^{o}C, and it can result in quite significant Si/SiGe intermixing at the heterointerface [14]. In addition, these $Si/Si_{1-x}Ge_x$ NSs with x approaching 0.5 produce a complex distribution of strain, and it affects heat conductance, which needs to be enhanced for electronic and photonic devices and reduced for thermoelectric devices [15].

In this dissertation, optical and thermal properties of multilayer $Si_{1-x}Ge_x$ ($0.2<x<0.5$) NSs combined with structural analysis are discussed. The samples are grown by molecular beam epitaxy (MBE) at National Research Council (NRC) of Canada. The first part of this study will focus on comprehensive analyses of Raman spectra in three different types of samples with progressively increasing Ge content: two-dimensional (2D) planar SiGe SLs, three-dimensional (3D) non-uniform SiGe CMs, and a single SiGe NL grown on top of SiGe CMs. In the following part of this study, continuous-wave (CW) and time-resolved photoluminescence (PL) measurements are performed to investigate in detail the recombination dynamics in the $Si/Si_{1-x}Ge_x$ samples. This dissertation will propose a novel design of Si/SiGe NSs to reduce the carrier radiative recombination lifetime and increase the PL quantum efficiency.

Chapter 2 discusses the previously published results focusing on growth techniques and mechanisms as well as structural, optical, and thermal properties of Si/SiGe NSs. Chapter 3 describes the details of $Si/Si_{1-x}Ge_x$ samples grown by MBE used in the present work. The experimental methods, optical characterization setup, and details of the measurement procedures are presented in Chapter 3.

Chapter 4 will present a detailed discussion of the experimental results. Raman and PL measurements are performed for $Si/Si_{1-x}Ge_x$ NSs with different compositions, dimensions, and heterointerface abruptness. The first part of Chapter 4 has focused on qualitative explanations of the observed Raman features in first-order, second-order, and low-frequency spectral ranges followed by quantitative analysis of the Raman peak's position, spectral shape, and intensity. The laser beam heating of the samples during Raman measurements, heat dissipation, and details of anti-Stokes Raman spectra are also discussed. In the following part of Chapter 4, CW and time-resolved PL measurements in the samples containing a $Si_{1-x}Ge_x$ NL with $x \approx 8\%$ sandwiched between $Si_{1-x}Ge_x$ clusters with $x \leq 40\%$ are presented and discussed. The PL measurements find that both the SiGe NL and SiGe clusters show non-exponential PL decay but with more than a 1000 times difference in the PL lifetimes. The results show that the shorter lifetime PL intensity (SiGe NLs) does not saturate as a function of excitation energy density. This chapter presents a quantitative model of carrier recombination in Si/SiGe NSs explaining the predicted and experimentally observed fast and intense PL signal.

Finally, Chapter 5 provides a summary of this research work.

CHAPTER 2

Si/SiGe NANOSTRUCTURES

The high quality epitaxial growth of SiGe layers on Si substrate offers an opportunity to realize novel devices such as heterojunction bipolar transistor (HBT), resonant tunneling diode (RTD), and high mobility two-dimensional hole gas (2DHG) [16-19]. In this chapter, the growth technique used for Si/SiGe nanostructures (NSs) and basic concepts of the growth modes will be reviewed from the literature. Characterization techniques to study the properties of Si/SiGe NSs will be discussed extensively.

2.1 Growth Techniques of Si/SiGe Nanostrustures

There are two techniques for the epitaxial growth of high quality SiGe films on the Si substrate: solid source molecular beam epitaxy (SS MBE) and ultrahigh vacuum chemical vapor deposition (UHV CVD). UHV CVD is the dominant growth process in production and industrial environments due to the low particulate density. The particulate density must be close to zero for high yield CMOS or bipolar production. UHV CVD provides uniformity and reproducibility for commercial applications. MBE, however is an outstanding research technique. The samples studied in this dissertation are grown by MBE.

2.1.1 Molecular Beam Epitaxy

MBE is the mostly used laboratory growth process for the growth of Si/SiGe and III-V heterostructures [10, 20]. In a typical MBE deposition process, a molecular or atomic beam is formed by heating the material that needs to be deposited using a cell. The cell is known as effusion (or Knudsen) cell. Mechanical shutters are used to select the material which will be absorbed by the sample surface (adatoms) and control the fluxes of the molecular beam. The types of adatoms, the substrate, and the temperature of the substrate can influence the interaction process between the adatoms and the substrate. The nucleation and the subsequent growth in the form of thin layers on the substrate depend on the interaction process. A slow growth rate is necessary to grow a good quality film.

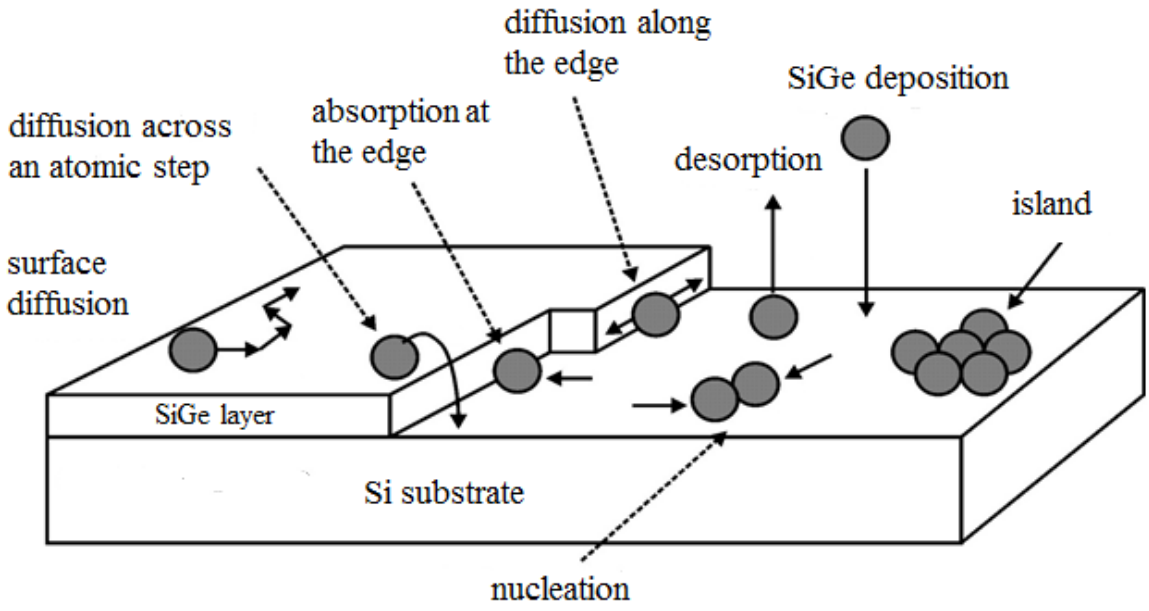

Figure 2.1 Schematic view of the fundamental processes during the growth of SiGe layer on Si substrate [21].

The MBE process involves highly controlled evaporation in an ultrahigh vacuum (~ 10^{-10} torr) environment. The molecules travel ballistically in the UHV environment [22]. Figure 2.1 shows the schematic view of the fundamental processes during the growth of SiGe or Ge layer on Si substrate. The adatoms can diffuse at the surface to an energetically favorable position where the surface energy is minimized. They can also undergo desorption, surface segregation, and nucleation. The Knudsen cells are difficult to use for the growth of SiGe layer due to the low vapor pressure of both Si and Ge. Hence, electron beam evaporators are used in the growth of Si and Ge. The disadvantage of using the electron beam evaporator is that it can create unwanted radiation in the chamber which introduces defects in the heterostructures.

The MBE system keeps the sample in rotation during the growth to achieve the film uniformity and precise control over the layer thickness and Ge content in the Si/SiGe nanostructures is possible in MBE system. The major advantage of MBE is that the Ge content of a layer is mostly dependent on the source flux and not on the substrate temperature or the chamber pressure. On the other hand, the Ge content is affected by the pressure, temperature, and flow rates of the gases in CVD process. Hence, less calibration is needed in MBE compared to CVD, MBE growth processes are extensively used for research [10].

2.2 Properties of Si/SiGe Nanostructures

2.2.1 Energy Band Structure and Band Alignment

Si and Ge both are indirect band-gap semiconductors. The lattice structure of Si and Ge is a diamond lattice structure. A unit cell of the diamond lattice structure consists of two face-centered cubic (fcc) lattices shifted by a quarter of the body diagonal ($\frac{1}{4}\ \frac{1}{4}\ \frac{1}{4}$) of the cell. On the other hand, the lattice structure of direct band-gap semiconductors such as GaAs is the zinc-blende structure. The electronic and optical properties differ between direct and indirect band-gap semiconductors due to their respective band structure. The band structure is simply defined as the E-k relation (the dispersion relation), where E is the energy of an electron (or hole) at the band edge with a wave vector k in the first Brilloiuin zone. The band structure of bulk Si and Ge at 300 K is shown in Figure 2.2.

Si and Ge valence energy band structure exhibit a maximum at the zone center k = 0. The valence band consists of a heavy holes band, a light holes band, and a split-off band. The heavy holes and light holes bands are degenerate at the zone center k = 0 or Γ symmetry point, which is maximum of the valence band. The degeneracy is partly broken shifting the split-off band to lower energies by 0.044 eV in Si and 0.29 eV in Ge. Si has six-fold degenerate conduction band minima, and the lowest energy point of the conduction band of Si is located at k ≈ 0.85X along the [001] direction (Δ-minimum). Ge has entirely different conduction band structures than Si in the reciprocal space. The conduction band minimum of Ge lies along the [111] direction at the Brillouin zone edge (L point). In band structure engineering, two or more group IV elements are combined to form an alloy such as $Si_{1-x}Ge_x$ with desired intermediate band gap structures. The

conduction band in unstrained $Si_{1-x}Ge_x$ alloy is like Si with six-fold Δ-minima for x<0.85 and it becomes like Ge with four-fold minima at the L-point for x>0.85 [23].

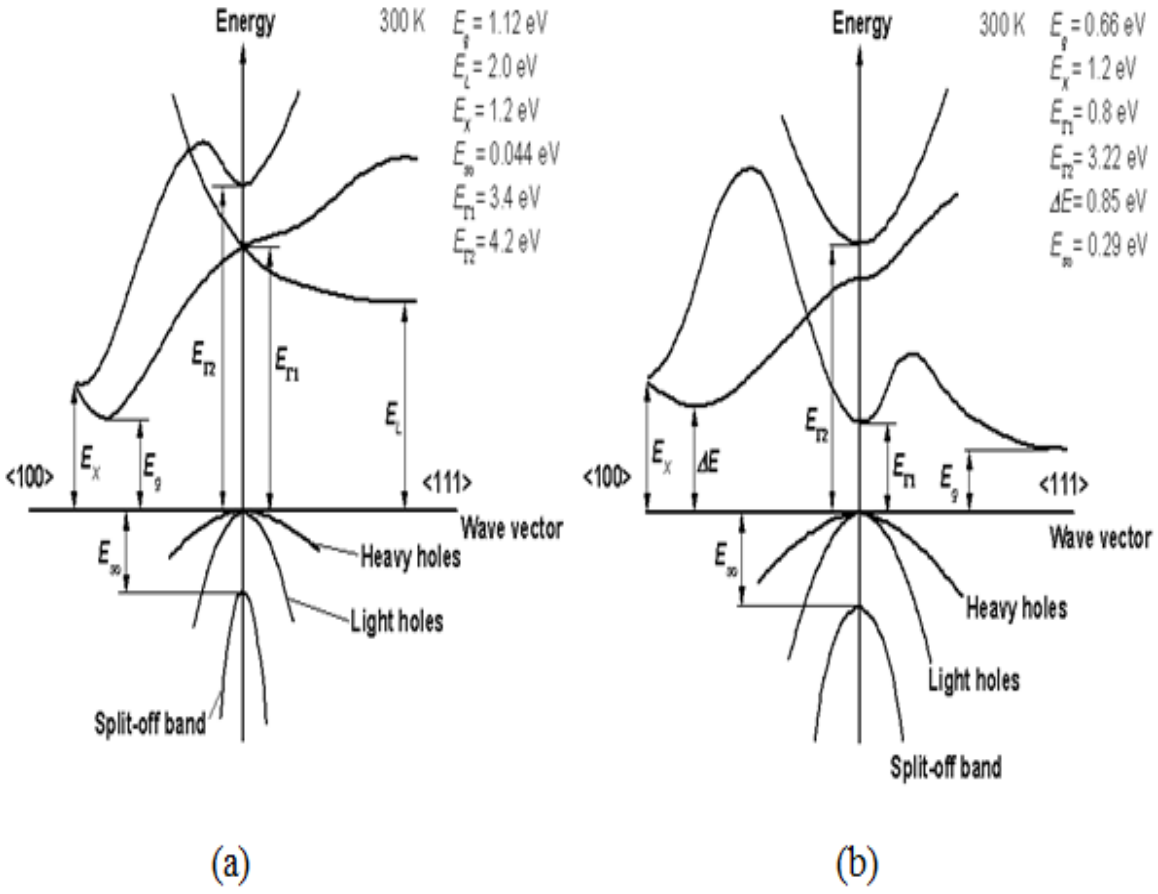

Figure 2.2 Energy band structures of (a) Si and (b) Ge at 300 K [24].

The lattice constant of Si, α_{Si} = 5.431 Å and Ge, α_{Ge} = 5.657 Å at room temperature (300 K). The band structure of SiGe is modified by the built-in strain due to the lattice mismatch (~ 4.2%) between Si and Ge [13]. This modification makes it possible to realize the band structure engineering in Si/SiGe NSs. In band structure engineering, strain plays an important role to change the energy band gap of SiGe layers grown on Si substrates. The energy gap of unstrained (upper dashed line) and strained

(solid line) $Si_{1-x}Ge_x$ alloy layers as a function of Ge concentration (x) at 4.2 K is shown in Figure 2.3. The minimum band gap of planar SiGe quantum wells (QWs) on Si is illustrated by the dashed-dotted line. The energy band gap becomes lower in case of wavy SiGe QWs grown by Stranski-Krastanov (S-K) growth mode, as presented by the gray area in Figure 2.3. Therefore, Si/SiGe NSs can emit light in the important low-loss optical communication wavelength range of 1.3 to 1.55 μm.

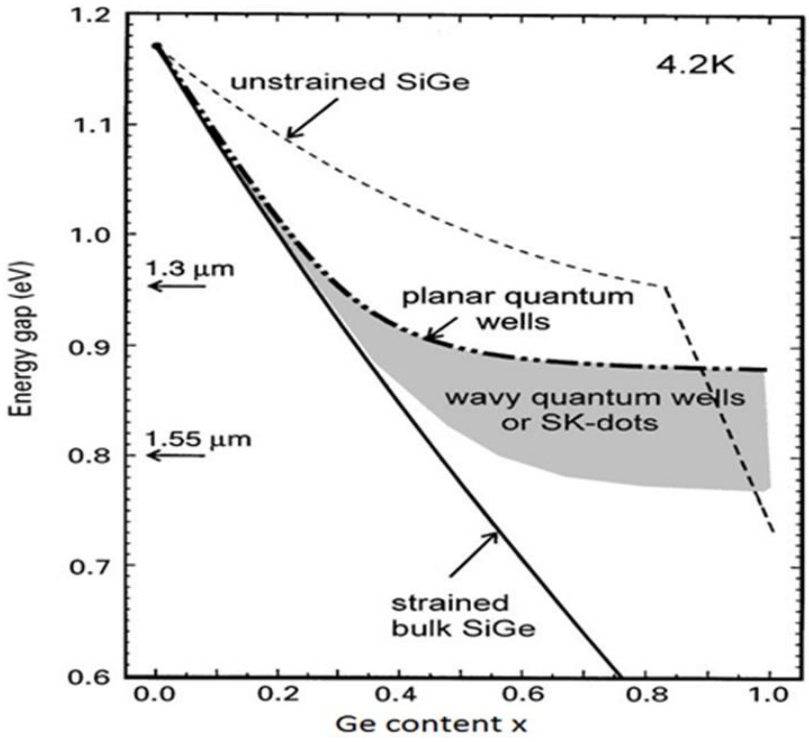

Figure 2.3 The energy gap of SiGe as a function of the Ge composition x for the relaxed and strained SiGe alloys [25].

When two materials of different band gaps are brought together to form a heterojunction, the band discontinuities occur in both the conduction and valence band due to the charge distribution near the heterojunction interface. Figure 2.4 illustrates

different types of energy band alignments in $Si/Si_{1-x}Ge_x$ NSs. The band alignment at Si/SiGe heterointerface affects the light emission properties and thus, it is necessary to understand the band alignment to realize physical and optical properties of Si/SiGe NSs. The discontinuity is larger at the valence band edge, while it is small at the conduction band edge. Valence band discontinuities in Si/SiGe(Ge) heterostructures is analyzed and calculated theoretically [26-28] and experimentally [29-31].

It is predicted that the alloy can form a well or a barrier for the electrons. Hence, the band alignment at Si/SiGe heterointerface is of two types: type I and type II. Electrons and holes are localized in the $Si_{1-x}Ge_x$ layer in type I energy band alignment, while electrons are localized in the Si and holes are localized in the $Si_{1-x}Ge_x$ layer in case of type II energy band alignment [32, 33]. Theoretical and experimental calculations of Baier et al. have concluded that the band alignment in $Si_{1-x}Ge_x$ ($0.1 \leq x \leq 0.36$) single QWs on Si is type II, as the energy upshifts of the QW PL line increases with the increasing well width. The energy upshifts occur due to the band-bending effect induced by the charge carriers with long lifetimes in the indirect band gap semiconductor materials, Si and $Si_{1-x}Ge_x$. In type II band alignment, the separation of electrons and holes leads to the Hartree potential, which makes the band bending obvious. Therefore, the increment of the well width leads to an increase of the charge separation, which results in more band-bending effects [33].

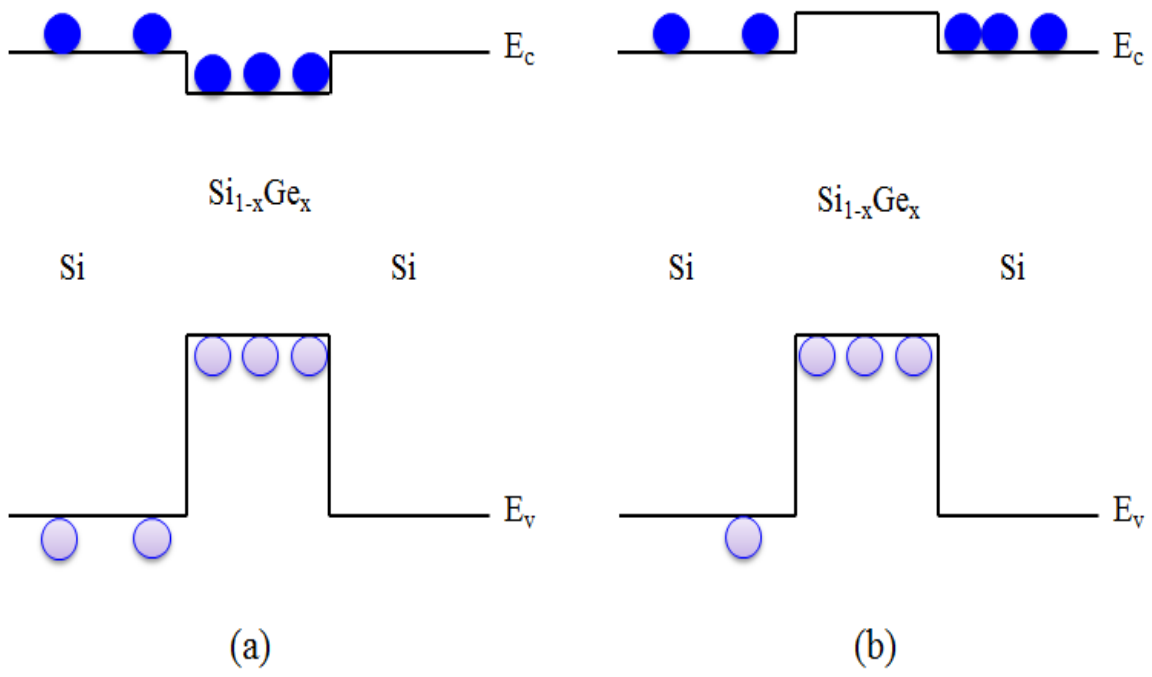

Figure 2.4 Schematic energy band alignment diagram of (a) type I and (b) type II in $Si/Si_{1-x}Ge_x$ NSs.

In an ideal case, the conduction band discontinuity ΔE_C is estimated from the difference in electron affinities $q(\chi_2 - \chi_1)$ and the valence band discontinuity ΔE_V is found from $\Delta E_g - \Delta E_C$. This is known as Anderson affinity rule [34]. The predicted ΔE_C is approximately 50 meV in Ge/Si heterojunctions, as χ_{Ge} = 4.05 eV and χ_{Ge} = 4.00 eV.

The energy of the indirect band-gap in $Si_{1-x}Ge_x$ alloys is determined from the low temperature PL data as a function of Ge concentration x [23]. The band-gap decreases smoothly from Si free-exciton gap at 1.155 eV to the excitonic gap in Ge at 0.74 eV. The crossover occurs at x = 0.85 from Si-like X-conduction band minimum to the Ge-like L-conduction band minimum. Braunstein et al. calculated the energy gap of $Si_{1-x}Ge_x$ alloys as a function of Ge concentration at 296 K based on one-phonon Macfarlane-Roberts expression [35].

The analytical expressions of energy band-gap for $Si_{1-x}Ge_x$ alloys are as follows [23]:

$$E_g^X(x) = 1.155 - 0.43x + 0.206x^2, \quad (2.1)$$

$$E_g^L(x) = 2.01 - 1.27x. \quad (2.2)$$

The equation 2.1 is for Δ-minima with $0 \leq x < 0.85$ and equation 2.2 is for L-minima with $0.85 < x \leq 1$.

The electron-phonon interaction depends on the temperature and also thermal expansion occurs in the lattice. Therefore, the band-gap shows temperature dependence which can be described according to Varshni's empirical equation [36]. The band-gap of Si and Ge at temperature T is given by:

$$E_g(T) = E_g(0) - \frac{\alpha T^2}{\beta + T}, \quad (2.3)$$

where T is the absolute temperature, $E_g(0)$ is the band gap at 0 K, α and β are fitting parameters. The values of α and β for bulk Si and Ge are listed in Table 2.1.

Table 2.1 Varshni's Parameters α and β of Indirect Band gap Si and Ge

	Si	Ge
α (10^{-4} eV/K)	4.73	4.77
β (K)	636	235

The band gap of compressively strained $Si_{1-x}Ge_x$ layer at temperature T can be approximated by the relationship:

$$E_g(x,T) = E_0(T) - 0.96x + 0.43x^2 - 0.13x^3, \quad (2.4)$$

where $E_0(T)$ is the band gap of bulk Si at temperature T.

2.2.2 Strain and Critical Thickness in Si/SiGe NSs

The ability to grow dislocation free coherently strained epitaxial layer is a challenging issue in lattice mismatched heterojunctions like Si/SiGe. There is ~4.2% lattice mismatch between Si and Ge. The lattice constant of bulk $Si_{1-x}Ge_x$ alloy layer ($0 \leq x \leq 1$) at 300 K is predicted by [37]:

$$a_{SiGe} = 5.431 + 0.1992x + 0.02733x^2. \quad (2.5)$$

A thin $Si_{1-x}Ge_x$ layer will be compressively strained when it is grown on top of Si while it will be tensilely strained when a Si layer is grown on top of a $Si_{1-x}Ge_x$ layer. Figure 2.5 shows the schematic diagram illustrating the compressive and tensile strains created in materials with different lattice parameters.

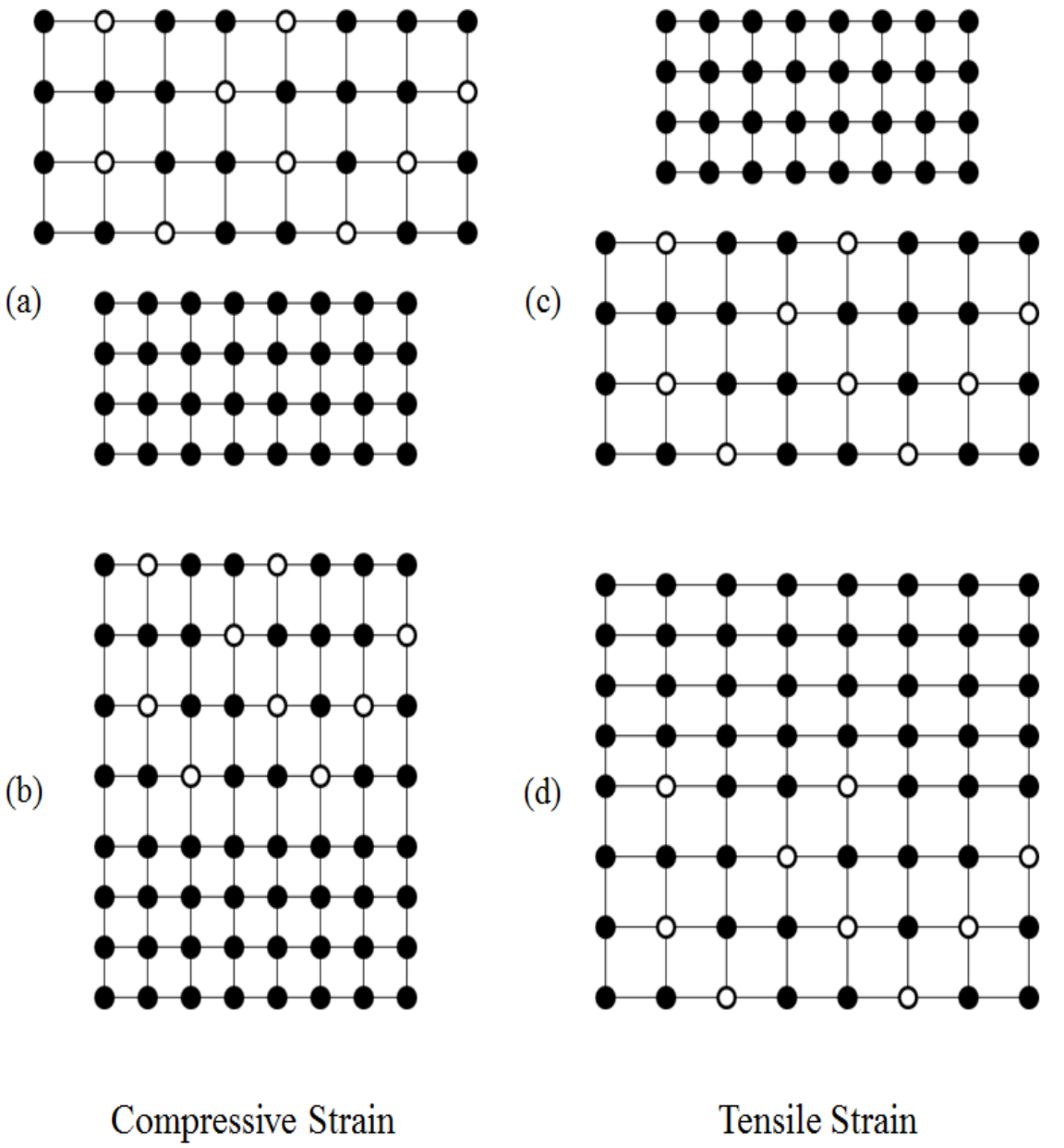

Figure 2.5 (a) A schematic view of the bulk material with a higher lattice constant such as $Si_{1-x}Ge_x$ layer to be grown on the bulk material with a lower lattice constant such as Si, (b) $Si_{1-x}Ge_x$ layer becomes compressively strained when two materials are placed together. (c) A schematic view of the bulk Si layer to be grown on top of the $Si_{1-x}Ge_x$ thin layer, (d) Si layer is tensile strained when it is placed on top of the $Si_{1-x}Ge_x$ layer [10].

The strain lies in the plane of the layer is called in-plane strain ($\epsilon_{\parallel}$). It could also be in the perpendicular direction, called the perpendicular strain ($\epsilon_{\perp}$). The strains are related by Poisson's ratio (ν) according to isotropic elastic theory:

$$\epsilon_{\perp} = \frac{-2\nu}{1-\nu}\epsilon_{\parallel}. \tag{2.6}$$

If the lattice parameters of two unstrained layers are a_A and a_B with the thicknesses of h_A and h_B, respectively, the parallel lattice constant due to the tetragonal distortion is determined by:

$$a_{\parallel} = a_A\left[1 + \frac{f}{1+\left(\frac{G_A h_A}{G_B h_B}\right)}\right], \tag{2.7}$$

where G_A and G_B are the shear modulus of layers A and B, respectively. The misfit f between two layers is defined by:

$$f = \frac{a_B - a_A}{a_A}, \tag{2.8}$$

and the in-plane strain relation between two layers is expressed as:

$$\epsilon_{\parallel}^{A} = -\left(\frac{G_B h_B}{G_A h_A}\right)\epsilon_{\parallel}^{B}. \tag{2.9}$$

In $Si/Si_{1-x}Ge_x$ NSs, a thin $Si_{1-x}Ge_x$ epitaxial layer is grown on top of the thicker Si substrate and a coherent or pseudomorphic heterointerface will be formed. The strain is balanced between two layers by the successive growth of compressive and tensile strained layers. It is necessary to keep the thickness of each layer in a coherently strained heterostructure below a certain thickness for strain relaxation. This thickness is called the critical thickness. Above the critical thickness, misfit dislocations will be formed to release the strain accumulated in the layer [38]. In the 1980s, the critical thickness for strain relaxation have been predicted by developing theoretical models [38-41] and measured experimentally in $Si/Si_{1-x}Ge_x$ SL [42-44]. The models proposed by Matthews-Blakeslee [38] and People-Bean [39] based on the equilibrium theory, and by Dodson-Tsao [40, 41] based on the kinetic theory are well known to explaining the critical thickness for strained epitaxial layers in lattice mismatched heterostructures. Van der Merwe [45] has determined the critical thickness, h_c by a coincidence of the interfacial energy between film and substrate for dislocation generation with the areal strain energy density associated with a film of thickness, h. The calculated critical thickness in SiGe/Si system according to Van der Merwe theory is given by:

$$h_c \cong \left(\frac{1}{8\pi^2}\right)\left(\frac{1-\nu}{1+\nu}\right)\frac{a_0}{f}, \tag{2.10}$$

where a_0 is the bulk lattice constant of the substrate, ν is the Poisson's ratio, and f is the misfit between film and substrate.

The critical thickness predicted by Matthews and Blakeslee is based on the mechanical equilibrium theory. According to this theory, the onset of interfacial misfit

dislocations is determined by the mechanical equilibrium of a grown-in threading dislocation. The critical thickness given by Matthews and Blakeslee is [38]:

$$h_c \cong \left(\frac{b}{f}\right)\left[\frac{1}{4\pi(1+\nu)}\right]\left[\ln\left(\frac{h_c}{b}\right)+1\right], \tag{2.11}$$

where b is the magnitude of the Burger's vector.

People and Bean calculated the critical thickness in strained $Si_{1-x}Ge_x$ layers on Si substrate assuming generation of misfit dislocations is determined merely by energy balance. The most accepted theory proposed by People and Bean [46] in the $Si_{1-x}Ge_x$ /Si heterostructures is:

$$h_c \cong \left(\frac{1.9\times 10^{-2}\text{Å}}{f^2}\right)\ln\left(\frac{h_c}{4\text{Å}}\right), \tag{2.12}$$

where $f = \left(\frac{a_{SiGe}-a_{Si}}{a_{Si}}\right) = 0.042x$. The calculated values for the critical thickness are in good agreement with the lattice misfit. Figure 2.6 shows the critical thickness as a function of Ge concentration based on three different proposed theories. The obtained results are different due to the growth temperature and measurement techniques.

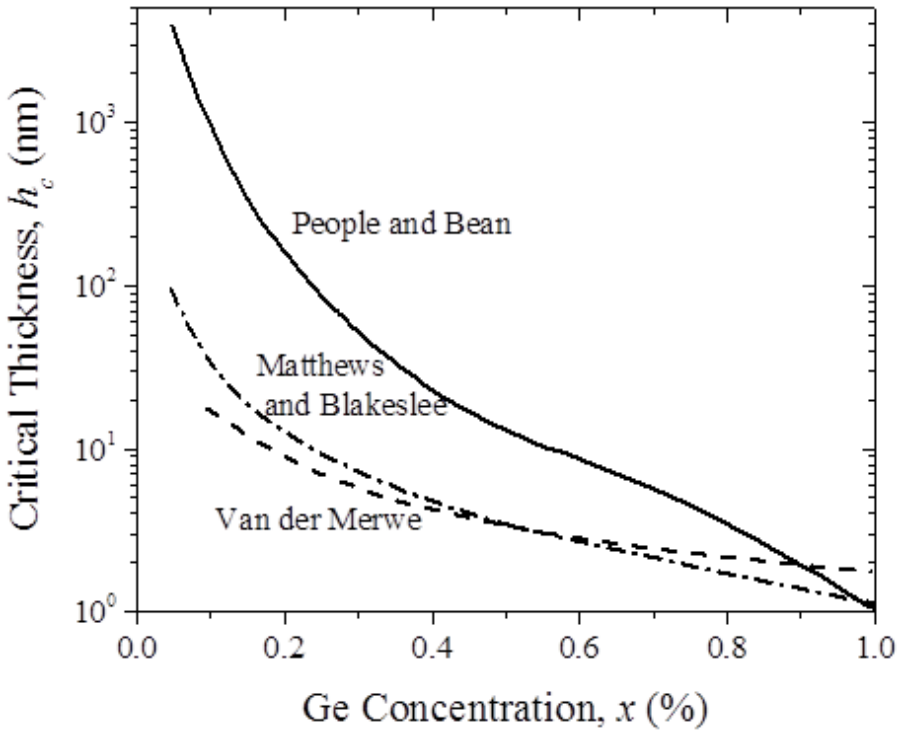

Figure 2.6 Critical thickness of strained $Si_{1-x}Ge_x$ layer on (001) Si as a function of Ge content x according to the Van der Merwe, Matthews-Blakeslee, and People-Bean theory [46].

2.2.3 Growth Mechanisms

The growth process of thin-film semiconductor is divided into three basic modes, as illustrated in Figure 2.7 [47]. Three dimensional islands are formed when the atoms or molecules in the deposit are more strongly bound to each other than to the substrate, called island or Volmer-Weber growth mode, 2) Layer-by-layer or Frank- van der Merwe growth mode occurred when the atoms in the deposit are more strongly bound to the substrate than to each other, and 3) The layer plus island or Stranski-Krastanov (S-K) mode is an intermediate mode, a combination of two other modes. S-K mode starts with a planar two dimensional (2D) layer and the strain energy due to the lattice mismatch between the film and the substrate is accumulated in the layered structure (2D planar SL). This layer is called the wetting layer (WL). When the increasing layer thickness exceeds

the critical thickness, it becomes energetically favorable to relieve lattice-mismatch induced strain by the formation of islands/clusters rather than by creating misfit dislocations. Thus, the strain energy is relaxed by increasing the surface energy, which in turn leads to the formation of islands on top of the 2D layer.

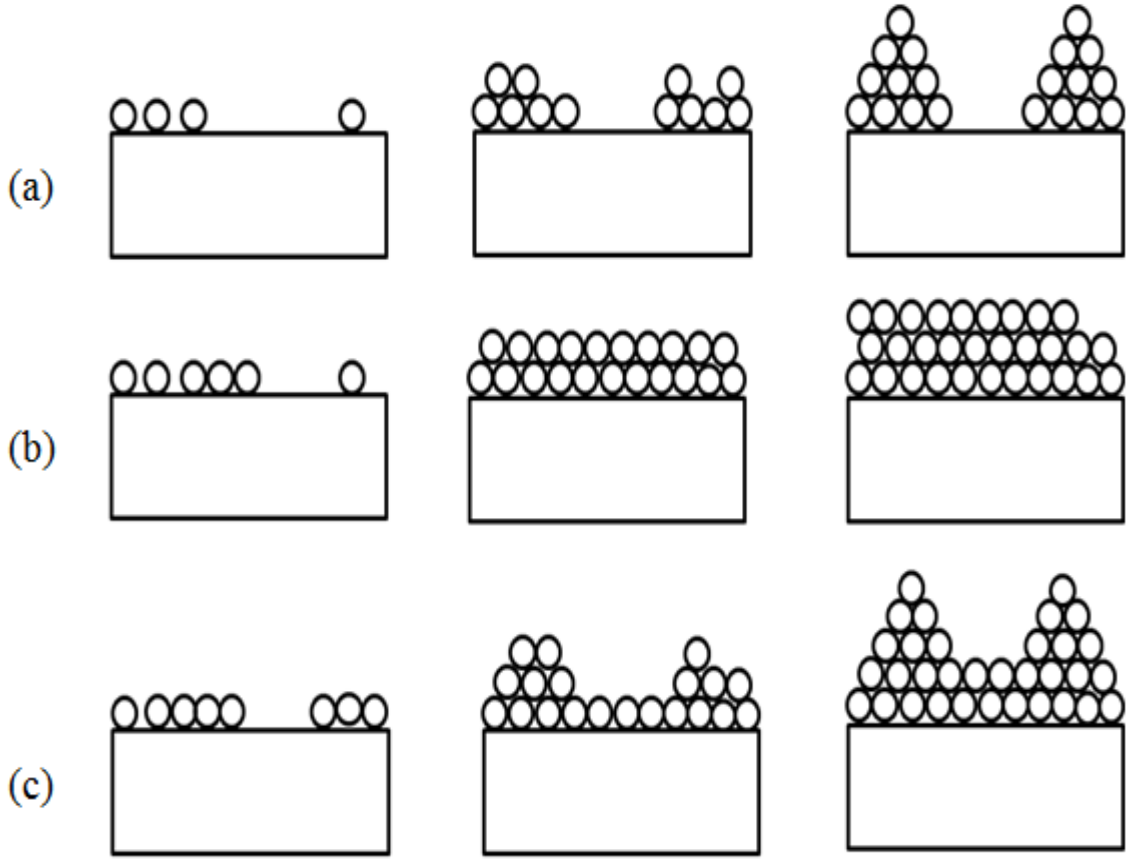

Figure 2.7 Growth modes in heteroepitaxy: (a) island or Volmer-Weber, (b) layer-by-layer or Frank- van der Merwe, and (c) layer-plus-island or Stranski-Krastanov.

In Si/SiGe heteroepitaxial growth, S-K growth mode is used to produce self-assembled SiGe clusters on Si substrate. The Ge content (x) is low in the alloy layer to keep the lattice strain energy minimum. As the lattice constant of SiGe layer is larger

than the Si substrate layer, SiGe layer experiences lateral lattice compression. The stored elastic energy increases linearly with the layer thickness, d according to the formula [48]:

$$E_{strain} \propto \varepsilon^2 d. \tag{2.13}$$

Therefore, a pseudomorphic SiGe layer can be grown on a Si substrate up to a certain critical thickness. As soon as the thickness of the SiGe layer exceeds the critical thickness (a few monolayers), the accumulated strain energy in the SiGe layer is released either by the generation of misfit dislocations or by introducing the formation of islands on top of the substrate. S-K growth mode in Si/SiGe NSs is illustrated in Figure 2.8.

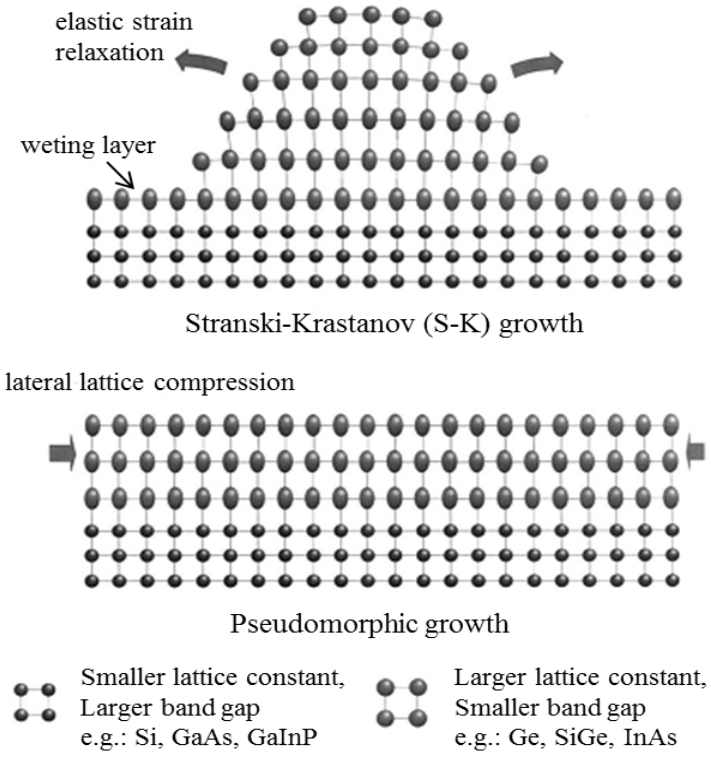

Figure 2.8 Schematic of island formation of SiGe alloy on top of Si in S-K growth mode [25].

SiGe layer embedded in Si layers and combined energy gaps of these structures are shown in Figure 2.9. The thickness of the SiGe island increases compared to that of the planar SiGe QW layer. Thus, the confinement shift in Si/SiGe 3D island morphology nanostructures is decreased as indicated by the double arrow in Figure 2.9 (b). The reduced confinement shift in SiGe islands allows much lower energy emission than the SiGe QW layers in Si.

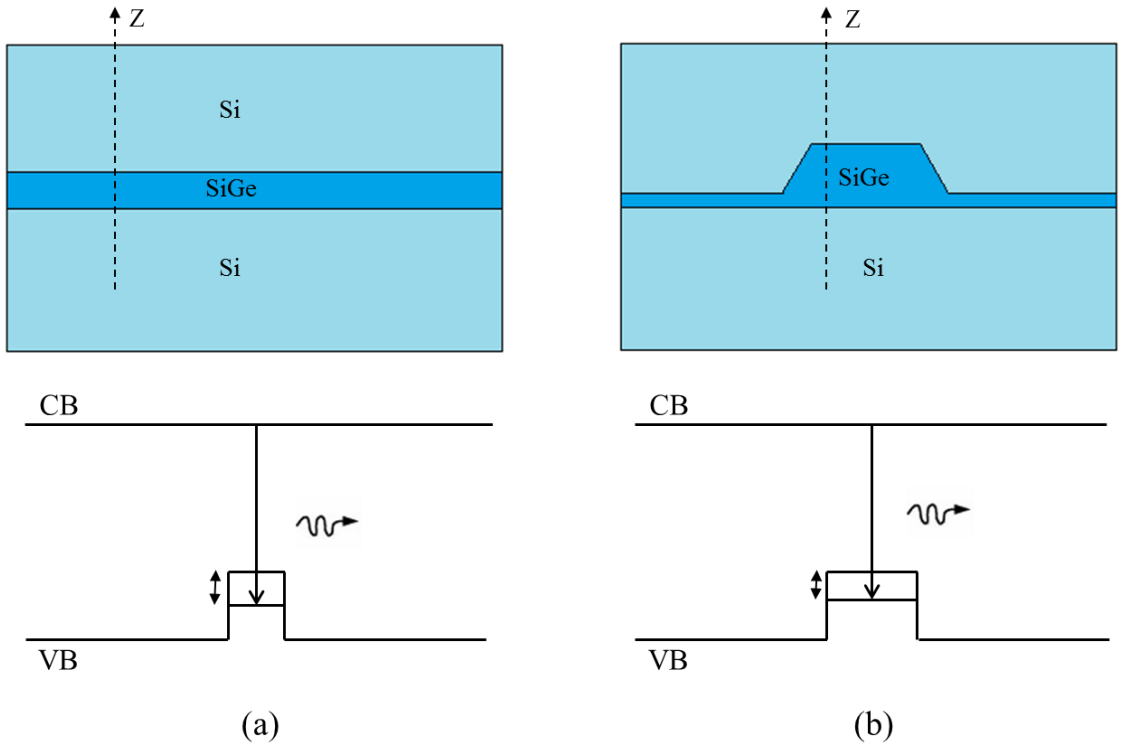

Figure 2.9 (a) Planar strained SiGe QW and (b) embedded SiGe island in Si layers. The total layer thickness at the position, Z is increased in the island. The confinement shift is indicated by the double arrow [25].

2.2.4 Structural Properties

Structural characterization of Si/SiGe samples allows to predicting and tailoring the electronic and optical properties for desired applications. Transmission electron microscopy (TEM), X-ray diffraction (XRD), Energy dispersive X-ray (EDX) spectroscopy, optical techniques such as Raman scattering and PL spectroscopy are mostly used to analyze the structural properties of the samples.

In Si/SiGe nanostructures, significant interdiffusion between SiGe layers and Si spacer layers takes place during growth. Hence, the effective Ge content, the effective bandgap, strain, and the shape of the structure vary accordingly [21]. The EDX data for the $Si_{1-x}Ge_x$ layers show a continual increase in Ge composition x reaching a maximum value close to the middle of a $Si_{1-x}Ge_x$ cluster, most likely due to Si/SiGe intermixing during growth [12, 49, 50]. In the growth of 3D $Si/Si_{1-x}Ge_x$ NSs, the island shape depends on the substrate temperature, Ge concentration, and coverage in the epilayer. Figure 2.10 shows the shapes of SiGe cluster grown on Si substrate. Initially, small islands with low aspect ratio (ρ) called pre-pyramids appear on the top of the wetting layer. The aspect ratio ρ is defined as:

$$\rho = \frac{h}{\sqrt{S}}, \tag{2.14}$$

where h is the height and S is the base surface area of the island. At the later stages of growth, small islands transform into shallow (105) faceted islands with pyramidal shape [51]. As the Ge coverage increases, larger multifaceted islands (domes) with higher aspect ratio form on the surface [52]. The shape of the island changes from pyramid to

dome in order to reduce the strain energy. The dome shaped islands allow more strain relaxation than the pyramids by increasing the surface energy. Two different island shapes (pyramid and dome) exist together depending on the growth conditions and island size distribution (see Figure 2.10 (c)).

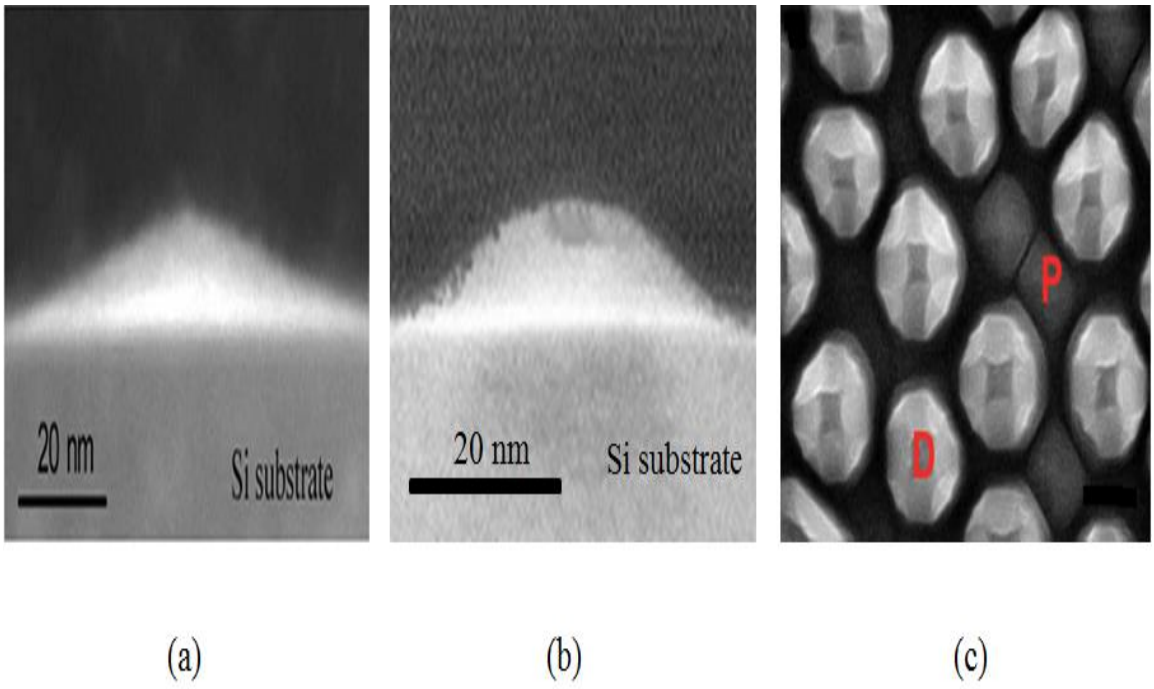

Figure 2.10 Cross-sectional TEM images of (a) pyramid-shaped and (b) dome-shaped SiGe cluster grown on Si substrate. (c) Scanning electron microscopy (SEM) image of Ge islands grown on Si at 690 ^{o}C. Both pyramid- (P) and dome- (D) shaped islands formed at this growth temperature [14, 50, 53].

It has also been observed that self-assembled Ge islands grown on Si exhibit minimization in strain energy due to the reduction in the lattice-mismatch during annealing at 650 ^{o}C. Thus, it becomes thermodynamically favorable for the islands to change the shape again from dome to pyramid. The reduction of lattice-mismatch occurs as a result of the Si intermixing with the Ge epilayer [54] at 650 ^{o}C. The island shape and

size distribution have been extensively studied by several authors [14, 52, 54, 56]. It is established from their experiments and theoretical explanations that the structural properties of SiGe clusters can be tailored by optimizing the growth parameters and performing post-growth treatments.

2.2.5 Thermal Properties

Heat dissipation is becoming a crucial issue for thermal management in the growing semiconductor industry. High thermal conductivity materials are desired in order to dissipate heat efficiently in optoelectonics, while low thermal conductivity materials find potential applications in the field of thermoelectric devices [57, 58].

The strain originating from the 4.2% lattice mismatch between Si and Ge in $Si/Si_{1-x}Ge_x$ NSs offer the degree of freedom to control the thermal conductivity [59] and attract much research attention in the field of optoelectronic as well as thermoelectric devices. The thermal properties of $Si/Si_{1-x}Ge_x$ multilayers NSs differ significantly from the corresponding bulk Si or Ge due to nonostructuring and alloying.

Modern fabrication processes of $Si/Si_{1-x}Ge_x$ multilayers NSs allow us to achieve high figure of merit tailoring the lattice thermal conductivity. The dimensionless figure of merit is defined as:

$$ZT = \frac{S^2\sigma}{\kappa}T, \tag{2.15}$$

where S is the Seebeck coefficient, σ is the electrical conductivity, κ is the thermal conductivity, and T is the absolute temperature [60]. The thermal conductivity of a

semiconductor is the sum of the electrical thermal conductivity (κ_e) and the lattice (phonon) thermal conductivity (κ_L). From the 1990s, low-dimensional NSs such as Si/Ge SLs [61], $Si/Si_{1-x}Ge_x$ SLs [15], SiGe nanocomposites [62], and Si nanowires [63, 64] have been extensively studied to enhance the thermoelectric figure of merit by reducing the thermal conductivity [65, 66].

Thermal conductivity is one of the fundamental properties of solids representing the ability to conduct heat. This property is usually quantified in terms of the thermal conductivity coefficient, which is defined through the macroscopic expression as:

$$Q = -\kappa \Delta T, \tag{2.16}$$

where Q is the rate of heat energy flow per unit area normal to the temperature gradient ΔT. Electrical carriers (electrons or holes), lattice waves (phonons), electromagnetic waves, spin waves, or other excitations can contribute to conductivity of heat in solids. Electrical carries carry the majority of the heat in metal, while in semiconductors and insulators, heat is conducted by phonons [67]. Phonons are the quanta of lattice vibrations, which responsible for lattice thermal conductivity.

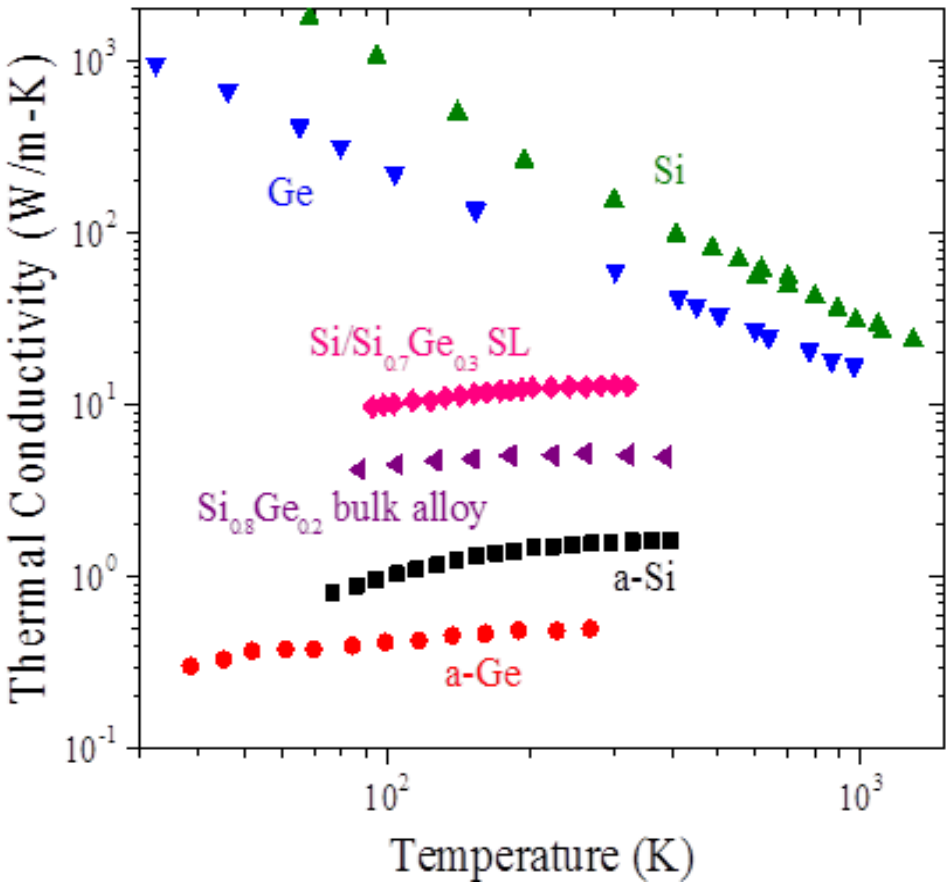

Figure 2.11 Thermal conductivity of SiGe bulk alloy [61] and $Si/Si_{0.7}Ge_{0.3}$ SL (300 Å /150 Å) [15] with comparison to data of c-Si, c-Ge [68], a-Si [69], and a-Ge [70].

The lattice thermal conductivity in Si/SiGe NSs is reduced compared to that of bulk c-Si due to different phonon scattering mechanisms. Si has high thermal conductivity compared to that of many metals in spite of its nonmetallic characteristics. Ge, also has a rather large thermal conductivity. The lattice conductivity of Si and Ge at room temperature (300 K) is 113 and 63 W/m-K, respectively. SiGe NS shows approximately 10 times reduction in thermal conductivity compared to that of Si. Figure 2.11 illustrates the temperature dependence of thermal conductivity of different Si and SiGe-based materials.

Figure 2.11 clearly depicts that the thermal conductivity in SiGe NSs is less than the pure crystals and more than the amorphous phases. Due to the lack of long range ordering in atomic structure, the thermal conductivity is significantly reduced in the amorphous phases (a-Si and a-Ge). Different phonon scattering processes may dominate heat transport in a material depending on the temperature. The dominant phonon wavelength, which carries the maximum amount of heat energy according to Wien's displacement law:

$$\lambda = \frac{h\nu}{\kappa_B T}, \tag{2.17}$$

where h, ν, k_B, and T are the Plank's constant, speed of phonon, Boltzmann constant, and the absolute temperature, respectively. The thermal conductivity in pure crystals (c-Si and c-Ge) decreases faster than the predicted T^{-1} law. The reason is that the three-phonon, four-phonon, isotope scattering processes play important role at high temperature [68]. Si/SiGe SL shows a gradual increase in thermal conductivity with temperature.

The size effects on thermal conductivity of Si/SiGe NSs become very important when the layer thicknesses are comparable to the mean free path or wavelength of the phonons. Phonon behaves as a particle for the layers thicker than the mean free path, while the wave interference can affect the transport properties as long as the phonon mean free path is comparable or longer than the film thickness [66]. Figure 2.12 shows the measured thermal conductivity of $Si_{1-x}Ge_x$ nanostructures as a function of either the SL periodicity, or the film thickness.

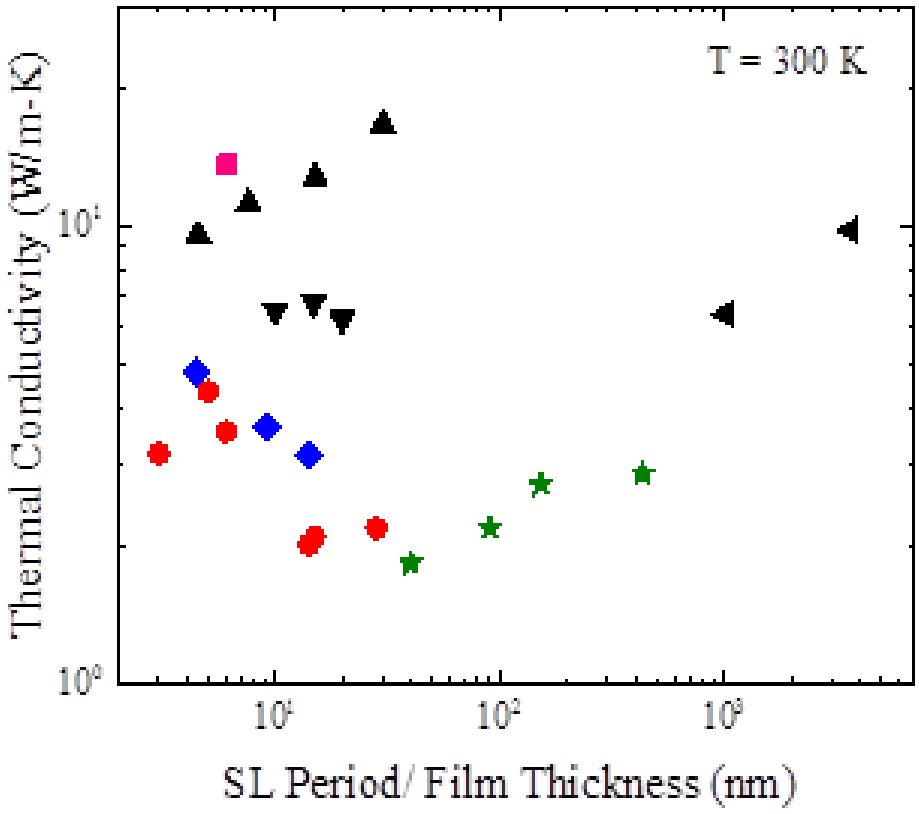

Figure 2.12 Thermal conductivity measured at room temperature (300K) for Si/Ge SL (red circle) [61], $Si/Si_{0.7}Ge_{0.3}$ SL (black up triangle), $Si_{0.84}Ge_{0.16}/Si_{0.74}Ge_{0.26}$ SL (black down triangle), and $Si_{0.9}Ge_{0.1}$ SL (black left triangle) [15], Si/Ge SL (blue diamond) [71], $Si/Si_{0.7}Ge_{0.3}$ SL (pink square) [72], $Si_{0.8}Ge_{0.2}$ SL (olive star) [73].

Interfaces play an important role to the reduction of thermal conductivity in Si/SiGe NSs. Several authors have modeled the phonon transport and the lattice thermal conductivity in different materials systems based on the Boltzmann transport equation by assuming the diffuse or specular interface scattering of phonons [66, 74-76]. The thermal conductivity could be reduced further due to the diffuse interface in 3D Si/SiGe NSs compared to that in 2D Si/SiGe NSs. The phonon dispersion curve deduced from Raman scattering have been investigated to explain the interface scattering mechanisms in 2D and 3D Si/SiGe NSs.

In the literature, a number of mechanisms including modification of phonon group velocity and phonon confinement based on lattice dynamics models [77-81], diffuse interface scattering based on the Boltzmann transport equation treating phonon as particles [74], and the wave interference of phonons at the interface based on the acoustic wave propagation [82] have been discussed. Several experimental (electrical and optical) techniques have been widely used to determine the thermal conductivity of multilayers NSs in the in-plane (parallel to the layers) and cross-plane (perpendicular to the layers) directions [83].

2.3 Characterization Techniques of Si/SiGe Nanostructures

2.3.1 Transmission Electron Microscopy

TEM is the most efficient and versatile microscopy technique for structural, compositional, and chemical characterization of materials. In conventional transmission electron microscope, an electron beam of uniform current density is transmitted through a thin specimen. The electron gun emits the beam of electron by thermionic, Schottky, or field emission from a small source region (tip). Besides the electron gun, the illumination system in TEM consists of the condenser lenses with different apertures. The condenser lens system produces an electron beam with desired diameter and transfer the beam to the specimen. The typical range of acceleration voltage is 100 – 200 kV.

In the imaging system of TEM, the objective lens is the most essential part. A diifraction pattern is formed at the back focal plane of the objective lens after the beam-specimen interaction. There are two imaging modes in TEM depending on the aperture position of the objective lens: bright field and dark field. The bright field image mode

removes the Bragg reflections and allows only the direct beam to pass through the aperture placed at the back focal plane of the objective lens [84, 85]. On the other hand, the diffracted beam passing through the aperture produces the dark field image. The intermediate and projector lenses are used to magnify the image and to focus that on the screen or computer display via a detector, CCD, or TV camera [86, 87].

The samples studied in this thesis are analyzed using a JEOL JEM-2100F field emission transmission electron microscope. The JEM-2100F provides best image quality and maximum analytical resolution with the operating voltage of 200 kV. High long-term currents are delivered from the Schottky field emission electron source for excellent performance analysis. The electron beam can be focused to an extremely small beam diameter of < 0.05 nm. This includes an electron optics which is free of image rotation. Thus, simplified allocation of TEM images and diffraction patterns are possible. A Fischione annular dark field detector attached to the JEM-2100F is used to obtain the high angle annular dark field (HAADF) scanning TEM images of Si/SiGe NSs. The Scanning TEM (STEM) mode provides strong chemical contrast in Si/SiGe NSs. TEM analytical techniques are used for the quantitative studies of these structures, which involve energy-dispersive X-ray spectroscopy using an Oxford INCA Energy TEM 200 attached to the JEM-2100F and electron energy loss spectroscopy (EELS) using a Gatan GIF Tridiem attached to the JEM-2100F [14]. A thick $Si/Si_{1-x}Ge_x$ NS with known Ge concentration x is used for the calibration in EDX.

2.3.2 Raman Scattering

When a monochromatic light of frequency ω_i is incident on a crystal, a small fraction of the light is scattered in the inhomogeneous media. The scattered light has three components with different frequencies as shown in Figure 2.13. The strong scattered radiation is at the same frequency (ω_i) as the incident radiation due to the elastic scattering of photons. This process is called Rayleigh scattering. The other two have frequencies of $\omega_i \pm \omega_p$, where ω_p is the phonon frequency. Since the frequency of photons in monochromatic light changes upon interactions with molecular vibrations, this process is known as inelastic scattering. Raman scattering is described as inelastic scattering of a photons by matter. Raman scattering are of two types: Stokes and anti-Stokes scattering. The energy transfer between the photons and the scattering system gives rise to the origin of the Stokes and anti-Stokes scattering. The photon has lost energy by emitting a phonon and frequency is shifted to lower energies in case of Stokes scattering, while the photon has gained energy due to phonon absorption and frequency is shifted to higher energies in anti-Stokes scattering. The Stokes frequency, $\omega_S = \omega_i - \omega_p$ and anti-Stokes frequency, $\omega_{AS} = \omega_i + \omega_p$.

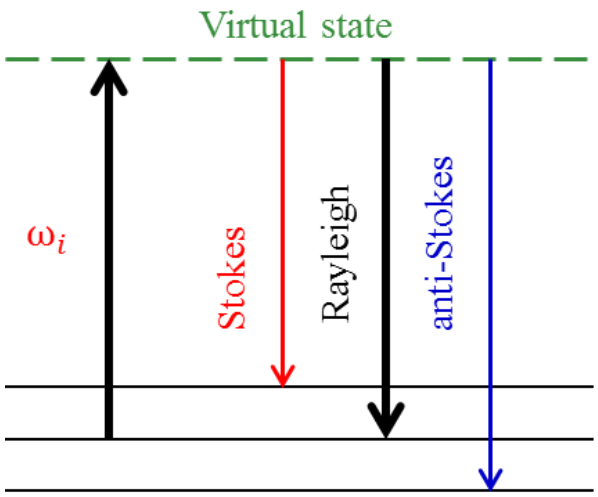

Figure 2.13 Energy-level diagram showing the Rayleigh and Raman effects.

Raman scattering is a non-destructive and versatile research tool allowing studies of chemical composition, strain, intermixing, and heat dissipation. Numerous publications reported effects of varying composition (x), strain, and temperature on Raman spectra in $Si_{1-x}Ge_x$ NSs [88- 92]. At the same time, quantitative analysis of Raman data combined with analytical electron microscopy provides unambiguous explanations of Raman features, and it is extremely useful for understanding and predictions of $Si/Si_{1-x}Ge_x$ NS properties as well as for the development of a reliable, non-destructive, and expedite metrological procedure.

2.3.2.1 First-order Optic Modes in Si/SiGe NSs. Raman spectroscopy is considered as an important tool which provides information to study electrical, optical, vibrational, and thermal properties of semiconductor heterostructures and superlattices. It has been widely used to discuss the alloy composition, lattice strain, and heterointerface abruptness of $Si/Si_{1-x}Ge_x$ NSs grown by MBE and CVD [11, 14, 93, 94]. The

simultaneous determination of Ge concentration and strain in $Si_{1-x}Ge_x$ layers has been obtained using Raman spectroscopy. The knowledge of composition and strain of heterostructures is necessary for many applications in optoelectronics. In $Si/Si_{1-x}Ge_x$ NSs, the peak frequency of three major first-order optical phonon modes shown in Figure 2.14 appears at approximately 295 (Ge-Ge), 415 (Si-Ge), and 505 (Si-Si) cm^{-1} [95]. The frequencies of these three first-order optic phonon modes depend on Ge concentration x [96, 97] and also on the strain [98].

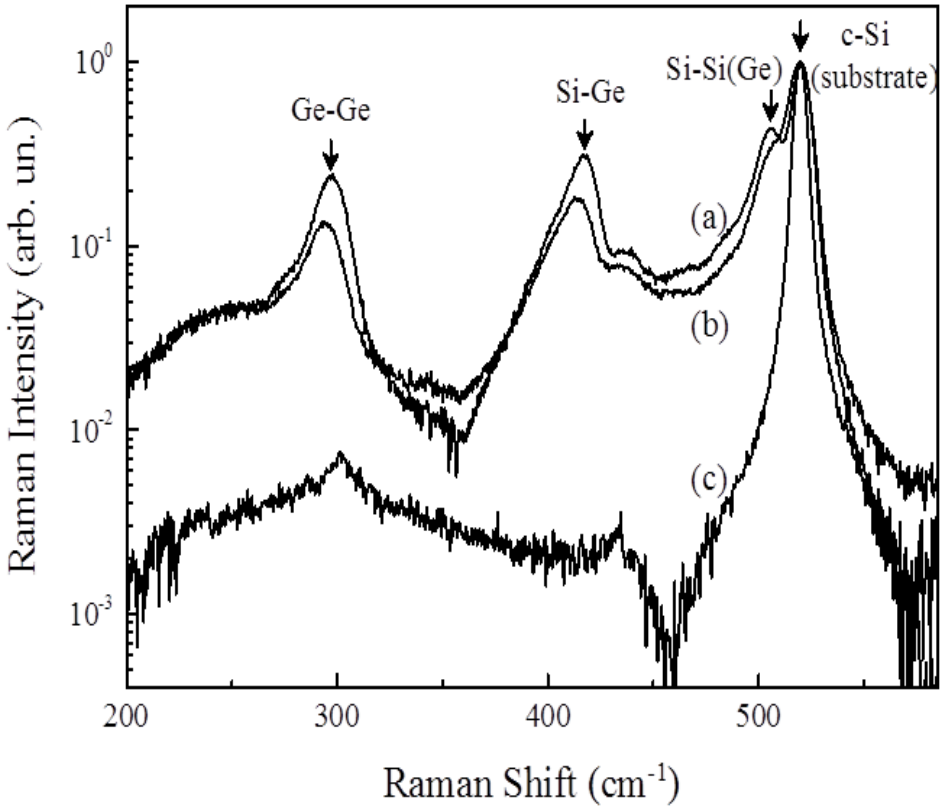

Figure 2.14 The first-order optical modes of Raman spectra in (a) 2D planar Si/SiGe SL, (b) 3D non-uniform Si/SiGe cluster multilayer, and (c) c-Si.

The optical-phonon frequency in $Si/Si_{1-x}Ge_x$ shifts due to the combined effects of strain and Ge content x according to the relationship [88]:

$$\omega = \omega_0 + \left(\frac{\omega_0}{2}\right)(p\epsilon_\perp + 2q\epsilon_\parallel), \tag{2.18}$$

where ω_0, the phonon frequency of the unstrained cubic lattice is a function of x and p, q are phenomenological parameters. Putting equation (2.6) into equation (2.15), it yields

$$\omega = \omega_0 + b\epsilon_\parallel, \tag{2.19}$$

where the strain-shift coefficient, $b = \frac{1}{\omega_0}\left[\frac{p\nu}{\nu - 1} + q\right]$, is an important parameter to determine the strain of the particular material.

Many authors have measured the peak frequencies as a function of the Ge content x at room temperature and equations are suggested for the Si-Si, Si-Ge, and Ge-Ge modes in the range of $0 < x < 0.5$ and $0 < x < 1$. The experimentally found equations for the Si-Si peak in a SiGe layer are [11, 99-103]:

$$\omega_{SiSi}(x) = 520.2 - 70.5x, \tag{2.20}$$

$$\omega_{SiSi}(x) = 520 - 70x, \tag{2.21}$$

$$\omega_{SiSi}(x) = 520.2 - 62x, \tag{2.22}$$

$$\omega_{SiSi}(x) = 520.2 - 66.7x, \tag{2.23}$$

$$\omega_{SiSi}(x) = 521.2 - 67.9x, \tag{2.24}$$

$$\omega_{SiSi}(x) = 520.7 - 66.9x. \tag{2.25}$$

For the Si-Ge peak position, following expressions are used [14, 99-101, 103]:

$$\omega_{SiGe}(x) = 400.5 + 16.3x, \quad (2.26)$$

$$\omega_{SiGe}(x) = 400.5 + 12x, \quad (2.27)$$

$$\omega_{SiGe}(x) = 400.5 + 14.2x, \quad (2.28)$$

$$\omega_{SiGe}(x) = 399.6 + 50.3x - 24.9x^2, \quad (2.29)$$

$$\omega_{SiGe}(x) = 400.1 + 24.5x - 4.5x^2 - 33.5x^3. \quad (2.30)$$

The expressions for the Ge-Ge peak position are [11, 101-103]:

$$\omega_{GeGe}(x) = 282 + 12.5x, \quad (2.31)$$

$$\omega_{GeGe}(x) = 282.5 + 16x, \quad (2.32)$$

$$\omega_{GeGe}(x) = 280.8 + 19.37x, \quad (2.33)$$

$$\omega_{GeGe}(x) = 280.3 + 19.37x. \quad (2.34)$$

It is seen in Figure 2.15 that the Si-Si (Ge-Ge) peak frequency decreases (increases) linearly with the Ge content, while the Si-Ge mode exhibits linear as well as nonlinear behaviors, shown in Figure 2.15 (b) [14, 99].

The dependency of the peak frequency shifting of Raman modes on strain is investigated in the literature [98, 100]. The strain-shift coefficient is the key parameter to determine the strain from the optical phonon frequency in $Si/Si_{1-x}Ge_x$ NSs. The

experimental values of b range from -732 to -815 cm^{-1} [89]. In strained $Si_{1-x}Ge_x$ layers on Si, the value of the strain shift coefficient b obtained for the Si-Si line is [88]:

$$b = -715 - 825x. \tag{2.35}$$

The value of b depends on the Ge content x and it is $-715\ cm^{-1}$ for bulk Si (x = 0). The variation of strain-shift coefficient of the optical modes in $Si_{1-x}Ge_x$ reported by several authors [88, 89, 104-109] is due to the different excitation wavelengths used for the Raman measurements [88]. The b values for Si-Si, Si-Ge, and Ge-Ge optic phonon modes are found -730 ± 70, -570 ± 50, and -450 ± 30, respectively [103, 110].

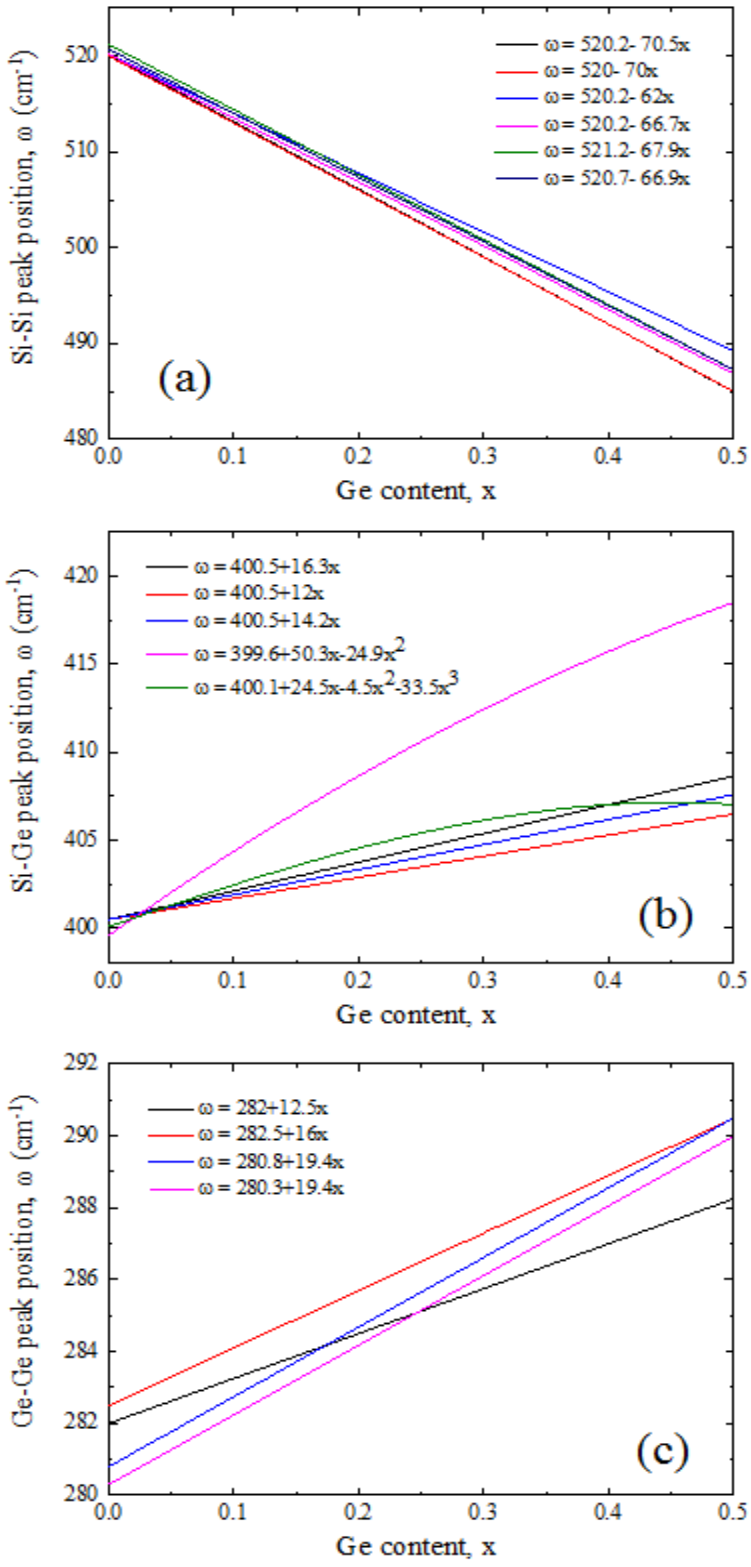

Figure 2.15 The peak position of the three optical modes (a) Si-Si, (b) Si-Ge, and (c) Ge-Ge of $Si/Si_{1-x}Ge_x$ NSs as a function of Ge content [14, 99].

2.3.2.2 Acoustic Modes in Si/SiGe NSs. Besides the first-order Raman peaks, acoustic phonon peaks are also observed in the low frequency Raman spectra of the SLs, as shown in Figure 2.16. The zone-edge acoustic phonon modes have been folded into the zone-center of the Brillouin zone due to the new periodicity of the SL and thus, folded doublets of longitudinal acoustic phonon peaks appear in the low-frequency region of Raman spectrum. The peaks of folded acoustic phonon modes are almost equally spaced in a SL with uniform layer thickness [111, 112].

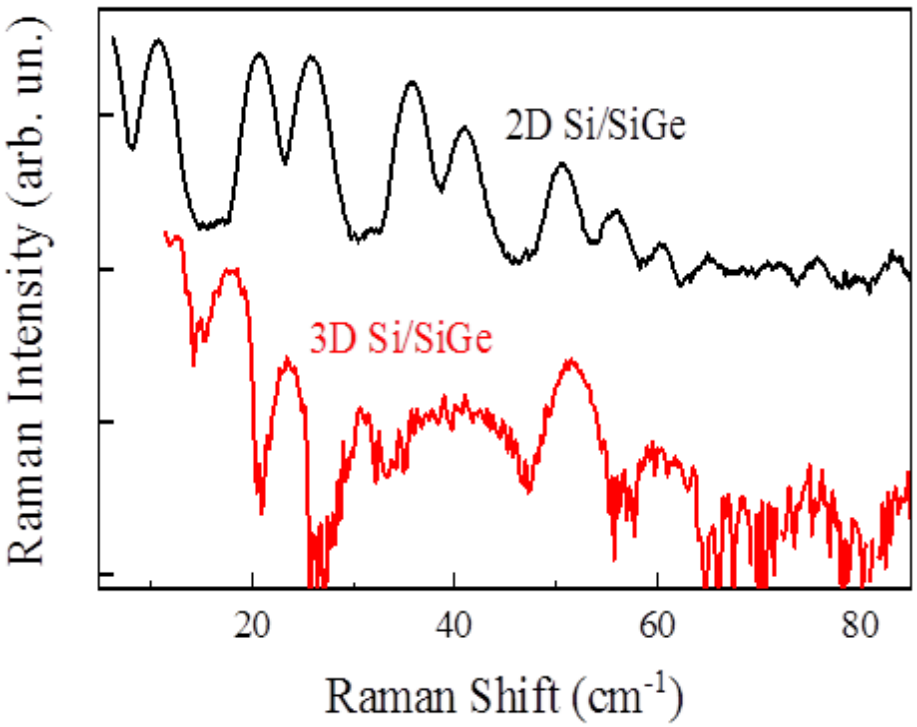

Figure 2.16 Low-frequency Raman spectra showing the acoustic modes in two different types of Si/SiGe SL.

Rytov's elastic continuum model [113] has been applied to explain the acoustic phonon modes in $Si/Si_{1-x}Ge_x$ NSs. The acoustic phonon dispersion according to this model is given by:

$$cos(qd) = cos\left(\frac{\omega d_1}{V_1}\right) cos\left(\frac{\omega d_2}{V_2}\right) - \frac{1}{2}\left(R + \frac{1}{R}\right) \times sin\left(\frac{\omega d_1}{V_1}\right) sin\left(\frac{\omega d_2}{V_2}\right), \quad (2.36)$$

where q is the wave vector of the SL perpendicular to the layers and is determined by:

$$q \cong \frac{4\pi\eta(\lambda)}{\lambda}\left[1 - \frac{1}{4[\eta(\lambda)]^2}\right], \quad (2.37)$$

where λ is the laser light wavelength and η(λ) is the refractive index of the material at that wavelength. In equation (2.36), R = $\frac{\boldsymbol{\rho_2 V_2}}{\boldsymbol{\rho_1 V_1}}$, and the superlattice periodicity, d = d_1 + d_2. d_1 and d_2, ρ_1 and ρ_2, V_1 and V_2 are the thicknesses, densities, and sound velocities of two constituent layers in the periodic multilayers structures [114].

In 3D (cluster-like) Si/$Si_{1-x}Ge_x$ NSs, the thickness of Si and $Si_{1-x}Ge_x$ layers fluctuates at the cluster peak and the valley due to uncontrolled SiGe interfiffusion during growth [9]. The varying thicknesses of the layers at the cluster peak and valley explain the broad FLA doublet which is reflected in the low-frequency Raman spectrum of 3D Si/SiGe NS in Figure 2.16. Phonon dispersion curves can describe the origin of broad FLA features explicitly.

Figure 2.17 shows the phonon dispersion relation in crystal, 2D, and 3D nanostructures. The zone edge of the first Brillouin zone in crystal structure is defined by π/a, where a is the lattice constant. In Si/SiGe NSs, the periodicity d is the summation of the thickness of Si (d_1) and SiGe (d_2) along the growth direction. The reduced minizone edge becomes at π/d instead of π/a.

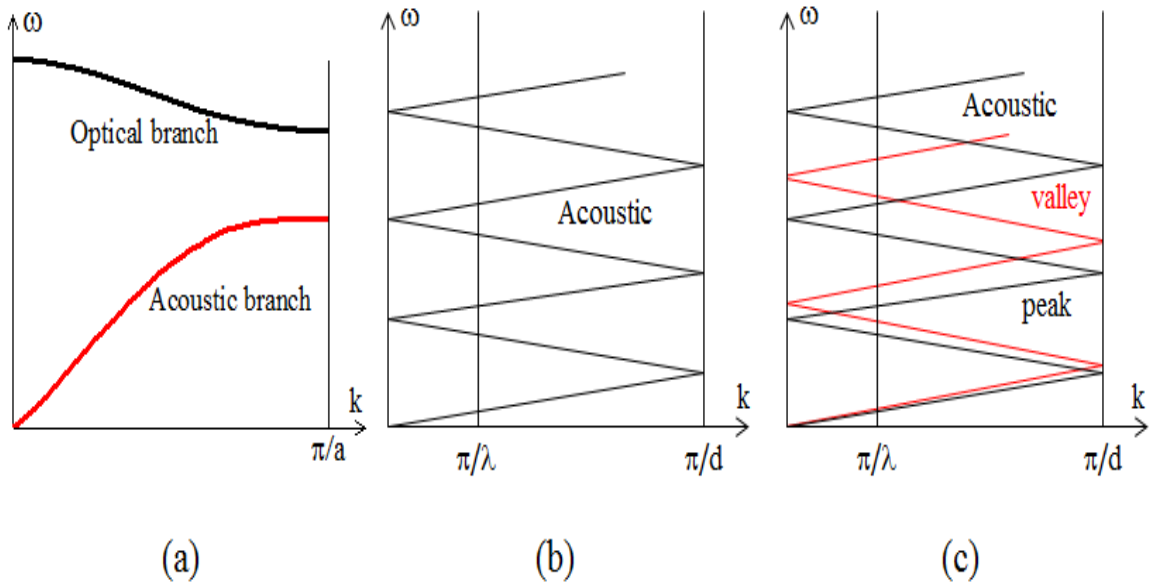

Figure 2.17 Phonon dispersion curve of (a) crystal structure. Acoustic-phonon dispersion of (b) 2D and (c) 3D NSs. The difference in thickness of layers at cluster peak and valley explains the broad and merged low-frequency peaks in 3D NS.

The acoustic branch frequency increases linearly and the slope represents the group velocity of phonons. The group velocity of optical phonon modes is negligible and therefore, they do not contribute to the heat transport.

2.3.2.3 Second-order Phonon Modes in Si/SiGe NSs. The second-order Raman spectra of crystalline Ge, Si, and Si_xGe_{1-x} alloys have been investigated and extensively studied to provide information about the density of states [90, 115-117]. Second-order Raman scattering in the two transverse optical (2TO) phonon region of Si is illustrated in Figure 2.18. Three distinct peaks are observed with Nd:YAG laser at 3.41 eV. The peak corresponds to two optical phonons at Γ develops above 2.81 eV excitation, which is due to the iterated first-order electron-phonon interaction with resonant intermediate states [116]. The 2TO(Γ) peak becomes sharper with increasing laser frequency and it has been

predicted that the stronger resonance of this peak is about ~ 4.1 to 4.3 eV for Si. The 2TO(W) peak disappears between 3.54 and 3.72 eV due to an iterated resonance with the intermediate states. The relative heights of the 2TO(L) peak becomes more than the 2TO(W) peak above 2.18 eV due to the enhancement of the scattering from phonons near 2TO(X) [117].

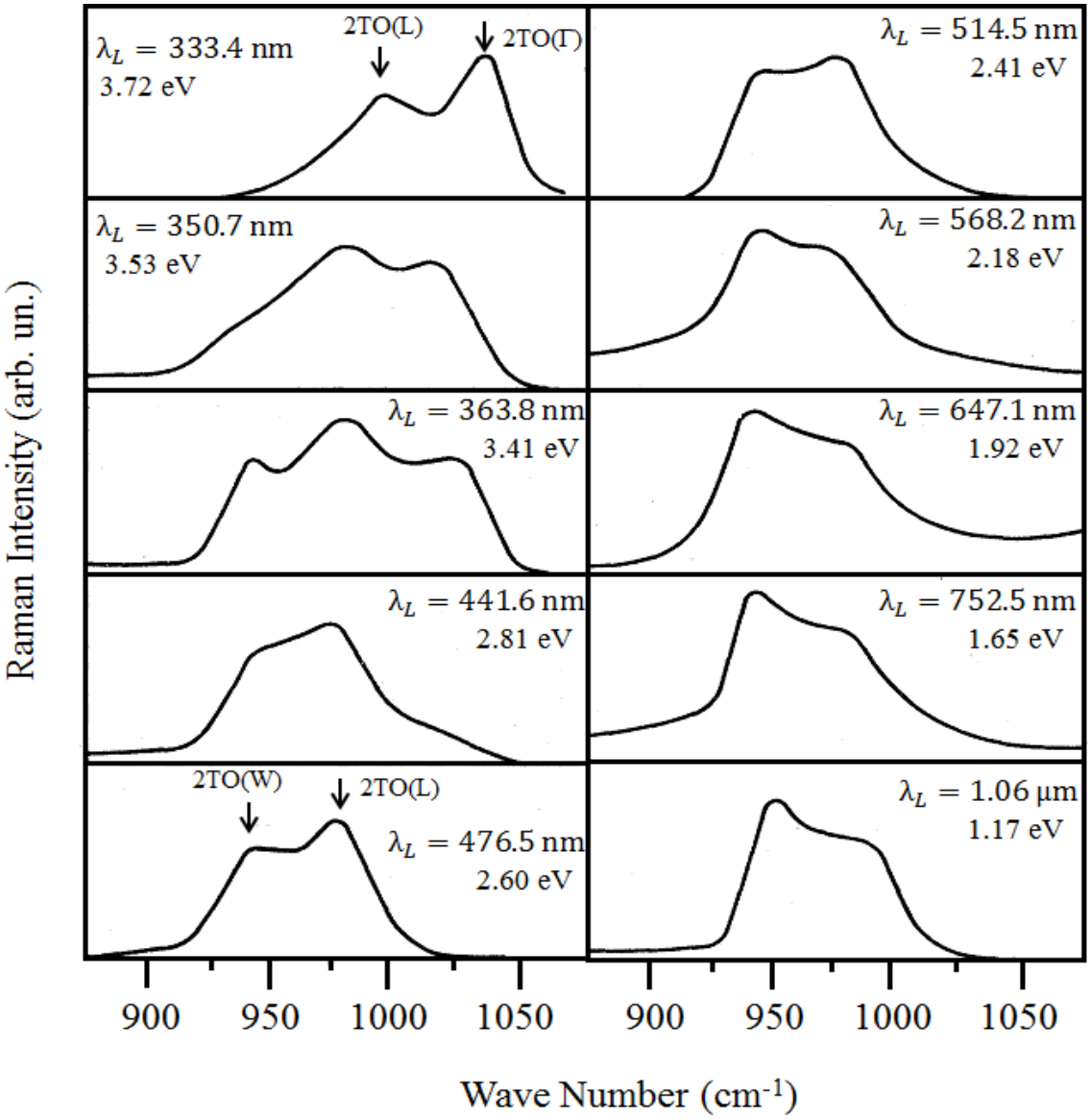

Figure 2.18 Second-order Raman spectra of Si in the region of overtone scattering by 2TO phonons for different laser frequencies [117].

Figure 2.19 shows the second-order 2TO Raman spectra of Ge and $Si_{1-x}Ge_x$ alloy. The effects observed in 2TO region of Ge are similar to that in Si. The most strongly contributing resonant gap of 2TO(Γ) peak is ~ 2.4 eV and this peak shifts to lower wave numbers with increasing laser frequency due to the change in resonant phonon momentum [116, 117].

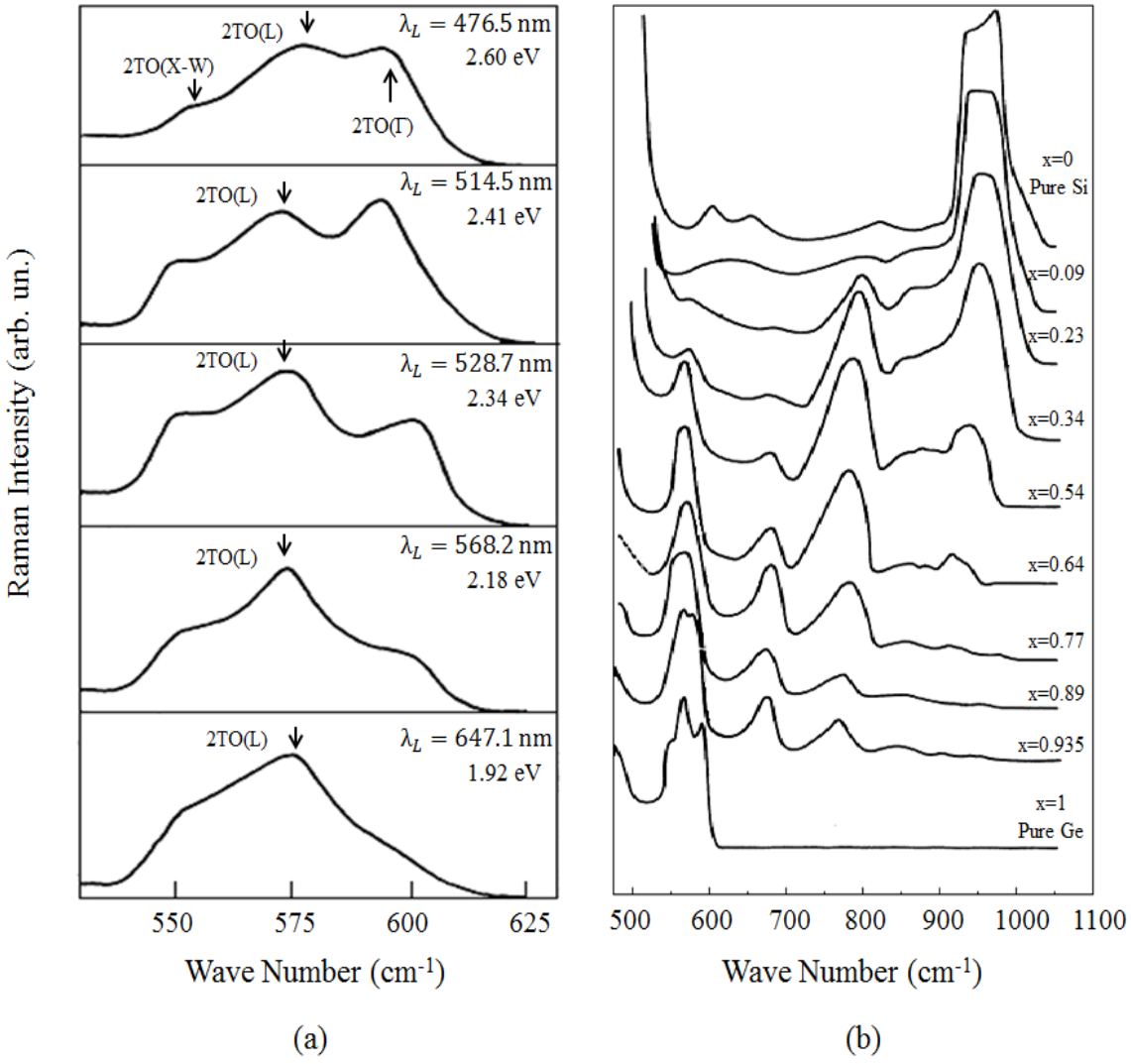

Figure 2.19 Second order Raman spectra in (a) Ge in the 2TO region for five different laser frequencies and (b) $Si_{1-x}Ge_x$ alloy with different Ge concentrations [90, 116].

Figure 2.19 (b) represents the effect of Ge concentration on the second-order Raman scattering of $Si_{1-x}Ge_x$ alloy. Three major peaks at ~ 570, 800, and 930-970 cm^{-1} are observed correspond to the overtone scattering by 2TO phonons of Ge, SiGe, and Si, respectively. When the Ge concentration is in the range of x = 0.54, a Raman feature at ~ 780 cm^{-1} is observed with the relative maximum intensity [90]. Besides these major peaks, few minor features at ~ 670-680 and 850-900 cm^{-1} are also observed. These weak features indicate additional structure in the overtone density of states. The peak at ~ 615 cm^{-1} is attributed to the combination of optical and acoustic phonon modes.

2.3.3 Photoluminescence Spectroscopy

Photoluminescence is one of the widely used nondestructive characterization techniques to analyze the properties of semiconductor nanostructure. It provides information to study both the intrinsic and extrinsic properties of semiconductors [118]. Photoluminescence concerns the excitation of charge carriers by the absorption of photons with energy above the band-gap of the material. Electron-hole (e-h) pairs are created and part of the e-h pairs recombines radiatively emitting a photon. The emitted photon can be collected and analyzed to yield significant information about the band structure of materials. The e-h pairs can also recombine through indirect transitions. Indirect transition requires the participation of phonons for the conservation of momentum. Since indirect transition involves the third particle (phonon), it is intrinsically less efficient than direct transition.

The photoexcited e-h pairs can recombine radiatively or non-radiatively. Non-radiative recombination mechanisms do not involve the creation of a photon. Non-radiative recombination dominates in indirect band gap semiconductors such as single-

crystal Si and Ge. In indirect band gap semiconductors, the minimum of the conduction band and the maximum of the valence band are not at the same location in reciprocal space. Thus, the participation of a phonon (a second-order process) is required for radiative recombination across the band gap. As a result, the radiative recombination lifetime is much longer and indirect band gap semiconductors exhibit poor photoluminescence efficiency [119]. The internal quantum efficiency is given by:

$$\eta_{in} = \frac{\tau_{non-rad}}{\tau_{non-rad} + \tau_{rad}}, \tag{2.38}$$

where τ_{rad} and $\tau_{non\text{-}rad}$ are the lifetimes for the radiative and non-radiative recombination pathways. The study of recombination paths could infer significant information about the lifetime, quantum efficiency, and diffusion length [118]. The recombination at bulk or surface defects and Auger recombination do not involve emitting photons, are considered as non-radiative recombination.

Features of the PL spectra are used to identify the surface, interface, and impurity levels and also to measure the dislocations in the alloy structure and interface roughness. The PL intensity provides a measure of the relative rates of radiative and non-radiative recombination. Figure 2.20 shows the energy band diagram of c-Si and a low-temperature (4 K) PL spectrum of c-Si, where transverse optical (TO), transverse acoustic (TA), and combination of two transverse optical (2TO) phonon-assisted peaks are clearly observed. The no-phonon (NP) PL peak at 1.16 eV associated with the direct carrier recombination due to the selection rule relaxation is insignificant, as shown in Figure 2.20 (b) [50, 120].

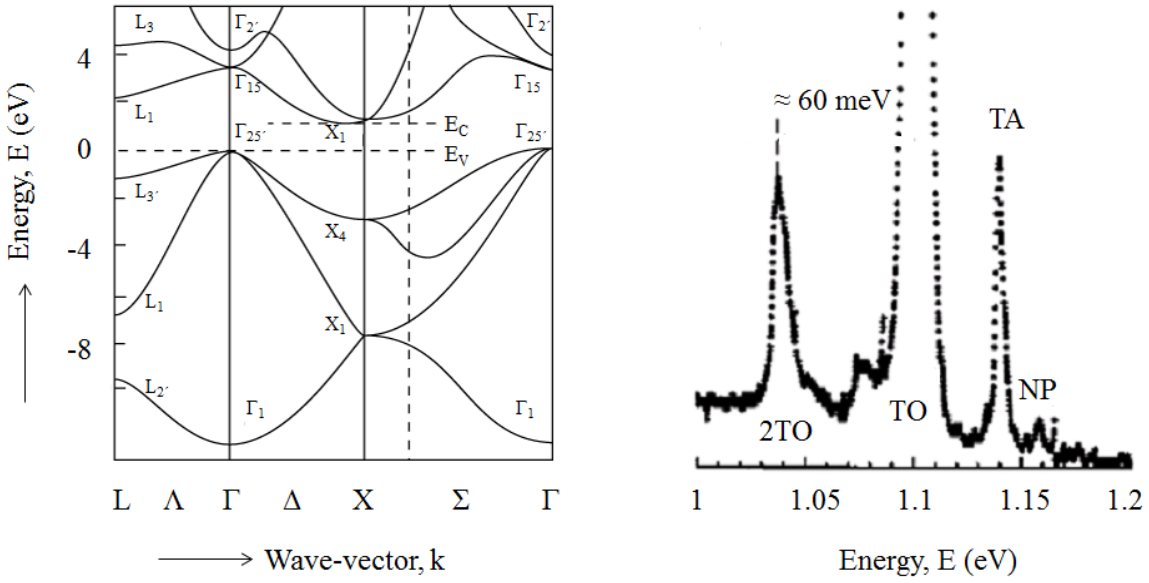

Figure 2.20 (a) Band-structure [119] and (b) low-temperature PL spectrum [120] in c-Si. Radiative recombination involving at least one phonon is much stronger than the NP emission.

In Si/SiGe nanostructures, the selection rule becomes relaxed and it is possible to achieve higher PL quantum efficiency compared to the indirect band gap semiconductors. The intensity ratio between NP to phonon-assisted PL emission in Si/ SiGe NSs is remarkably improved compared to that in c-Si as shown in Figure 2.21. The PL signal of WL, which appears first in the growth of SiGe islands, shows two strong peaks of NP and TO phonon emission located approximately 0.1 eV below the bulk Si phonon replica [121]. A weak shoulder due to the TA phonon assisted emission is also observed. In $Si/Si_{1-x}Ge_x$ NSs, the PL signal is strongly depends on the alloy composition and the strain. As the Ge coverage increases, the PL peak at ~ 0.8 eV associated with SiGe islands appears. It is difficult to resolve the NP and TO peaks in SiGe due to the band

broadening caused by the non-uniform size, shape, and composition of the islands [121, 122].

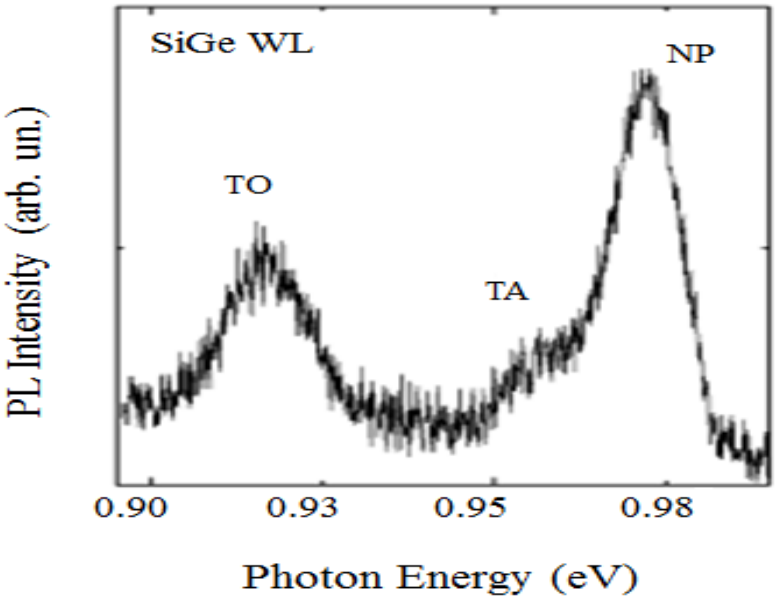

Figure 2.21 Low temperature PL spectra of SiGe WL showing the intensity ratio between NP and TO phonon PL peaks [120].

CHAPTER 3

EXPERIMENTAL METHODS

3.1 Introduction

$Si/Si_{1-x}Ge_x$ NSs with different structural parameters studied in this thesis were fabricated by MBE in NRC, Canada. Optical measurements of these samples were performed using Raman and PL spectroscopy in Dr. Tsybeskov's Lab. Raman spectra were measured at room temperature using a CW Ar^+ laser with different excitation wavelengths in a wide spectral range (0-1200 cm^{-1}). PL spectra are recorded at low temperature (17 K) using a CW Ar+ laser (514, 488, and 457.9 nm), a HeCd laser (325 nm), and high-power light-emitting diode with a peak near 365 nm. The PL dynamics were also measured using the 3rd harmonic (355 nm) of a Q- switched Neodymium doped Yttrium-Aluminium-Garnet (Nd:YAG) pulse laser.

3.2 Samples

$Si/Si_{1-x}Ge_x$ ($0.2 < x < 0.5$) samples were grown by MBE in a VG Semicon V80 system on Si (001) substrates at a temperature of ~ 550−600 ^oC [123]. All samples are characterized using TEM performed on a JEOL JEM-2100F field emission source electron microscope operating at 200 kV. EDX spectroscopy with an Oxford INCA Energy TEM 200 attached to the JEM-2100F has been used to analyze the chemical composition of the samples. The structural properties of the samples obtained from TEM and EDX data are presented in Table 3.1.

Table 3.1 Structural Details of Multilayer $Si/Si_{1-x}Ge_x$ NSs

Sample No.	**x in $Si/Si_{1-x}Ge_x$** (EDX data)	**No. of Period** N
1810 (S1)	~ 0.35	10
1834 (S2)	~ 0.4	9
1830 (S3)	~ 0.5	8
1831 (S4)	~ 0.4	10

The first sample (S1) is grown on a c-Si substrate and comprises a $Si/Si_{1-x}Ge_x$ 10 period superlattice (SL) with ~ 5 nm thick $Si_{1-x}Ge_x$ layers and x approaching 35% (Figures 3.1 (a), 3.2 (a)). The second sample (S2) is a multilayer $Si/Si_{1-x}Ge_x$ cluster sample with x ~ 40%, a typical cluster height of ~ 10 nm, a second-to-top $Si_{1-x}Ge_x$ cluster layer approximately three times thicker than those below, and a 15 nm thick Si separating layer closer to the c-Si substrate (Figures 3.1 (b), 3.2 (b)). This design is introduced for the purpose of creating a non-homogeneous in-depth strain distribution [124]. The third sample (S3) is a $Si_{1-x}Ge_x$ 50 nm thick NL grown on top of $Si/Si_{1-x}Ge_x$ cluster multilayers with x ~ 50% [see Figure 3.1 (c); x is confirmed by EDX]. In these samples, the top SiGe NL is expected to have different properties compared to SiGe NLs grown directly on a c-Si substrate.

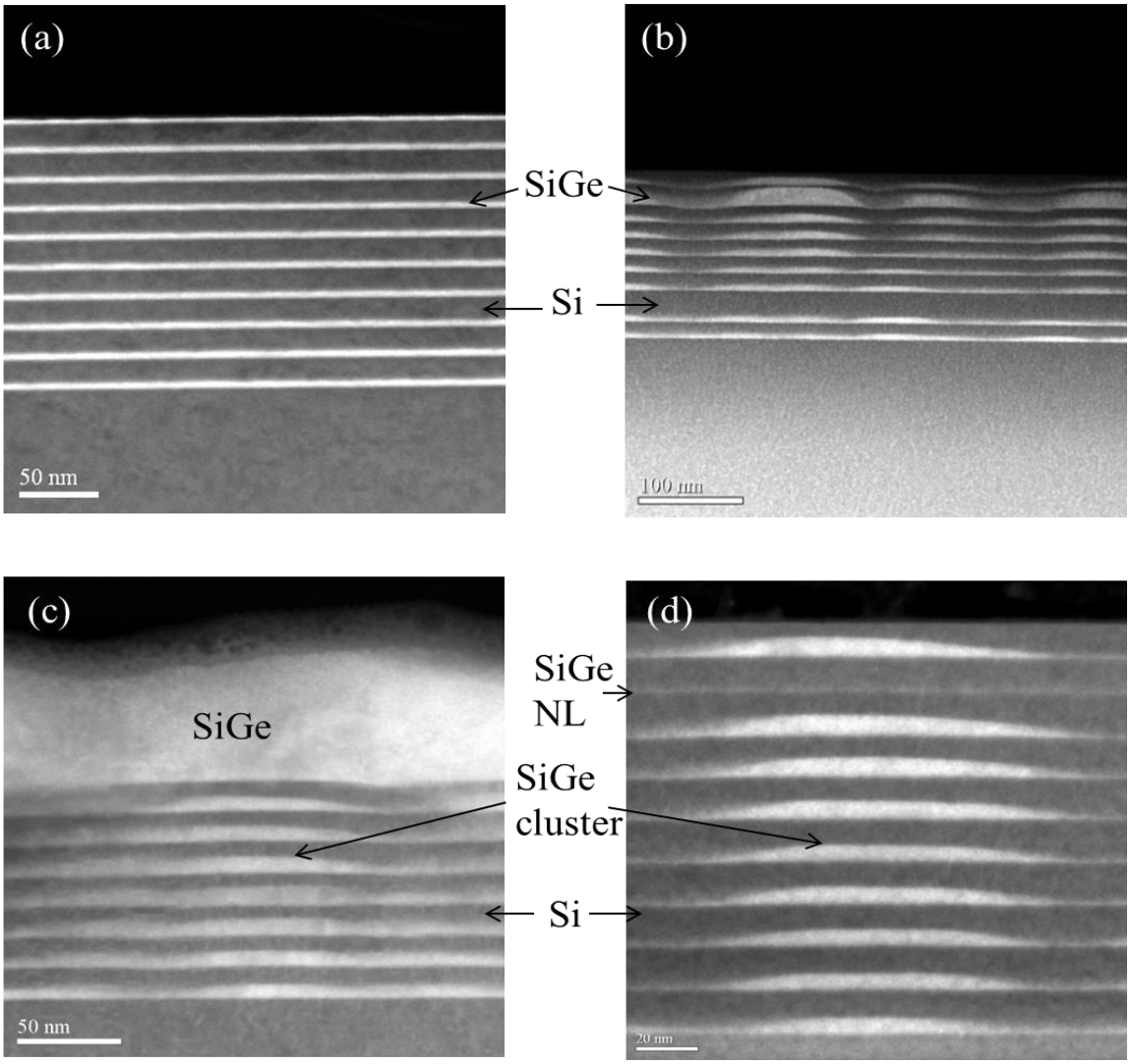

Figure 3.1 Cross-sectional TEM images of MBE grown samples: (a) planar $Si/Si_{0.65}Ge_{0.35}$ SL (sample S1), (b) $Si/Si_{0.6}Ge_{0.4}$ CMs (sample S2), (c) a 50 nm thick, partially relaxed $Si_{0.5}Ge_{0.5}$ alloy layer on top of $Si/Si_{0.5}Ge_{0.5}$ CMs (sample S3), and (d) a single $Si_{0.92}Ge_{0.08}$ NL sandwiched between $Si/Si_{0.6}Ge_{0.4}$ clusters.

The EDX data for the $Si_{1-x}Ge_x$ layers (Figure 3.2) show a continual increase in Ge composition (x) reaching a maximum value close to the middle of a $Si_{1-x}Ge_x$ layer (or cluster), most likely due to Si/SiGe intermixing during growth. The fourth sample (S4) consists of a Si substrate; a $Si_{1-x}Ge_x$ buffer layer with $x \approx 10\%$, 8 repeats of layers of Si and $Si_{1-x}Ge_x$ clusters (up to 10 nm thick); a single 3–5 nm thick $Si_{1-x}Ge_x$ NL enclosed in

Si; and a final $Si_{1-x}Ge_x$ cluster layer topped with a Si capping layer, as shown in Figure 3.1 (d). EDX measurements (Figure 3.2 (c)) confirmed the size of the SiGe clusters and NL obtained from the TEM measurements. Also, they show that the $Si_{1-x}Ge_x$ NL composition is relatively uniform (with $x \approx 8\%$) while in the $Si_{1-x}Ge_x$ clusters x gradually increases from 5% at the SiGe cluster/Si interface to up to 40% close to the cluster center (Figure 3.2 (c)).

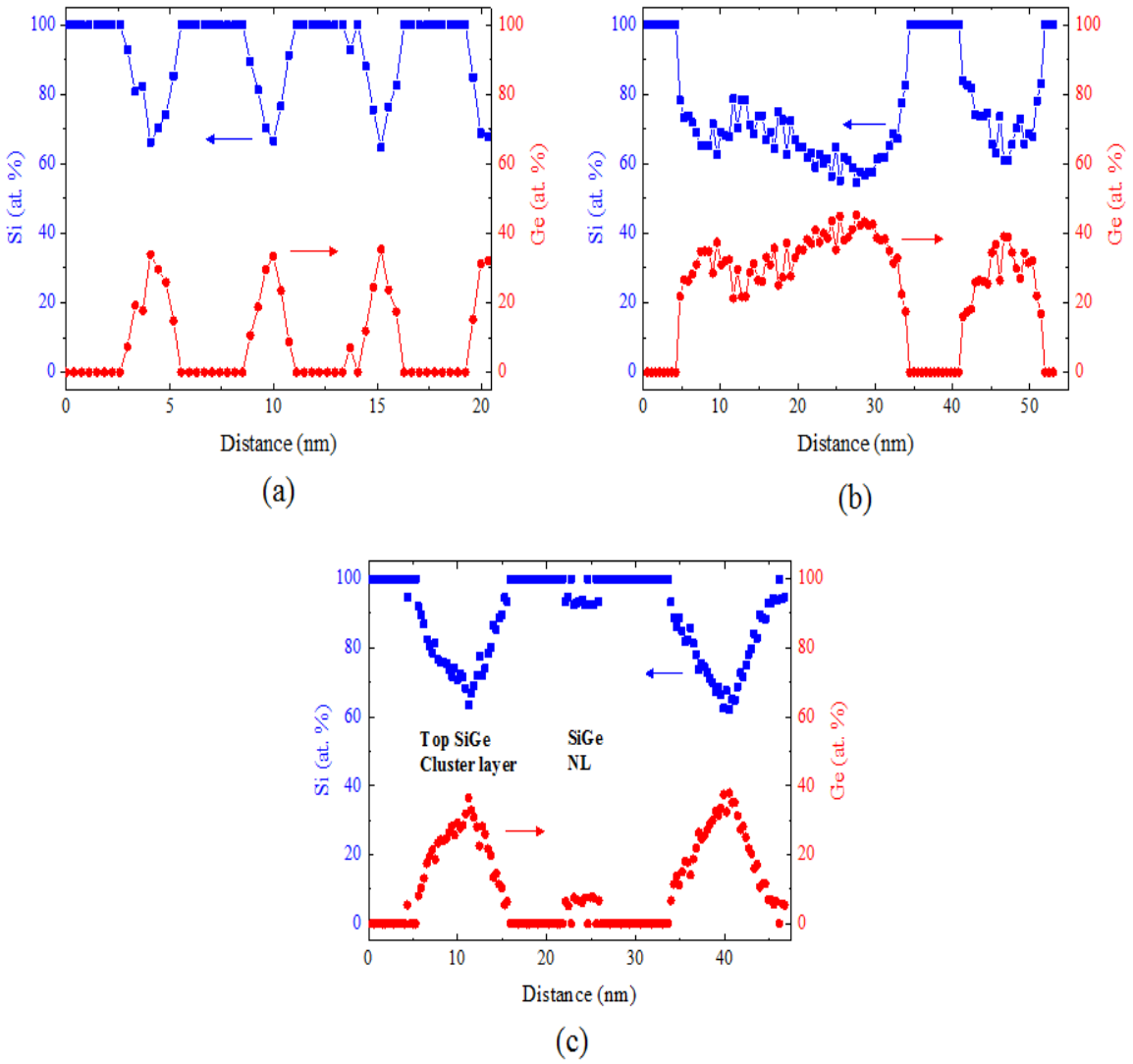

Figure 3.2 EDX measured composition of topmost layers of samples (a) S1, (b) S2, and (c) S3.

3.3 Experimental Setup and Measurement Procedures

3.3.1 Raman Spectroscopy

Figure 3.3 shows the experimental setup for Raman measurements. Raman spectra are recorded at room temperature using an Ar^{+} laser as an excitation source. The used excitation wavelengths were 457.9, 488, and 514.5 nm. The measurements are performed with the incident light at an angle close to ~ 78^{o} (Brewster angle in c-Si), and the laser beam was focused to a spot of approximately 10 μm in diameter. The laser power varied from ~1 W (514.5 nm) to ~0.3 W (457.9 nm) and the power on the sample was ~ 200 mW at 457.9 nm excitation wavelength with 30 μm slit width. The scattered light from the sample is focused onto the entrance slit of 150 μm of a Jobin Yvon U1000 double monochromator with 1 m focal length [125] and detected by a thermoelectrically cooled Hamamatsu R943-02 photomultiplier tube (PMT) and a photon counting system. The PMT has wavelength range at maximum spectral response of 300 – 850 nm and a dark current of 20 counts per second [126]. The Raman system spectral resolution is ~ 0.5 cm^{-1}.

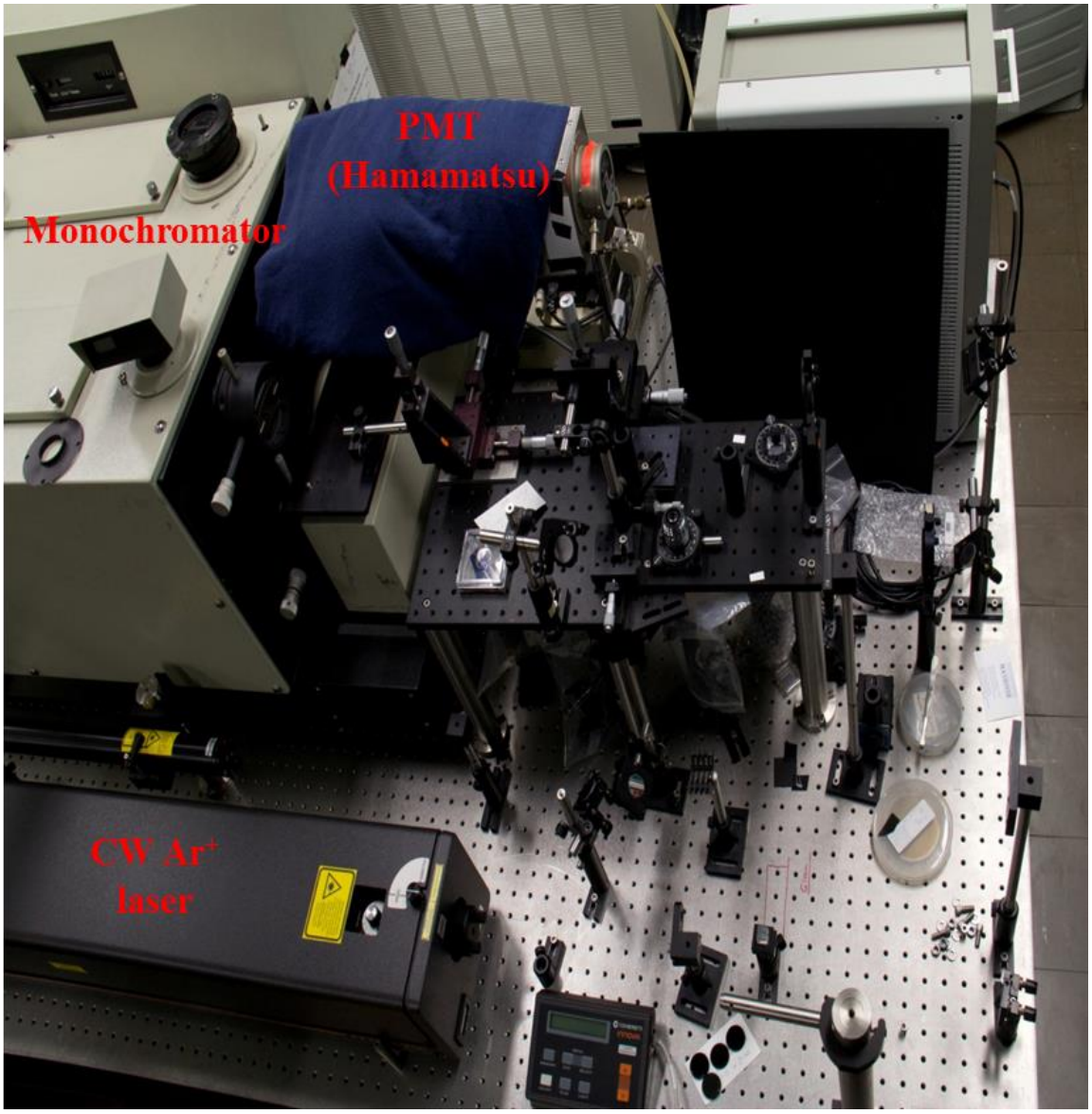

Figure 3.3 Experimental setup for Raman measurements.

Raw data of Raman spectrum in $Si/S_{0.65}Ge_{0.35}$ SL is shown in Figure 3.4 (a). The baseline observed in the obtained Raman spectra may tend to obscure the Raman features. The sample surface imperfection and significant instrument response associated with the stray light could play a major role to the change in the baseline of the Raman scattering. Therefore, an elevation of the intensity of the baseline data points is observed

in the Raman spectrum. This elevation of Raman peak intensity impedes the correct analysis of the sample [127] and makes it difficult to detect weak Raman features. In this study, the correction of the measured Raman spectra is performed after proper determination, fitting, and subtraction of the corresponding baseline (see Figure 3.4 (b)).

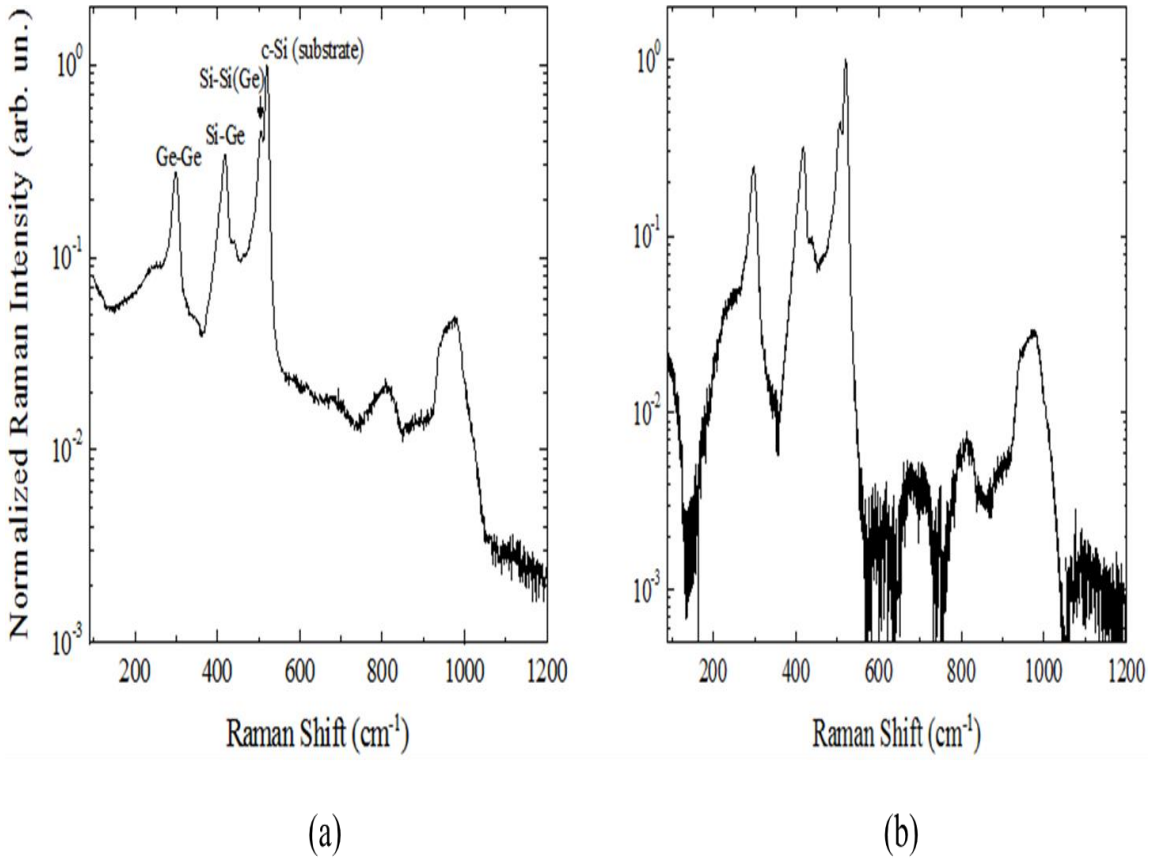

Figure 3.4 The Raman spectrum of $Si/Si_{0.65}Ge_{0.35}$ SL (a) before and (b) after the baseline correction.

Figure 3.5 presents the schematics of heat transport in samples S1 and S2. The temperature gradient observed between different parts of the sample, which can be determined by using the ratio of Stokes/anti-Stokes Raman peak intensities associated

with different vibration modes (i.e., Raman scattering thermometry) [128]. According to the Fourier law of heat conduction, the thermal conductivity can be calculated using:

$$\kappa = P \times \frac{L}{A} \times \frac{1}{\Delta T}, \tag{3.1}$$

where P is the laser power absorbed by a sample with a thickness (L) in the direction normal to a surface of a cross-sectional area (A) due to a temperature gradient (ΔT). For Raman measurements in $Si/Si_{1-x}Ge_x$ NSs, an intense and focused laser beam with a short penetration depth is used and a hot spot close to the sample surface is created. In general, heat can dissipate vertically (across-plane direction) and laterally (in-plane direction). However, it is reasonable to assume that heat dissipation is mostly controlled by a heat flow in the across-plane direction in the samples, because the c-Si substrate thermal conductivity is ~10 times better than that of a SiGe NS, and entire thickness of the sample is in the order of 150 nm [75, 129]. Thus, the temperature gradient is established between the highest temperature at the sample surface and the lowest temperature of the sample c-Si substrate, and these temperatures can be estimated from the Stokes/anti-Stokes Raman peak intensity ratio for strained Si and Si-Ge phonon modes and the Si-Si mode at 520 cm^{-1}.

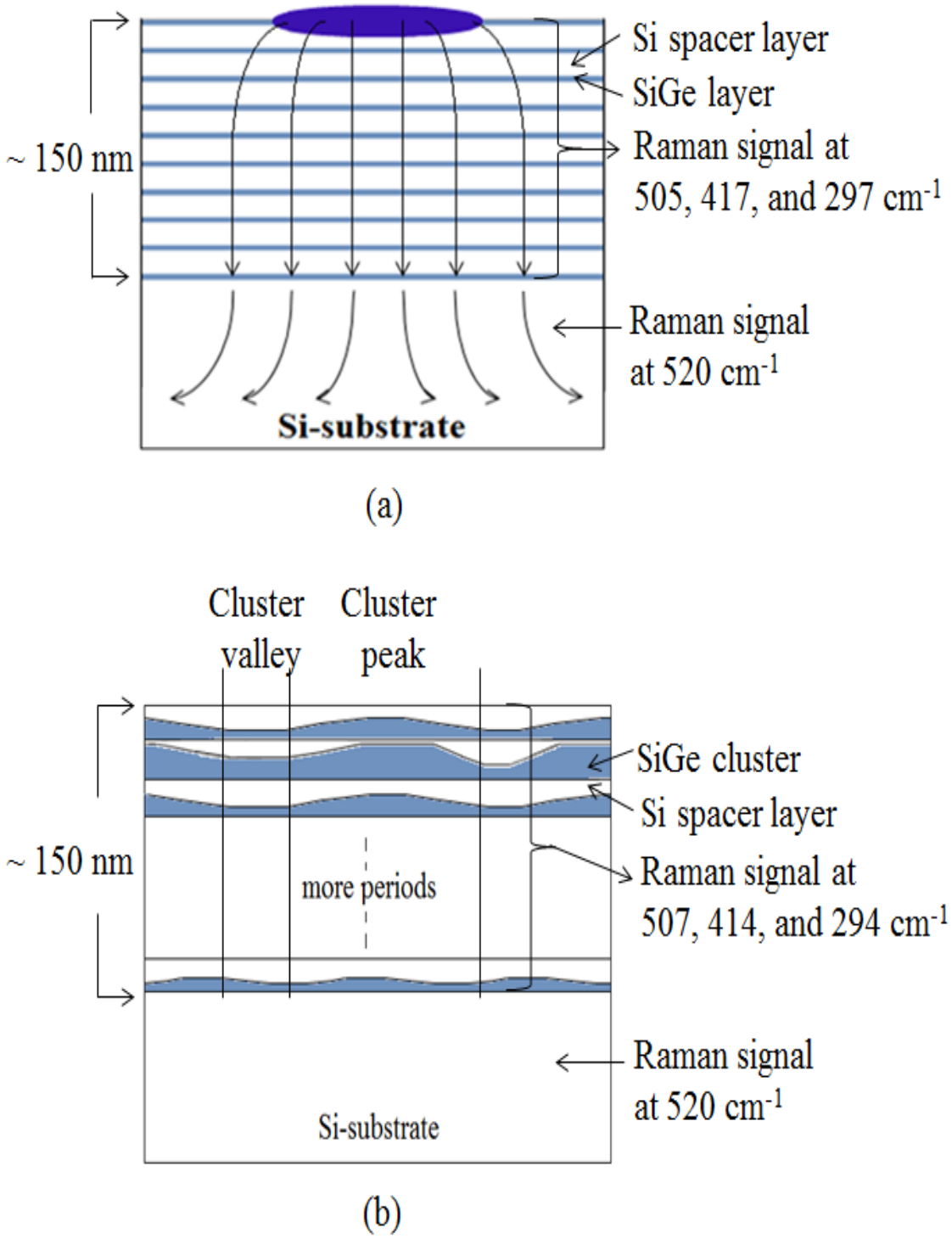

Figure 3.5 A model for heat dissipation in samples (a) S1 and (b) S2.

3.3.2 Photoluminescence Spectroscopy

The PL measurements of the Si/SiGe NSs were performed at low temperatures using a He closed-cycle optical cryostat with temperature of $T \geq 15$ K. For CW and near steady-state excitation, an Ar^+ laser (514 nm, 488 nm, 457.9 nm, and a multi-line), a HeCd laser (325 nm), a high-power light-emitting diode (LED) with a peak near 365 nm, a mechanical chopper and a lock-in amplifier were used. For PL measurements under pulsed laser excitation, the third harmonic of a Nd:YAG laser with a wavelength of 355 nm, 6 ns pulse duration, and 10 Hz repetition rate was used. The time-resolved PL signal from PMT in PL decay measurement was averaged over 1000 sweeps using LeCroy 9310M 300 MHz digital oscilloscope. The background signal was measured independently and subtracted carefully. The overall time resolution of the entire system was 2.5 ns. The excitation intensity was varied from 0.1 to 10 W/cm^2 for CW PL measurements, 0.15 to 5 mJ for time resolved PL measurements. The PL signal was dispersed by a 0.5 meter single grating Acton Research spectrometer, and the dispersed signal was detected by a thermo-electrically cooled InGaAs Hamamatsu PMT in the spectral range of 0.9-1.65 μm using standard lock-in configuration. The experimental setup for PL measurements is presented in Figure 3.6.

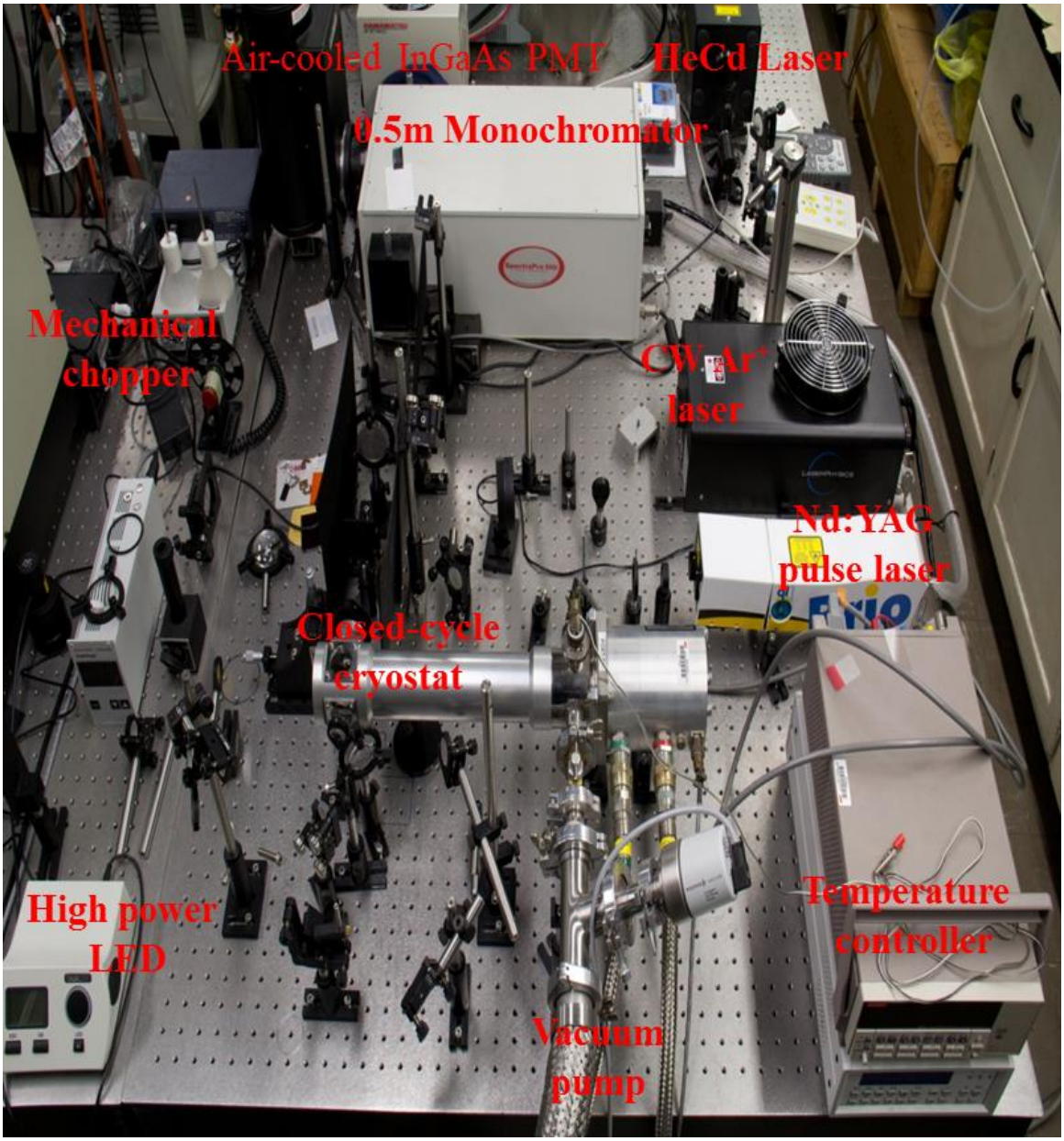

Figure 3.6 Experimental setup for PL measurement.

CHAPTER 4

RESULTS AND DISCUSSION

This chapter presents Raman and PL studies of structural, optical, and thermal properties of the MBE grown $Si/Si_{1-x}Ge_x$ ($0.2 < x < 0.5$) NSs. In the first section, experimental results from Raman spectroscopy will be presented, and the quantitative and qualitative analysis of Raman data will be discussed. The Raman peaks associated with low-frequency, first-order, and second-order Raman scattering are determined to explain structural, vibrational, and thermal properties of Si/SiGe NSs. The experimental results from PL spectroscopy will be presented in the second section of this chapter. The CW lasers and third harmonic (355 nm) of Nd:YAG pulsed laser have been used for PL excitation and electron-hole recombination schemes have been discussed and modeled.

4.1 Raman Measurements in Si/SiGe NSs

Raman measurements were performed at room temperature in three different types of $Si/Si_{1-x}Ge_x$ NSs: 2D planar $Si/Si_{0.65}Ge_{0.35}$ SLs (sample S1), 3D non-uniform $Si/Si_{0.6}Ge_{0.4}$ CMs (sample S2), and $Si_{0.5}Ge_{0.5}$ alloy layer on top of $Si/Si_{0.5}Ge_{0.5}$ CMs (sample S3). Low-frequency, first-order, and second-order Raman spectra (Stokes and anti-Stokes) for these samples are recorded using different excitation wavelengths (457.9, 488, and 514.5 nm). Baseline correction has been performed to measure the Raman peak's position, spectral shape, and intensity with accuracy. The comprehensive studies of strain, chemical composition, intermixing, FLA phonons, thermal conductivity, and heat dissipation in $Si/Si_{1-x}Ge_x$ NSs are presented in details and combined with high resolution transmission

electron microscopy. The sample chemical composition has been calculated using two methods: Raman peak intensity and peak position. The relative Raman intensities are calculated using scattering-volume relation and compared with the experimental data. Low-frequency FLA phonon peaks in 2D and 3D Si/SiGe NSs are explained by calculating the phonon dispersion curve using Rytov's elastic continuum model. The local temperature and thermal conductivity are predicted from the Stokes/anti-Stokes Raman spectra and used to explain the heat dissipation in different types of Si/SiGe NSs.

4.1.1 Results

Figure 4.1 shows Raman spectra in c-Si and S1-S3 in a wide spectral range (0-1200 cm^{-1}) covering low-frequency (<100 cm^{-1}), first- and second-order Raman scattering spectral range in Si, Ge, and $Si_{1-x}Ge_x$. All Raman spectra are normalized and shifted vertically for clarity, and the signal-to-noise ratio is approaching 10,000.

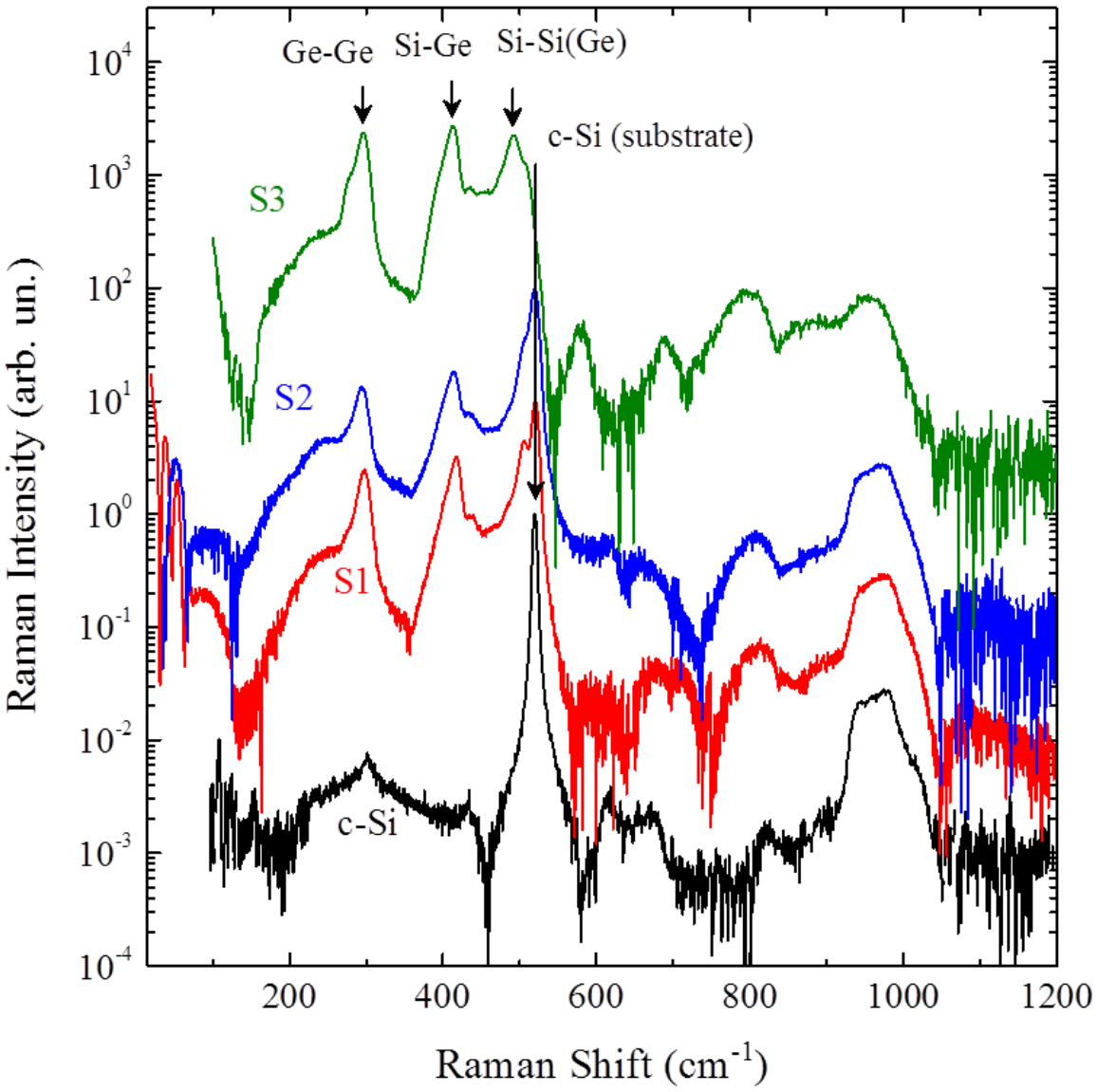

Figure 4.1 Raman spectra at room temperature measured using 457.9 nm excitation in c-Si and samples S1-S3 after baseline correction (spectra shifted vertically for clarity).

In c-Si, three major Raman features are found associated with second-order scattering from acoustic phonons (at ~300 cm^{-1}), first (at ~520 cm^{-1}), and second (at ~1000 cm^{-1}) order scattering from optical phonons [115]. In S1-S3, three clearly distinct major peaks are observed at ~295, 415, and 500-520 cm^{-1}, and they correspond to first-order Ge-Ge, Si-Ge, and Si-Si optical phonon modes, respectively [95]. Raman peaks

associated with second-order inelastic light scattering include the feature at ~600 cm^{-1} associated with a combination of Ge optical and Si acoustic phonons [90] and the signal between 700 and 1100 cm^{-1} attributed to second-order Raman scattering involving $Si_{1-x}Ge_x$ and Si phonons [90, 115, 116].

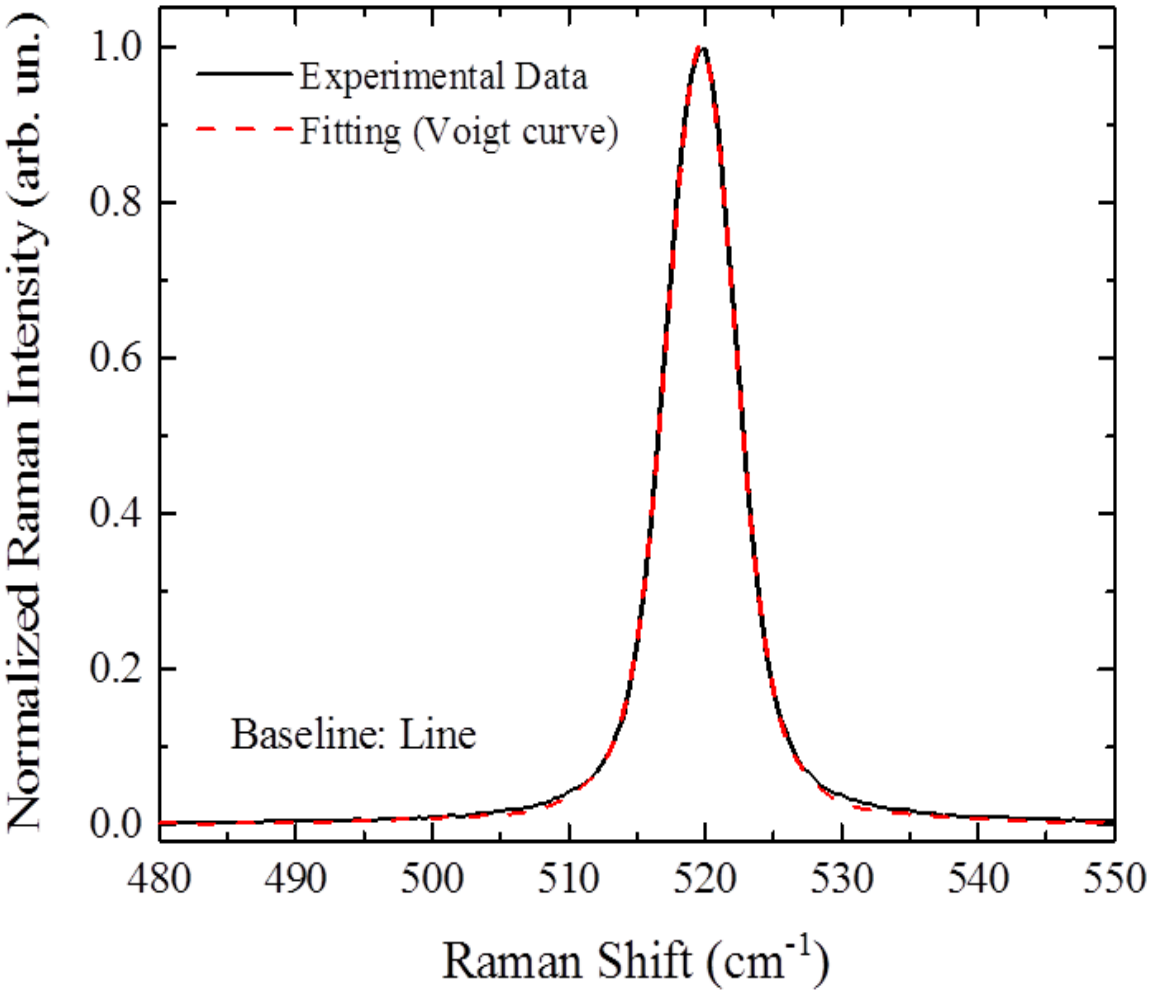

Figure 4.2 Normalized Raman spectrum at room temperature measured using 457.9 nm excitation in c-Si after baseline correction is fitted with a Voigt curve (dashed line).

The major Raman peak in c-Si observed at 520 cm^{-1} is well fitted by a Voigt peak with a full width at half maximum (FWHM) of ~5 cm^{-1} as shown in Figure 4.2. In S1 and S2, the FWHM of the 520 cm^{-1} Raman peak is found to be ~5.5 cm^{-1} and ~6 cm^{-1}, respectively. In both samples, in addition to the major peak at ~ 520 cm^{-1}, a much weaker peak at 505-506 cm^{-1} attributed to strained Si is observed [50]. A curve fitting procedure indicates that the FWHM of the 505-506 cm^{-1} peak precisely correlates with the FWHM of the major Raman peak at 520 cm^{-1}. It is concluded that in S1 and S2, the Raman peak at 520 cm^{-1} is associated with the c-Si substrate directly underneath of Si/SiGe NSs, and the Raman peak at 505 cm^{-1} is associated with Si layers separating SiGe layers (or SiGe cluster layers). Also, it is found that in S1 and S2, Si layers separating SiGe layers are mostly strained (not equally strained-compressed as suggested in the references [49, 50]), and in S1 the Si layer strain is more homogeneous compared to that in S2.

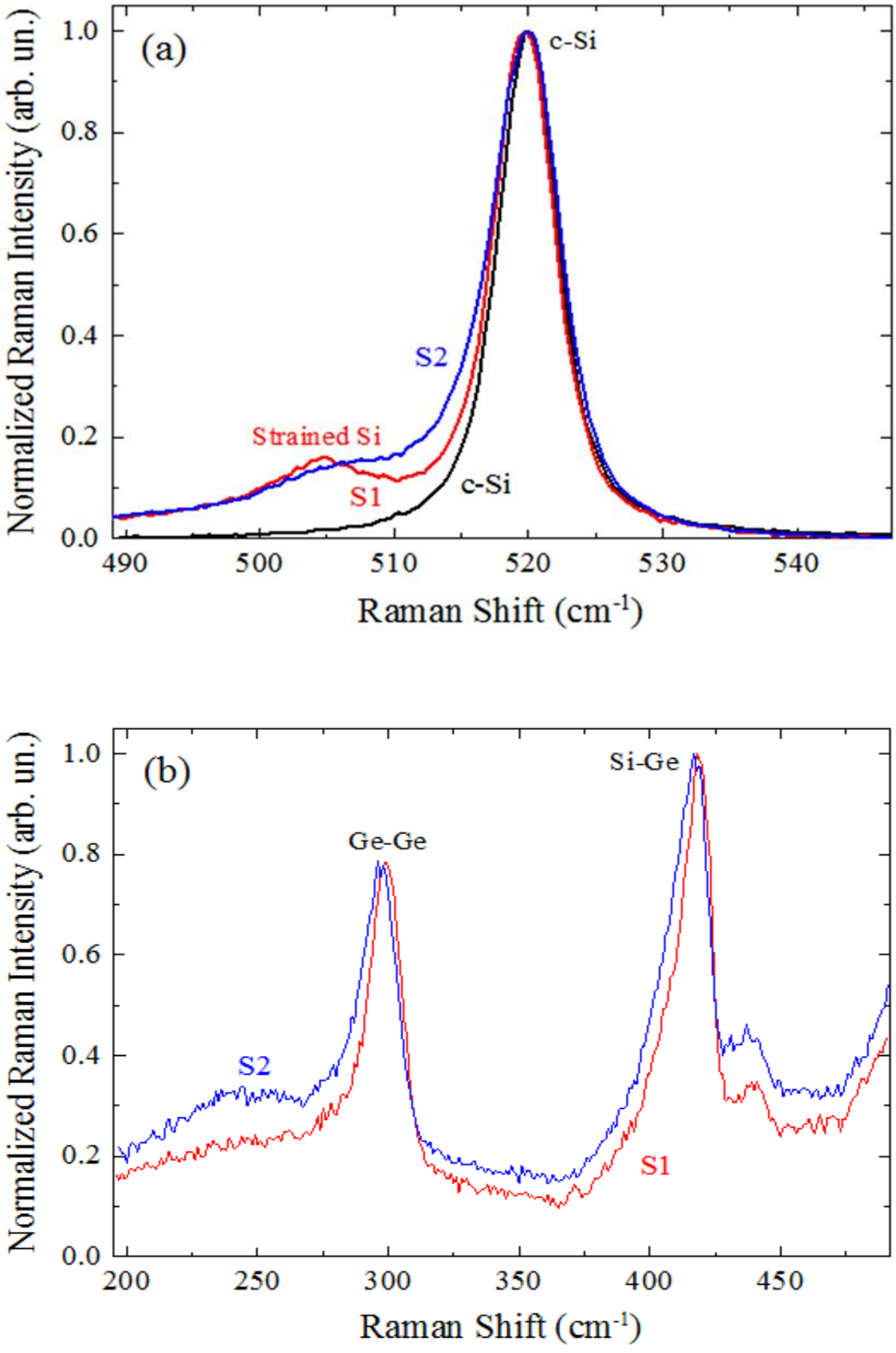

Figure 4.3 Room temperature Raman spectra measured using 457.9 nm excitation of samples S1 and S2 in the vicinity of (a) the Si-Si vibration mode compared with that of c-Si and (b) the Si-Ge and Ge-Ge vibration modes.

Raman spectra in S1 and S2 associated with Si-Ge and Ge-Ge vibrations are shown in Figure 4.3 (b). In both samples, Si-Ge Raman signals are peaked at 417-418 cm^{-1} and Ge-Ge are peaked at 298-299 cm^{-1}. In S2, the Si-Ge and Ge-Ge peaks are broader by ~ 3 cm^{-1} compared to that in S1. Also, these peaks are slightly shifted toward lower wavenumbers in the case of S2 compared to S1, which could be due to the higher Ge composition (*x*). In addition, the Raman spectra show weaker and broader peaks at ~ 250 cm^{-1} attributed to the resonant Ge vibrational mode and 438 cm^{-1} associated with the local Si vibrational mode in the presence of Si and Ge, respectively [90, 100]. These peaks are enhanced in sample S2 compared to sample S1, most likely due to the higher Ge composition (*x*) (see Figures 3.2 (a) and (b)).

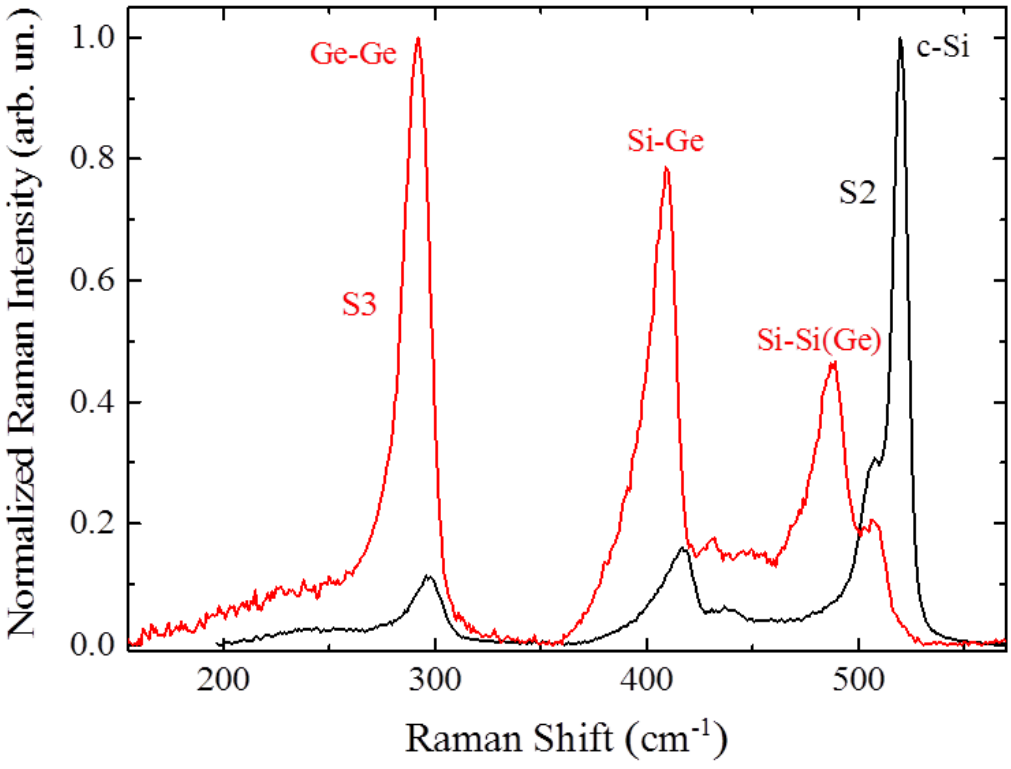

Figure 4.4 Comparison of normalized Raman spectra on a linear intensity scale measured using 457.9 nm excitation in samples S2 and S3.

The major Raman peaks in S2 and S3 obtained using excitation at a wavelength of 457.9 nm are compared in Figure 4.4. In S3, a strong peak at ~488 cm^{-1} is found and attributed to the Si-Si phonon band of a SiGe alloy layer [99]. No scattering from the c-Si substrate at 520 cm^{-1} is ovserved, which is the result of a stronger absorption of 457.9 nm light by a thicker $Si_{1-x}Ge_x$ layer with x ~ 50%. In addition, the strained Si peak is observed at ~508 cm^{-1}. The Raman signal at ~ 488 cm^{-1} is not observed in S2 with thinner $Si_{1-x}Ge_x$ alloy layers and x ~ 40% while the Raman peak from the c-Si substrate is the dominant one. The other two main Raman features at 409 cm^{-1} (Si-Ge vibration mode) and at 292 cm^{-1} (Ge-Ge vibration mode) are more pronounced and slightly shifted toward lower wavenumbers in S3 compared to S2, which is also due to a higher Ge concentration.

Figure 4.5 (a) compares normalized Raman spectra in S3 measured using 488 and 457.9 nm excitation wavelengths in the range of first- and second-order Raman scattering. As the excitation wavelength increases, the light penetration depth increases, and a low intensity Raman signal from c-Si at 520 cm^{-1} is observed with excitation at 488 nm. However, the dominant Raman signal is still associated with the three major vibration modes: the local Si-Si mode in the presence of Ge at ~490 cm^{-1}, Si-Ge vibration at 409 cm^{-1}, and Ge-Ge vibration at 292 cm^{-1}. Figure 4.5 (b) focuses on second-order Raman spectra in S3 excited at the two wavelengths and compare them to that in c-Si. In addition to the three major Raman peaks at ~ 575, 715-830, and 910-1000 cm^{-1}, weaker Raman features at ~ 680 cm^{-1} and in the range of 840-900 cm^{-1} are observed. They are, most likely, overtones of the first-order Ge-Ge (in the presence of Si) and local Si-Si (in the presence of Ge) modes [90].

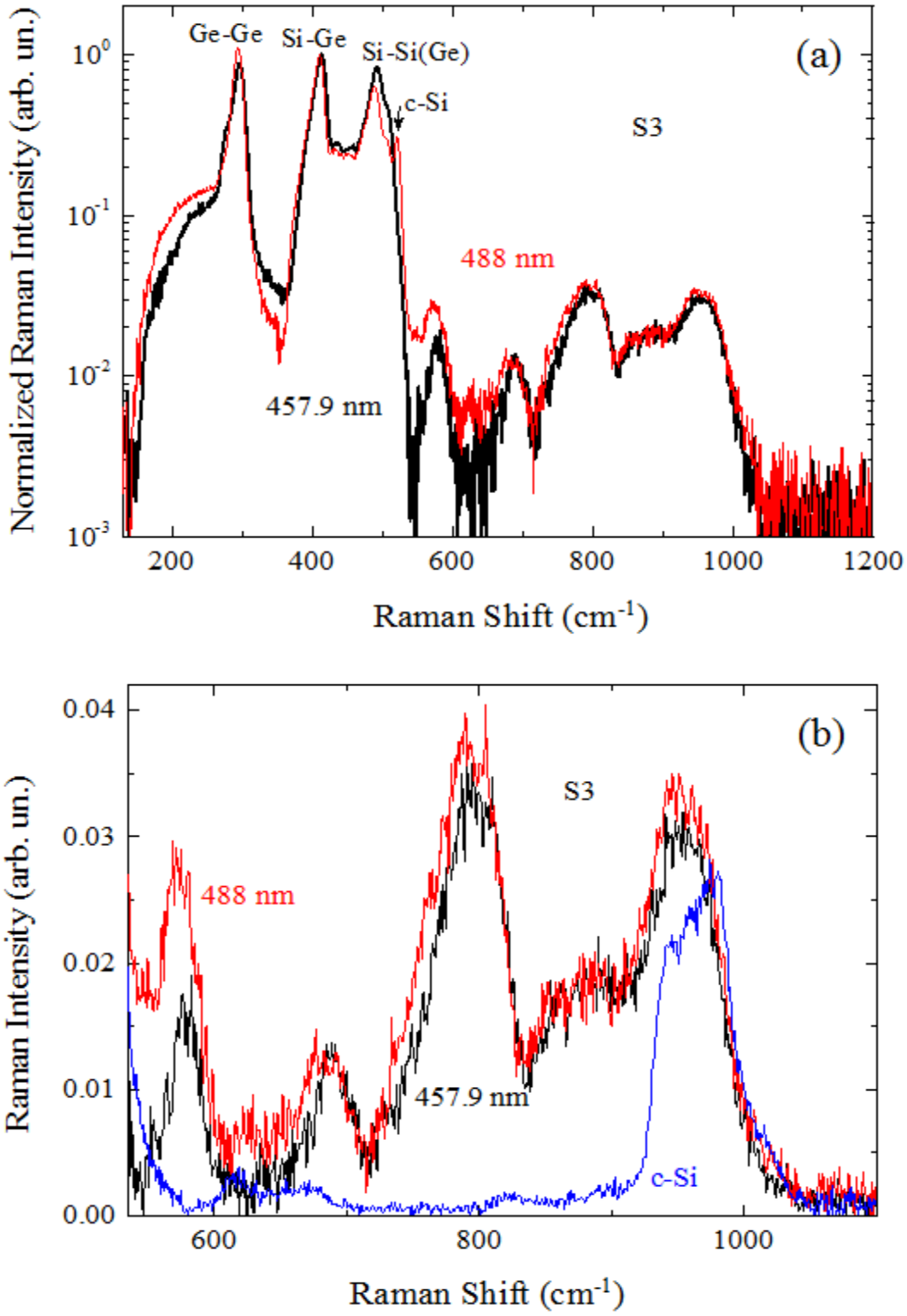

Figure 4.5 Comparison of normalized Raman spectra in sample S3 measured at the indicated excitation wavelengths: (a) full range spectra showing first and second order Raman peaks and (b) Raman spectra on a linear intensity scale comparing major second order peaks with respect to c-Si (the excitation wavelength is 457.9 nm).

In c-Si, the two-transverse optical (2TO) phonon overtone scattering from the Brillouin zone critical points at W and L are observed at 940 and 975 cm^{-1}, respectively [115]. The 2TO Raman signal is usually curve fitted using three peaks: the major Raman peak associated with scattering from 2TO(L) phonons, the 2TO(W) Raman peak, and a weak shoulder associated with the 2TO(Γ) phonon. In S3, the 2TO(Γ) peak completely disappears, and the relative heights of the 2TO(L) and 2TO(W) peaks are reversed, mostly due to the fact that there is practically no Raman signal at 520 cm^{-1} and the contribution of the first-order Si-Si(Ge) peak at ~ 488 cm^{-1} is stronger. Interestingly, the 2TO(L) Raman peak of Ge-Ge (Si) at ~ 575 cm^{-1} and a weak shoulder of the 2TO(Γ) peak at ~ 585 cm^{-1} are stronger and slightly shifted to lower wavenumbers under 488 nm laser excitation compared to that under 457.9 nm excitation, and that is most likely due to the resonant effect in Raman scattering [116, 117].

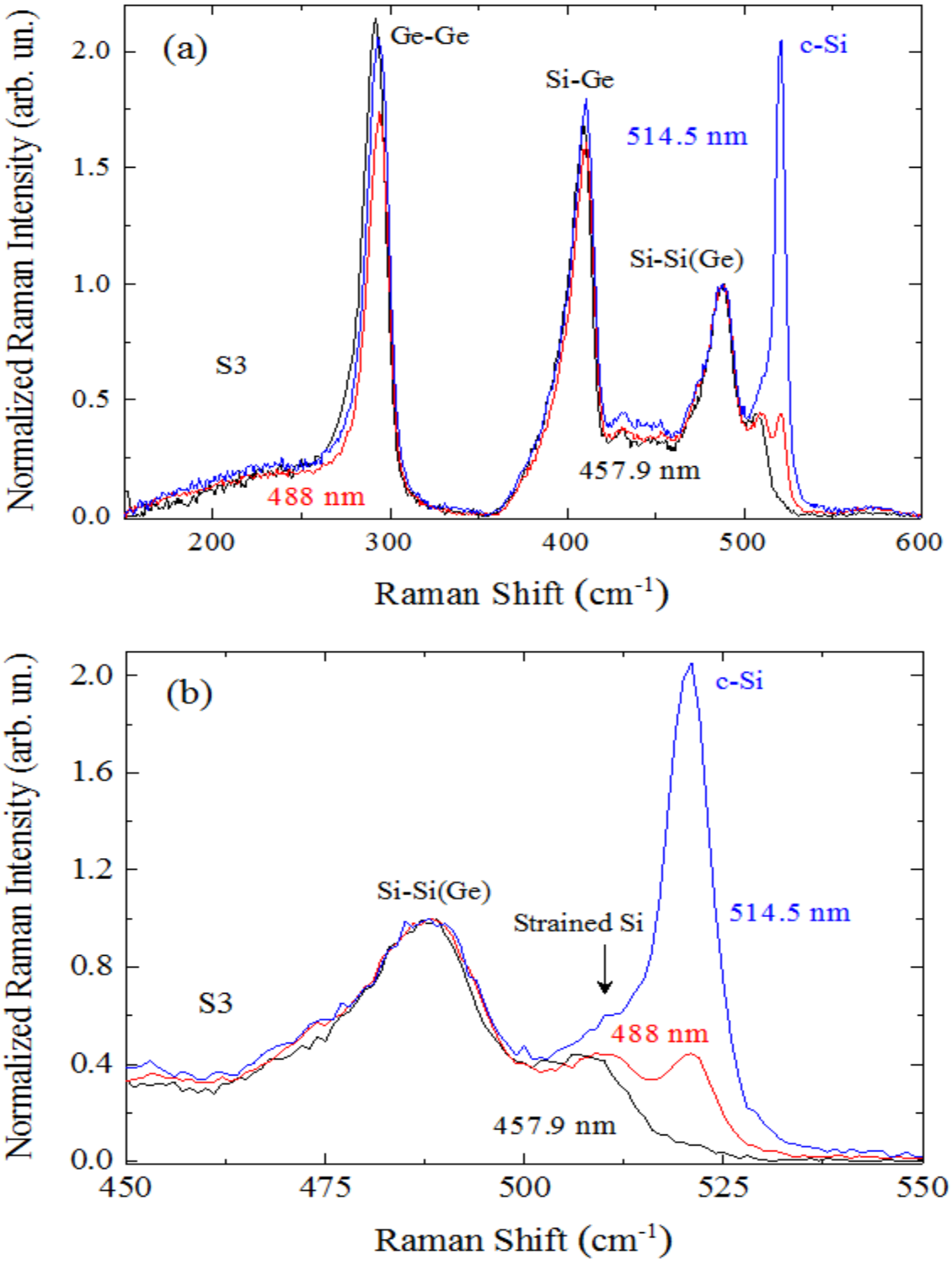

Figure 4.6 The Raman spectra at room temperature in sample S3 measured at the indicated excitation wavelengths of visible light showing (a) the relative intensities of the major Si-Si, Si-Ge, and Ge-Ge Raman peaks and (b) three Si-Si vibration modes within the range of 480 – 530 cm^{-1}.

The intensity of non-resonant Raman scattering is proportional to the scattering volume associated with the light penetration depth from the sample surface, and the light penetration depth in our samples strongly depends on excitation wavelength. In S3, Raman spectra using various excitation wavelengths are measured and significant changes in the relative intensities of Raman peaks associated with the major Si-Si, Si-Ge, and Ge-Ge vibration modes are found [Figure 4.6 (a)]. Figure 4.6 (b) shows a closer look at the three Si-Si vibration modes within the range of 480-530 cm^{-1} for three different (indicated) laser excitation wavelengths also measured in S3. The Raman peak observed at ~510 cm^{-1} between the Si-Si phonon band of the SiGe alloy layer and the c-Si substrate peak is attributed to strained Si within the Si spacer layers [50, 99]. Using curve fitting, it is found that the peak frequency of strained Si shifts considerably from 507.5 to 515 cm^{-1} when the laser excitation wavelength increases from 457.9 to 514.5 nm. This result confirms the existence of a vertical strain gradient within the sample layers and points out that, in S3, built-in tensile strain in the top Si layers separating SiGe clusters is greater compared to that in Si layers at the bottom of the Si/SiGe cluster multilayer structure. Similar results are obtained in S2, where with an increase of excitation wavelength from 457.9 to 514.5 nm the strained Si Raman peak shifts from 506 to 517 cm^{-1}. To the contrary, in S1 the strained Si Raman peak at ~ 505 cm^{-1} does not shift under varying the excitation wavelength (not shown).

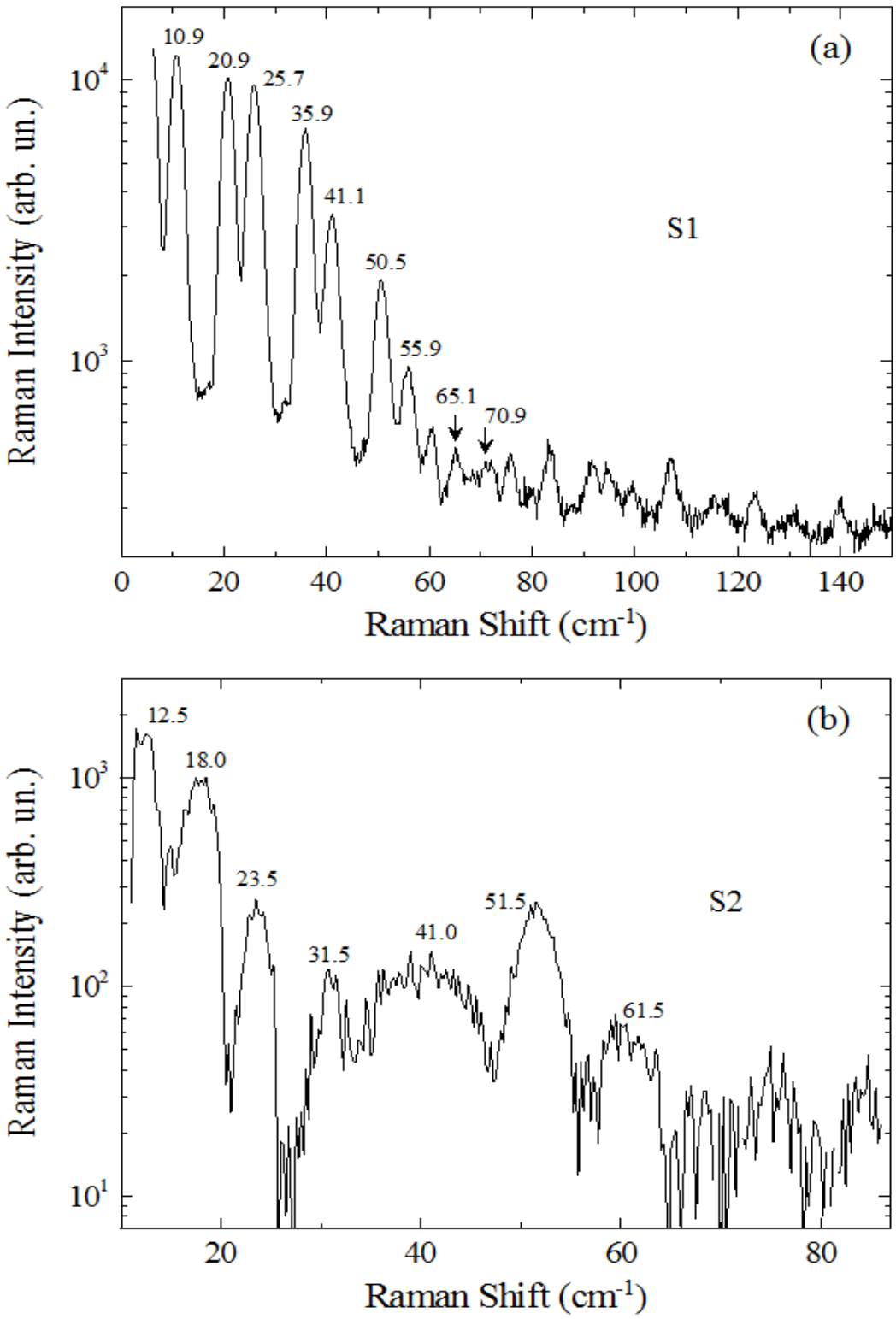

Figure 4.7 The low-frequency Raman spectra of folded longitudinal-acoustic phonons measured using 457.9 nm in samples (a) S1 and (b) S2. Note the vertical logarithmic scale.

Figure 4.7 compares Raman spectra of S1 and S2 in the low frequency spectral region, where Raman scattering is associated with Brillioun zone folding of longitudinal acoustic (FLA) phonons due to the new periodicity in the growth direction of the $Si/Si_{1-x}Ge_x$ multilayer NS [114]. A simplified FLA phonon dispersion, including changes due to varying thicknesses and average composition will be discussed later.

The baseline corrected Stokes and anti-Stokes Raman spectra in samples S1-S3 are presented in Figures 4.8 (a) - 4.10 (a), respectively. Stokes and anti-Stokes Raman spectra represent processes involving phonon emission and phonon absorption, and the intensity ratio of the Stokes and anti-Stokes non-resonant Raman peaks (I_S/I_A) is proportional to the phonon population. Thus, sample temperature can be calculated using Boltzmann statistics:

$$\frac{I_S}{I_A} = e^{\frac{\hbar\omega_p}{k_B T}}, \tag{4.1}$$

where $\hbar\omega_p$ is the phonon energy, k_B is the Boltzmann constant, and T is the absolute temperature.

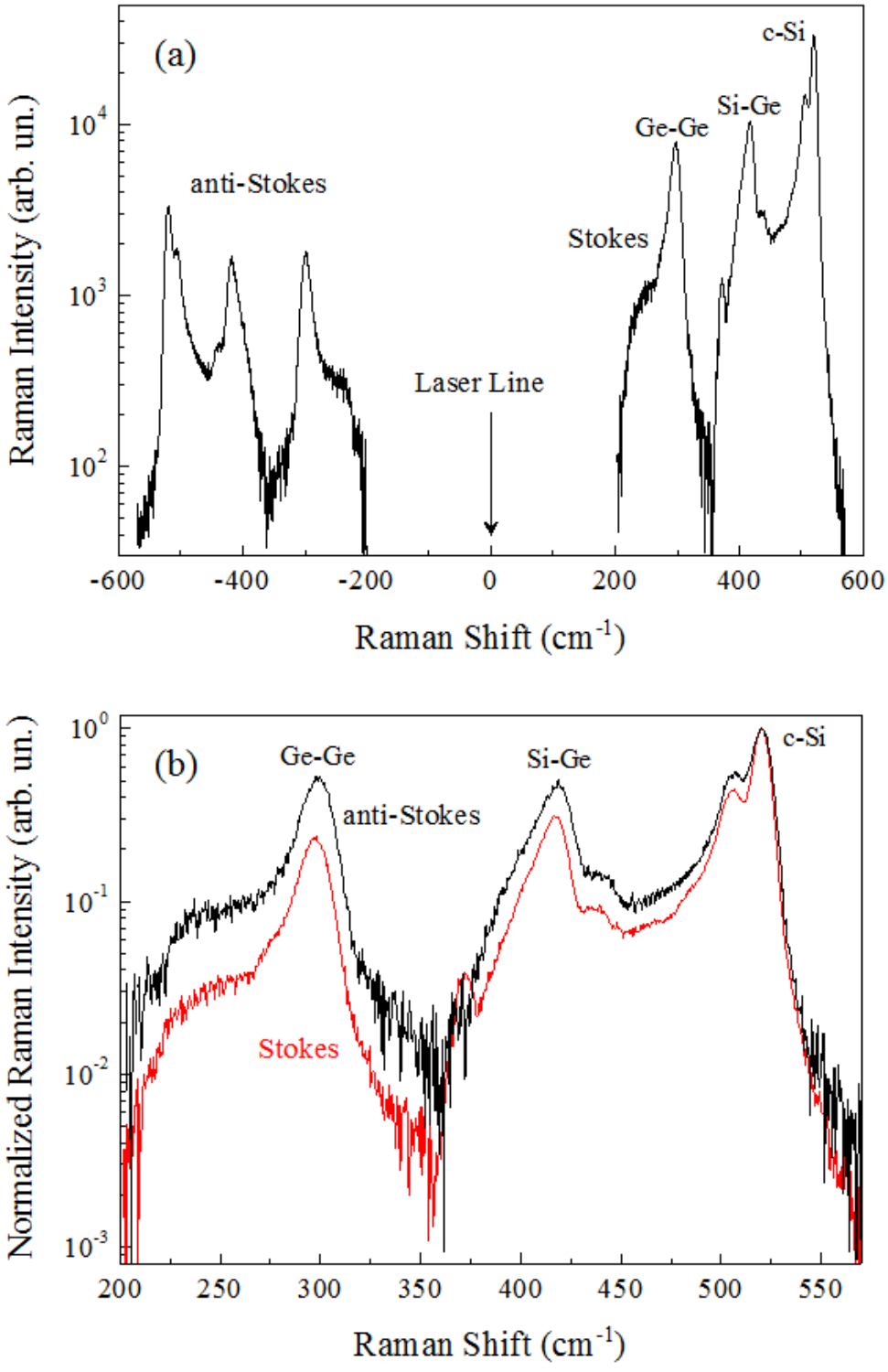

Figure 4.8 (a) The Stokes and anti-Stokes components of the Raman spectrum of sample S1 excited at a wavelength of 457.9 nm and (b) normalized Stokes/anti-Stokes Raman peaks with respect to the Si-Si peak at 520 cm^{-1}.

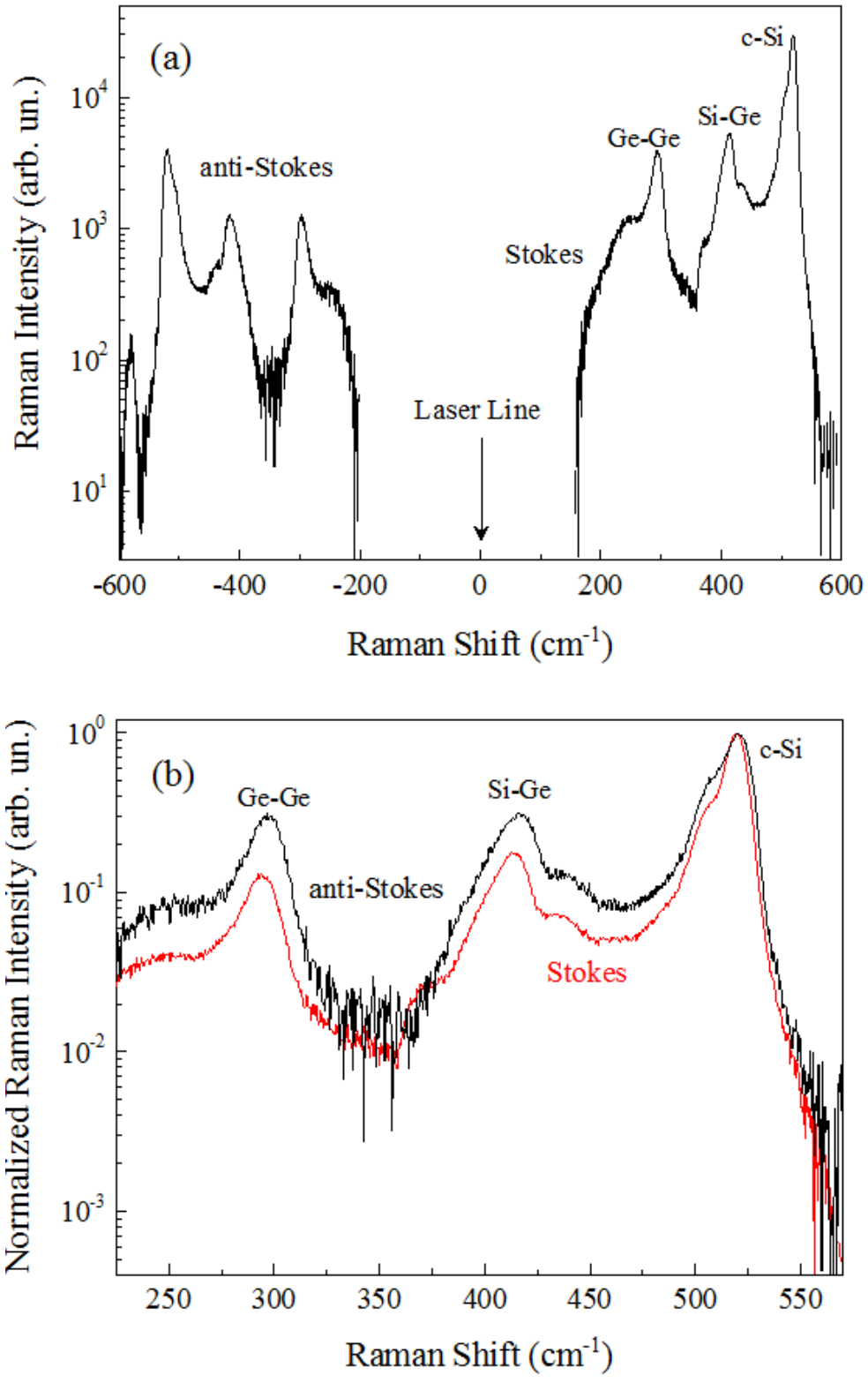

Figure 4.9 (a) The Stokes and anti-Stokes components of the Raman spectrum of sample S2 excited at a wavelength of 457.9 nm and (b) normalized Stokes/anti-Stokes Raman peaks with respect to the Si-Si peak at 520 cm^{-1}.

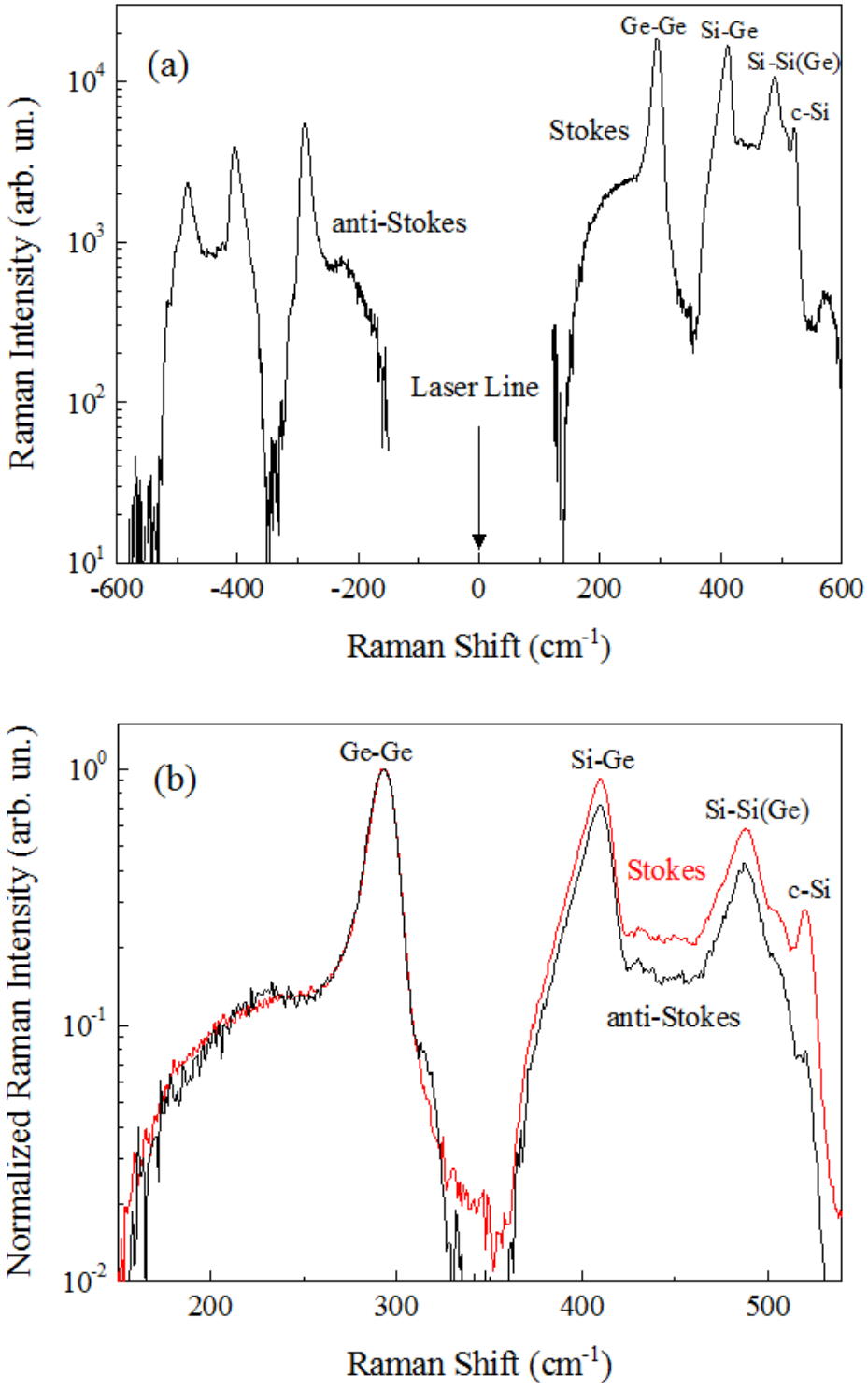

Figure 4.10 (a) The Stokes and anti-Stokes components of the Raman spectrum of sample S3 using an excitation wavelength of 488 nm and (b) normalized Stokes/anti-Stokes Raman peaks with respect to the Si-Ge peak at 293 cm^{-1}.

Figures 4.8 (b) – 4.10 (b) show normalized and superimposed Stokes and anti-Stokes Raman spectra (note that the horizontal axes are absolute values of the Raman shift). It is found that I_S/I_A is different for different vibration modes (Si-Si at 520 cm^{-1}, Si-Ge at ~ 400 cm^{-1}, and Ge-Ge at ~300 cm^{-1}). Assuming that non-resonant Raman scattering is measured, this difference could only be due to the fact that the temperature is different in different parts of the samples. Since Raman scattering is measured using an intense (1-10 kW/cm^2), strongly absorbed laser radiation, and the thermal conductivity in SiGe NSs is ~10 times lower compared to that in c-Si [129], it is assumed that temperature of the SiGe NS is higher compared to the c-Si substrate temperature. The calculated temperatures associated with different vibration modes (and different parts of the samples) are shown in Table 4.1. The explanation and details of the heat dissipation process during Raman scattering measurements in our samples are given below.

Table 4.1 Calculated Temperatures in Different Parts of the Samples S1-S3 Based on Raman Scattering Thermometry

Sample No.	T_{Si-Si} (K)	T_{Si-Ge} (K)	T_{Ge-Ge} (K)	T_{Si-Sub} (K)	ΔT (K)	Thermal Conductivity (W/m K)
S1	~ 350	~ 340	~ 315	~ 325	~ 25	~ 12
S2	~ 425	~ 423	~ 395	~ 375	~ 50	~ 6
S3	~ 411	~ 407	~ 351	~ 304	~ 100	~ 4

4.1.2 Discussion

4.1.2.1 Strain and Chemical Composition in Si/SiGe NSs. In our experimental results, a correlation between Si-Si, Si-Ge and Ge-Ge Raman peak positions, peak intensities, Ge content (x) and strain (ε) is observed. Our analysis has been started with estimating x using two different methods: the Raman peak integrated intensity and the peak position in wavenumbers. In $Si/Si_{1-x}Ge_x$ NSs, the relative number of bonds comprising the Si-Si, Si-Ge, and Ge-Ge phonon modes are estimated as $(1-x)^2$, $2x(1-x)$, and x^2, respectively. The ratio of the integrated peak intensities related to the relative number of bonds of the corresponding phonon modes are as follows:

$$I_{GeGe}/I_{SiGe} = Bx/2(1-x), \tag{4.2}$$

$$I_{SiSi}/I_{SiGe} = A(1-x)/2x, \tag{4.3}$$

where coefficients A and B are related to the frequencies of the optical modes in the SiGe alloy. It is found experimentally that $B = 3.2$ and $A = 1.85$ for 457.9 nm excitation [97]. The intensity method for determining the value of x is independent of strain in the alloy layer and depends on the integrated intensity of the phonon bands. Thus, proper baseline correction is required to estimate the intensity with accuracy. In the Raman peak position (wavenumber) method, a set of equations is used where the Raman peak position of the three major vibrational modes in $Si/Si_{1-x}Ge_x$ NSs is described as a function of x and ε. The major phonon bands have been curve fitted mostly using a Voigt profile to estimate the peak positions accurately. The frequency of phonon band can be expressed as:

$$\omega = \omega_0 + b\varepsilon, \tag{4.4}$$

where ω_0 is the x dependent phonon frequency of the unstrained alloy and b is the strain-shift coefficient. In the case of a strained $Si_{1-x}Ge_x$ ($0 < x < 0.5$) layer, the wavenumbers of the three different phonon modes are [99, 101]:

$$\omega_{SiSi} = 520.2 - 70.5x - 830\varepsilon, \tag{4.5}$$

$$\omega_{SiGe} = 400.5 + 16.3x - 575\varepsilon, \tag{4.6}$$

$$\omega_{GeGe} = 282.5 + 16x - 384\varepsilon. \tag{4.7}$$

The average value of x and ε in the alloy layer can be determined by solving, for example, equations 4.5 and 4.6, as follows:

$$x = \frac{(\omega_{SiGe} - 400.5) - 0.6928 \times (\omega_{SiSi} - 520.2)}{65.14}, \tag{4.8}$$

$$\varepsilon = \frac{(400.5 - \omega_{SiGe}) + 0.23 \times (520.2 - \omega_{SiSi})}{766.9}. \tag{4.9}$$

The calculated values of x and ε using the Raman data are summarized in Table 4.2, and they are compared with the EDX spectroscopy data. A reasonably good correlation is found between Raman and EDX data, while the observed increase of local sample temperature under intense laser radiation (1-10 kW/cm^2) during Raman measurements and resonant Raman scattering might be responsible for the observed discrepancies. Also

according to our results, strain in S2 and S3 has a considerable gradient along the growth direction, and this also needs to be taken into account.

Table 4.2 Estimated Values of Ge Content and Strain for the $Si_{1-x}Ge_x$ Layers of Samples S1-S3 using Raman Scattering Data Collected under 457.9 nm Excitation (The Corresponding EDX Values of x are Given for Comparison Purposes)

Sample	Ge content, *x*				Compressive strain ε (%) [Equation (4.9)]
	Equation (4.2)	Equation (4.3)	Equation (4.8)	EDX data	
S1	0.32±0.01	0.41±0.01	0.42±0.02	0.35	1.85±0.1
S2	0.33±0.02	0.33±0.01	0.36±0.02	0.4	1.5±0.25
S3	0.4±0.02	0.55±0.02	0.49±0.01	0.5	0.75±0.05

4.1.2.2 Relative Raman Signal Intensity in Si/SiGe NSs. As it is already pointed out, the intensity of non-resonant Raman scattering depends mainly on the scattering volume (i.e., sample thicknesses and light penetration depth, and the later depends on the excitation wavelength). In S1 and S2 under 457.9 nm laser wavelength excitation, the light penetration depth is more than 0.5 μm [130] and the entire sample thicknesses are less than 150 nm. Assuming the same Raman cross-section and only small changes in the Si absorption coefficient (α) due to strain, the anticipated ratio between the intensities of the Raman signals associated with the c-Si substrate at 520 cm^{-1} and strained Si layers at 505-506 cm^{-1} is ~ 4:1, which is close to our experimental data [Figures 4.3 (a) and 4.4].

In S3, the Raman intensities of the Si-Si, Si-Ge, and Ge-Ge phonon bands using 514.5, 488, and 457.9 nm light excitation wavelengths are examined. The Raman peaks at ~ 520, 488, 411, and 292 cm^{-1} are attributed to the c-Si substrate, Si-Si (Ge), Si-Ge, and Ge-Ge phonon modes in the SiGe alloy layer, respectively [Figure 4.6 (a)]. The Si-Si phonon band of the c-Si substrate (~ 520 cm^{-1}) and top epitaxial SiGe alloy layer (~ 488 cm^{-1}) contribute together to the observed Raman spectra in the vicinity of 500 cm^{-1}. The relative intensities of Raman scattering from the c-Si substrate and SiGe alloy layer vary with the excitation wavelength, as illustrated in Figure 4.6 (a). The relative intensities of Raman scattering associated with the c-Si substrate and Si-Si, Si-Ge, and Ge-Ge modes in the SiGe alloy layers have been calculated according to the following expressions, where the scattering-volume relation is taken into account [131]:

$$I_{alloy} \propto \int_0^t e^{-2\alpha_{alloy}x}dx$$

$$= \frac{1}{2\alpha_{alloy}}(1 - e^{-2\alpha_{alloy}t}), \tag{4.10}$$

$$I_{substrate} \propto e^{-2\alpha_{alloy}t}\int_t^\infty e^{-2\alpha_{substrate}x}dx$$

$$= \frac{1}{2\alpha_{substrate}}e^{-2\alpha_{alloy}t}e^{-2\alpha_{substrate}t}, \tag{4.11}$$

where *t* is the thickness of the alloy layer. Our calculations based on the scattering-volume relation are in a good agreement with our experimental results, as shown in Figure 4.11.

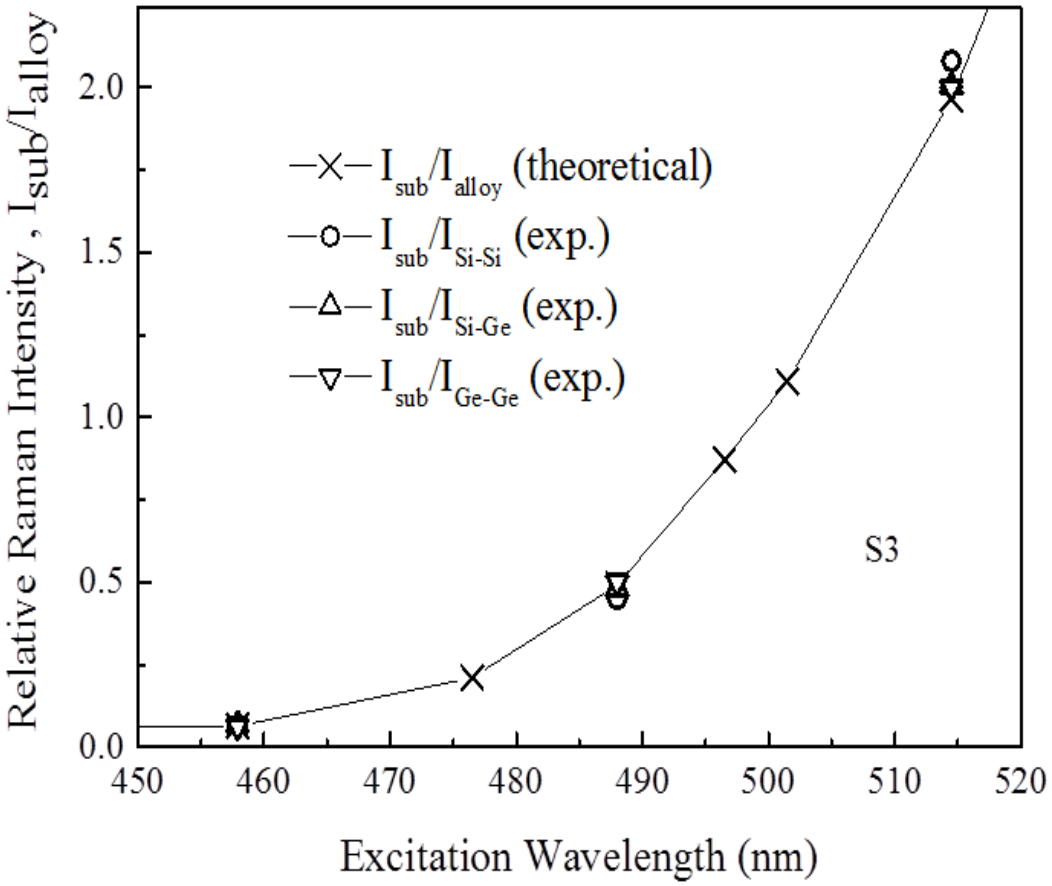

Figure 4.11 Experimental results of relative Raman intensities (the c-Si substrate and Si-Si, Si-Ge, and Ge-Ge vibration modes in a 50 nm thick, partially relaxed $Si_{0.5}Ge_{0.5}$ alloy layer) as a function of excitation wavelength compared with the theoretical calculations using the scattering-volume relation.

4.1.2.3 Folded Longitudinal Acoustic Phonons in Periodic and Quasi-Periodic $Si/Si_{1-x}Ge_x$ NSs. Figure 4.12 (a) shows a simplified version of the S1 phonon dispersion curve calculated using Rytov's theory [113]. The sound velocity in a superlattice is:

$$V_{SL} = d\left[\frac{d_1^2}{V_1^2} + \frac{d_2^2}{V_2^2} + \left[R + \frac{1}{R}\right]\frac{d_1 d_2}{V_1 V_2}\right]^{-1/2}, \quad (4.12)$$

where $R = \frac{\rho_2 V_2}{\rho_1 V_1}$, and the superlattice periodicity, $d = d_1 + d_2$. d_1 and d_2, V_1 and V_2, ρ_1 and ρ_2 are the thicknesses, sound velocities, and densities of the Si spacer and $Si_{1-x}Ge_x$ alloy layers, respectively. The frequency dispersion of the FLA phonons is calculated from

$$\omega = \left(\frac{2m\pi}{d} \pm q\right) V_{SL}, \quad (4.13)$$

where m = 0, 1, 2,…. is the folding index and q is the wave vector of the superlattice. The parameters used in the calculation are listed in Table 4.3. The density ρ_2 and the sound velocity V_2 in the $Si_{1-x}Ge_x$ layer are calculated using linear interpolation between these values for Si and Ge [114].

Table 4.3 Parameters of Si and Ge used in the Calculation of Rytov Model

	Si	Ge
Sound velocity (cm/s)	8.44×10^5	4.9×10^5
Density (g/cm^3)	2.33	5.36

Source: http://www.ioffe.ru/SVA/NSM/Semicond/index.html [24].

For S1, a planar superlattice, the phonon dispersion curves shown in Figure 4.12 (a) are readily calculated with equations 4.12 and 4.13. For S2, the thicknesses of the Si spacer and $Si_{1-x}Ge_x$ alloy layers vary at the cluster peak and valley, as shown in Figure 3.1 (b). The phonon dispersion curves have been calculated considering that the reduced wave vector is different at the cluster valley and at the cluster peak. This structural division results in two sets of phonon dispersion curves, as shown in Figure 4.12 (b). Also, the cluster composition is found to be strongly non-uniform due to interdiffusion during growth [132]. Therefore, the low-frequency FLA peaks become broader and merge together due to the diffuse interface and variation across the layers of the periodicity and thicknesses of the SiGe cluster layers. This simple model provides a good semi-quantitative explanation of the experimental results obtained [Figure 4.12 (b)].

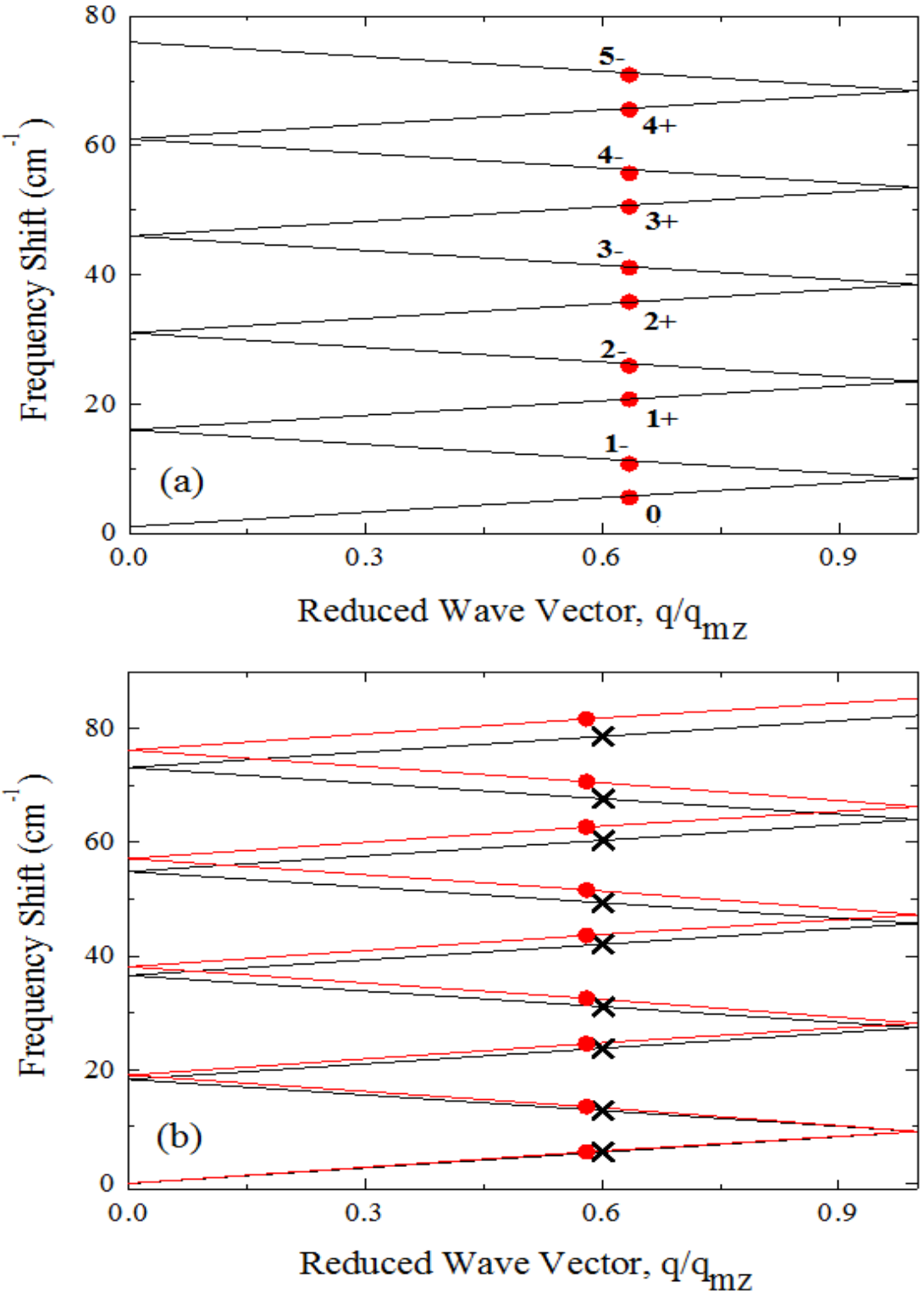

Figure 4.12 The folded longitudinal-acoustic phonon dispersion curve calculated according to Rytov's theory of samples (a) S1 and (S2). The FLA peak positions at the cluster peak and valley of sample S2 are marked with the crosses and filled circles, respectively.

4.1.2.4 Thermal Conductivity and Heat Dissipation in $Si/Si_{1-x}Ge_x$ NSs. During Raman scattering measurements in $Si/Si_{1-x}Ge_x$ NSs exposed to intense laser light, the thermal conductivity (κ) can be evaluated via the temperature gradient (the observed temperature gradient between different parts of the sample is calculated using equation 4.1). The thermal conductivity is calculated using the proposed model (see Figure 3.5) and equation 3.1, and the values obtained are ~12, 6, and 4 W/m-K in samples S1-S3, respectively.

The reason for the lower thermal conductivity found in S2/S3 compared to S1 can be understood by analyzing a comparative volume fraction of SiGe (a lower thermal conductivity material) versus Si (a higher thermal conductivity material) and quality of the Si/SiGe heterointerfaces. The average volume fraction of SiGe has been calculated using the TEM images and EDX data (Figures 3.1 (a), (b), (c), and 3.2 (a), (b)). The volume fraction of SiGe in S1 is estimated to be ~ 25% while it is ~ 40-45% at the peak of the SiGe clusters and ~ 20-25% at the valley between two SiGe clusters in sample S2. Thus, the lower SiGe/Si ratio in S1 compared to that in S2 is, most likely, responsible for the higher thermal conductivity found in S1. Similarly, in S3 a slightly higher volume fraction of SiGe and a slightly lower thermal conductivity compared to that in S2 are found. In addition, inelastic scattering of phonons in Si/SiGe NSs with a diffuse interface also contributes to the reduction in thermal conductivity [66]. Our results on the thermal conductivity are in a good agreement with the results obtained by different methods [15, 73, 133].

Interestingly, the experimental results in Table 4.1 indicate that the local temperature calculated according to Boltzmann statistics under a non-resonant condition

of the Ge-Ge phonon mode is consistently lower than that found for the Si-Ge and Si-Si modes. This discrepancy can be explained assuming that for the laser excitation wavelengths used and the alloy composition (*x*). Raman scattering associated with Ge-Ge phonon mode might have a resonant component, as also pointed out in the references [116, 117, 134, 135].

4.2 PL Measurements in Si/SiGe NSs

Low temperature (17 K) PL measurements were performed in a high quality $Si_{1-x}Ge_x$ NL with x ~ 8% grown on locally strained Si layers sandwiched between $Si_{1-x}Ge_x$ clusters with $x \leq 40\%$ using CW and pulsed laser excitation. The PL properties of SiGe cluster and SiGe NL have been investigated. For CW laser excitation, an Ar+ laser (514 nm, 488 nm, 457.9 nm, and a multi-line), a HeCd laser (325 nm), and high-power light-emitting diode with a peak near 365 nm are used. PL dynamics using a Q-switched Nd:YAG pulse laser of 355 nm excitation wavelength were studied. The excitation energy density was varied from 1.5 to 50 mJ/cm^2.

Two different measurement techniques were used to investigate the significant peaks in multilayers Si/SiGe NSs under pulsed laser excitation; the measured time-integrated PL spectrum using a lock-in amplifier shows the peak at 0.8 eV associated with SiGe cluster and the peak-intensity PL signal reveals the peak at 0.92 eV associate with SiGe NL. Longer PL rise time in SiGe cluster and non-exponential PL decays both in SiGe cluster and SiGe QW have been found. The spatial separation of electrons and holes, where electrons are localized in Si and holes are located in the SiGe cluster core area, explains the experimentally found long-lived PL in Si/SiGe clusters [9, 136-138].

The recombination rate has been measured and a model has been proposed to explain the fast and slow recombination rates found in tailored multilayer Si/SiGe NSs.

4.2.1 Results

Figure 4.13 shows the normalized PL spectra of MBE grown multi-layers Si/SiGe NSs measured under three different excitation wavelengths (514, 365, and 355 nm).

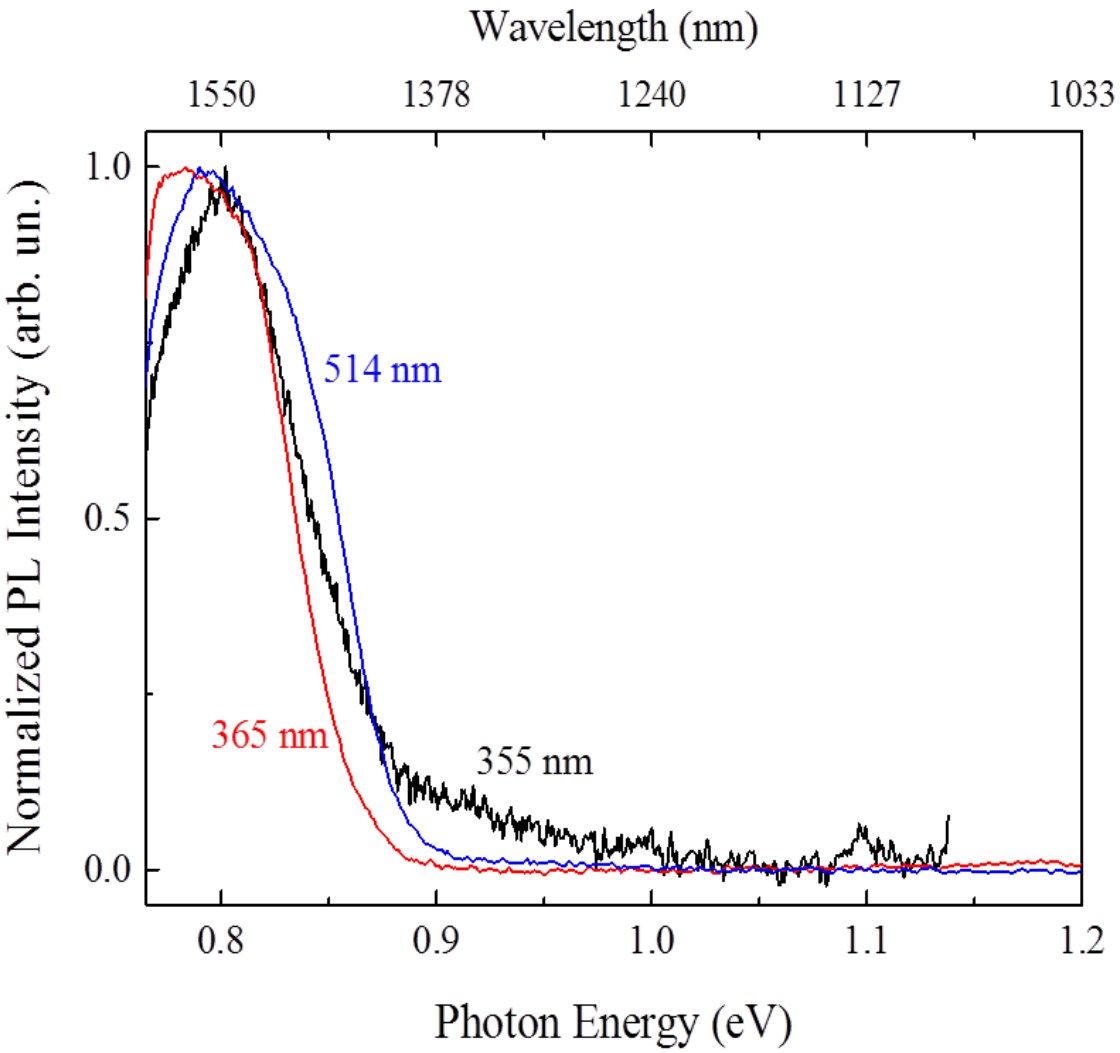

Figure 4.13 Normalized PL spectra at low temperature (T = 17 K) measured using different excitation wavelengths.

In Figure 4.13, the major and broad PL peak at 1550 nm (0.8 eV) attributed to the SiGe cluster, a broad but rather weak peak PL feature at 1350 nm (0.92 eV) associated with SiGe NL are observed. The broad feature at 0.8 eV in the PL spectra is due to the non-uniform size, shape, and composition of individual clusters [122]. A weak c-Si PL peak at 1130 nm (1.097 eV) is also found under 355 nm pulsed Nd:YAG laser.

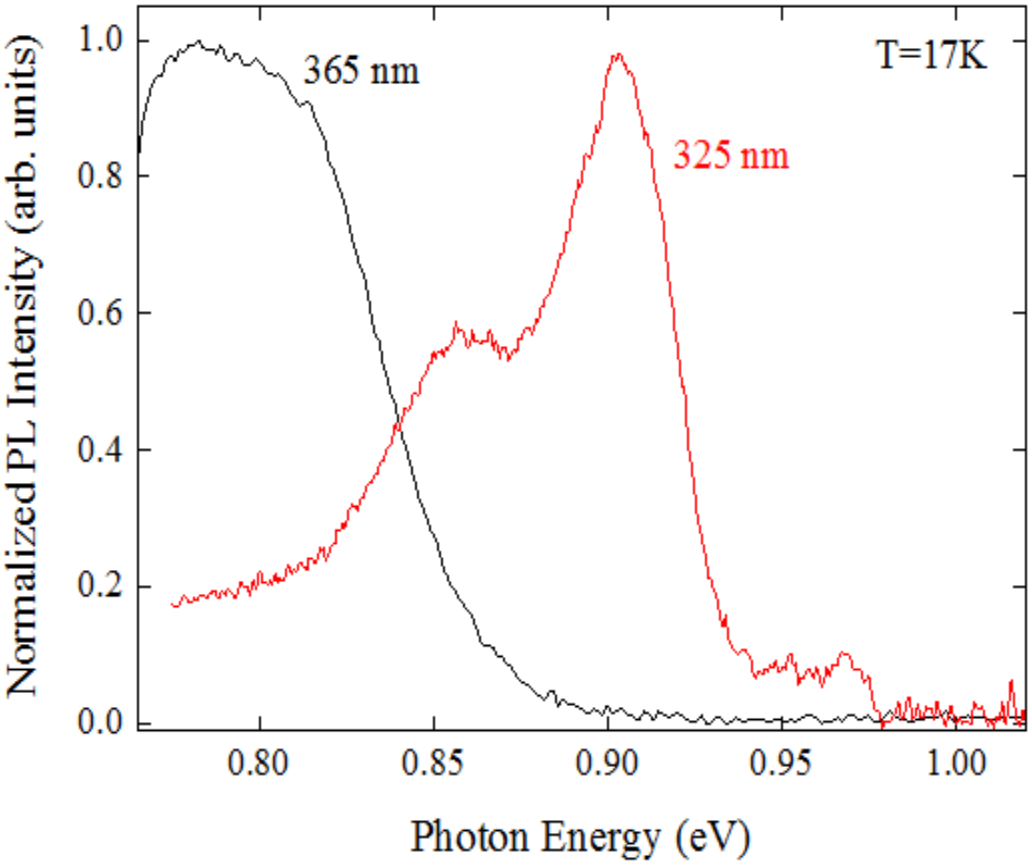

Figure 4.14 Low temperature PL spectra recorded under CW excitation with the indicated excitation wavelengths.

Figure 4.14 compares the PL spectra obtained with two different excitation wavelengths and with approximately the same intensities. The PL spectrum under steady-

state 365 nm excitation is peaked around 0.8 eV, while the PL obtained under CW 325 nm excitation is peaked near 0.9 eV. Under these excitation conditions no significant PL signal from c-Si at ~ 1.1 eV was found.

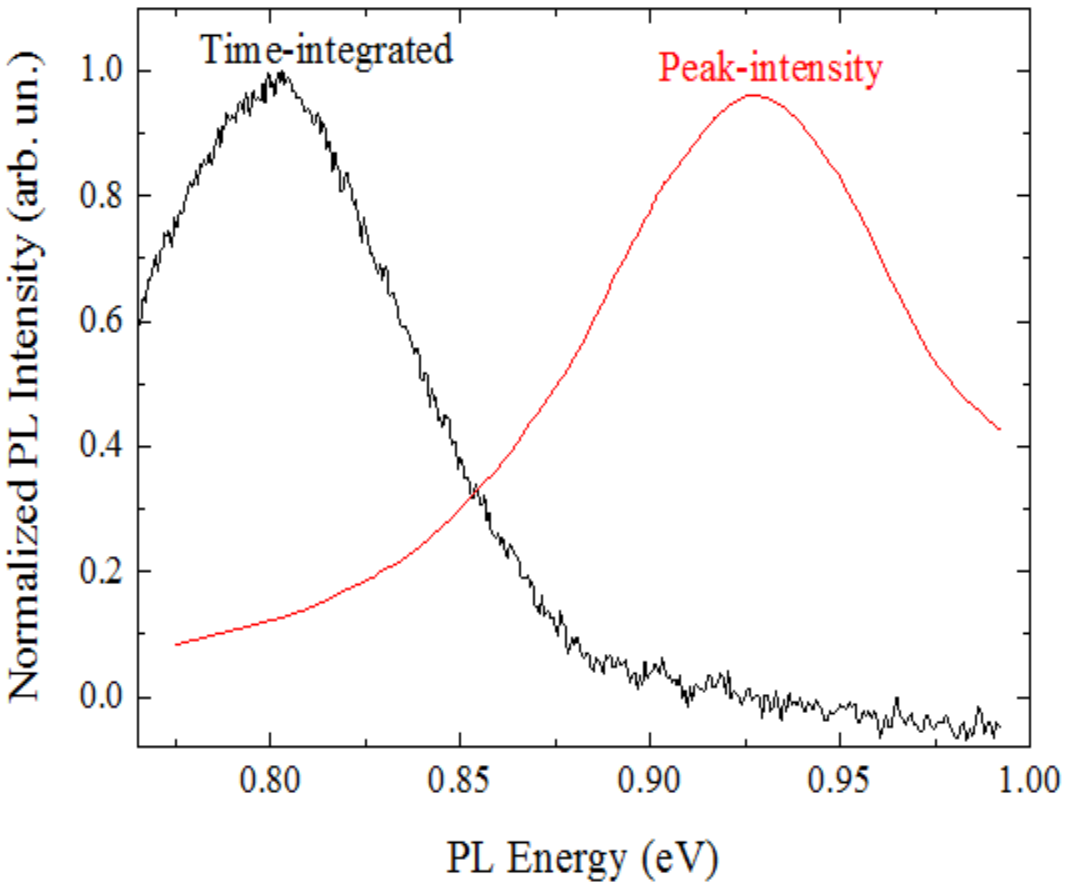

Figure 4.15 Low temperature (T=17 K) PL spectra recorded under pulsed 355-nm excitation using the time-integrated and peak-intensity methods.

Figure 4.15 shows the PL spectra measured under pulsed 355 nm wavelength photo-excitation using different measurement techniques. The PL time-integrated measurements were performed using a lock-in amplifier synchronized with the pulse of the Nd:YAG laser; in this measurement, the accumulation time is in the order of

10^{-3} - 10^{-2} s. The PL peak intensity was measured using a digital oscilloscope. These two different techniques produced quite different results: the time-integrated PL spectrum shows a peak near 0.8 eV while the PL peak intensity spectrum has a maximum at ~ 0.92 eV. Such a difference in the PL spectra can arise from a significant difference in lifetimes of the respective PL components, which is expected to be much shorter for the PL peaked at 0.92 eV compared to the PL peaked at 0.8 eV [138].

Figure 4.16 shows the normalized PL dynamics of SiGe clusters (at 0.8 eV) and SiGe NL (at 0.92 eV) measured under different excitation energies (1.5 to 50 mJ/cm^2) at 17 K using the Q-switched Nd:YAG pulsed laser with excitation wavelength λ = 355 nm, pulse duration τ = 6 ns, and repetition rate ν = 9 Hz. The PL dynamics comprises of fast and slow decays; fast PL decays are single-exponential under applied excitation energy densities, and the slow PL decays exhibit non-exponential behavior for both the PL bands (SiGe cluster and SiGe NL). It is found that the initial PL decays in SiGe cluster become faster with the increasing excitation energy density (Figure 4.16 (a)).

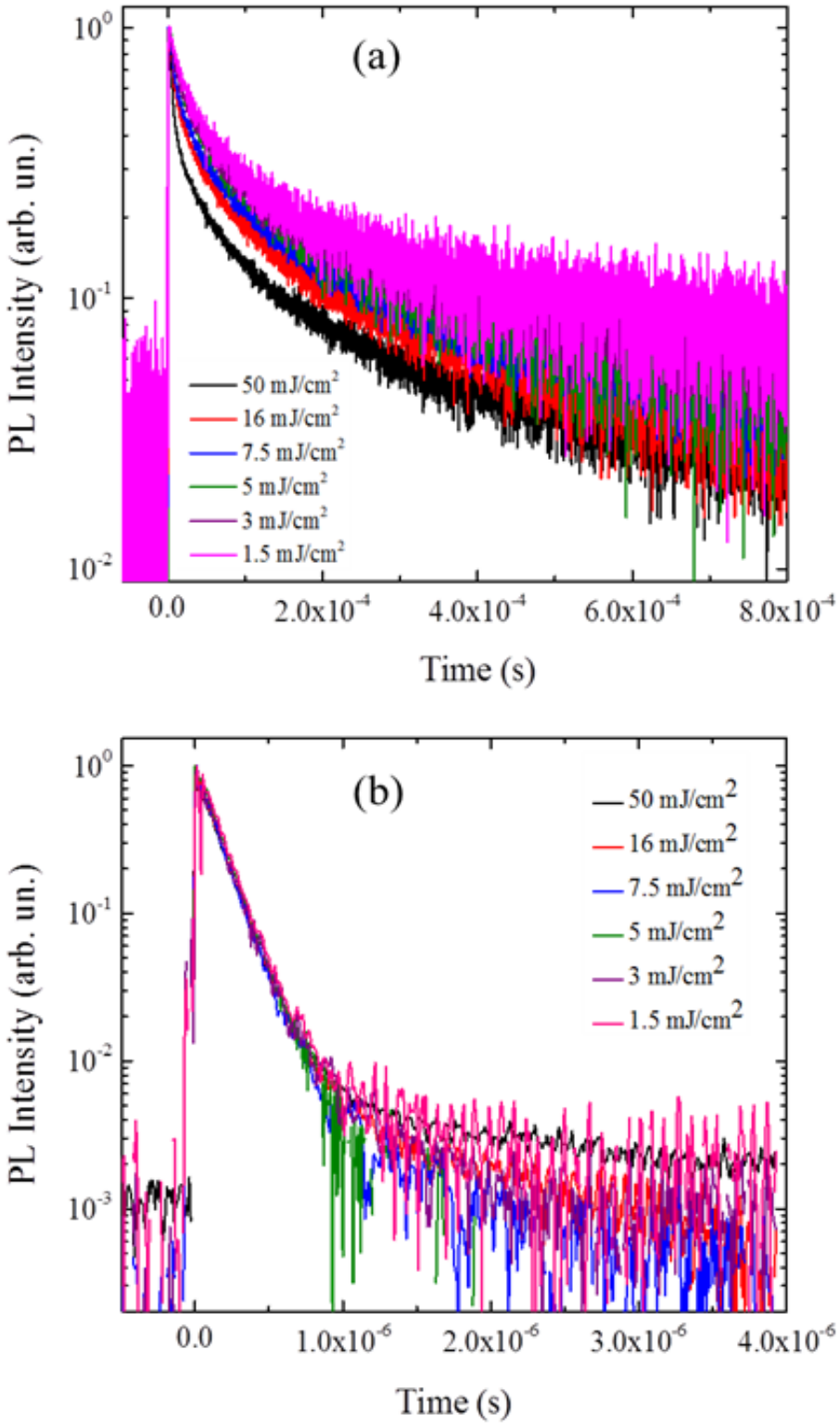

Figure 4.16 Low temperature (T = 17 K) PL dynamics under excitation energy densities (1.5 - 50 mJ/cm^2) measured at (a) 0.8 eV and (b) 0.92 eV.

Figure 4.17 compares PL intensities as a function of pulsed laser energy density. It is found that the intensity of the PL peaked at 0.92 eV is linear versus excitation energy density with no saturation evident until ~50 mJ/cm^2, while the PL peaked at 0.8 eV depends on excitation energy density as the square root.

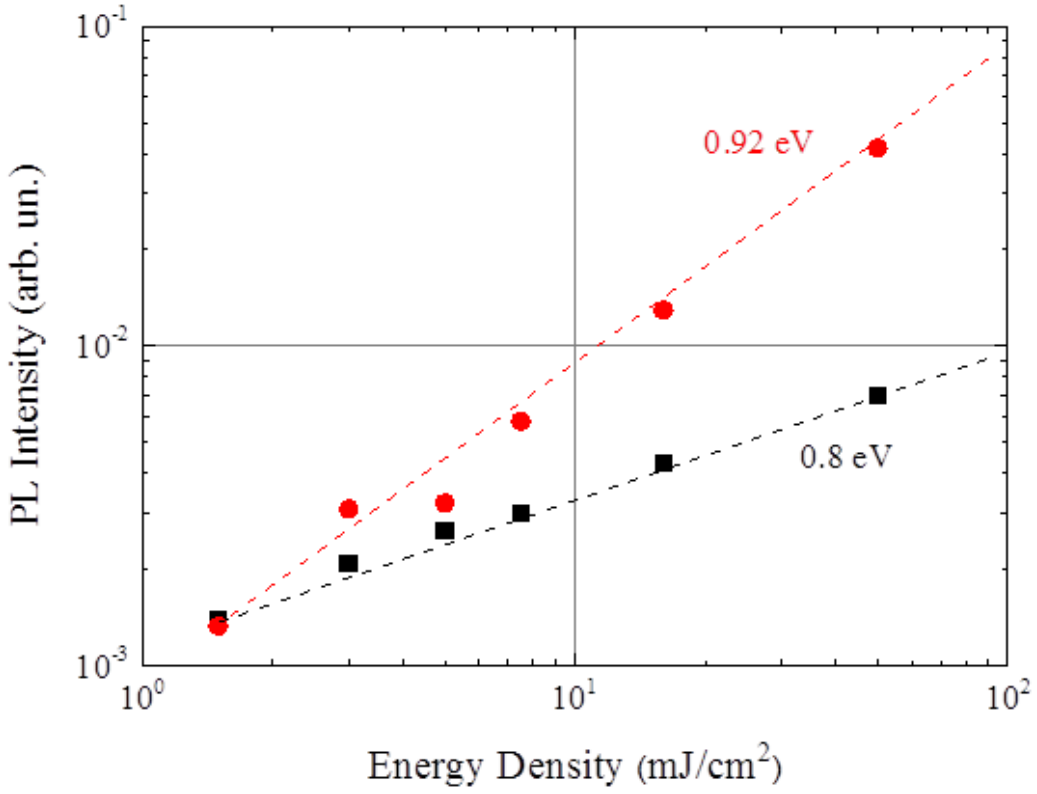

Figure 4.17 Low temperature (T = 17 K) PL intensity versus excitation energy density for two (indicated) photon detection energies.

The PL signal peaked at 0.8 eV (SiGe cluster PL) presents delayed PL with a long rise time (~3 μs) found at low excitation intensity and low temperature, as shown in Figure 4.18. The extracted rise time as a function of temperature and energy density in SiGe clusters is shown in Figure 4.19

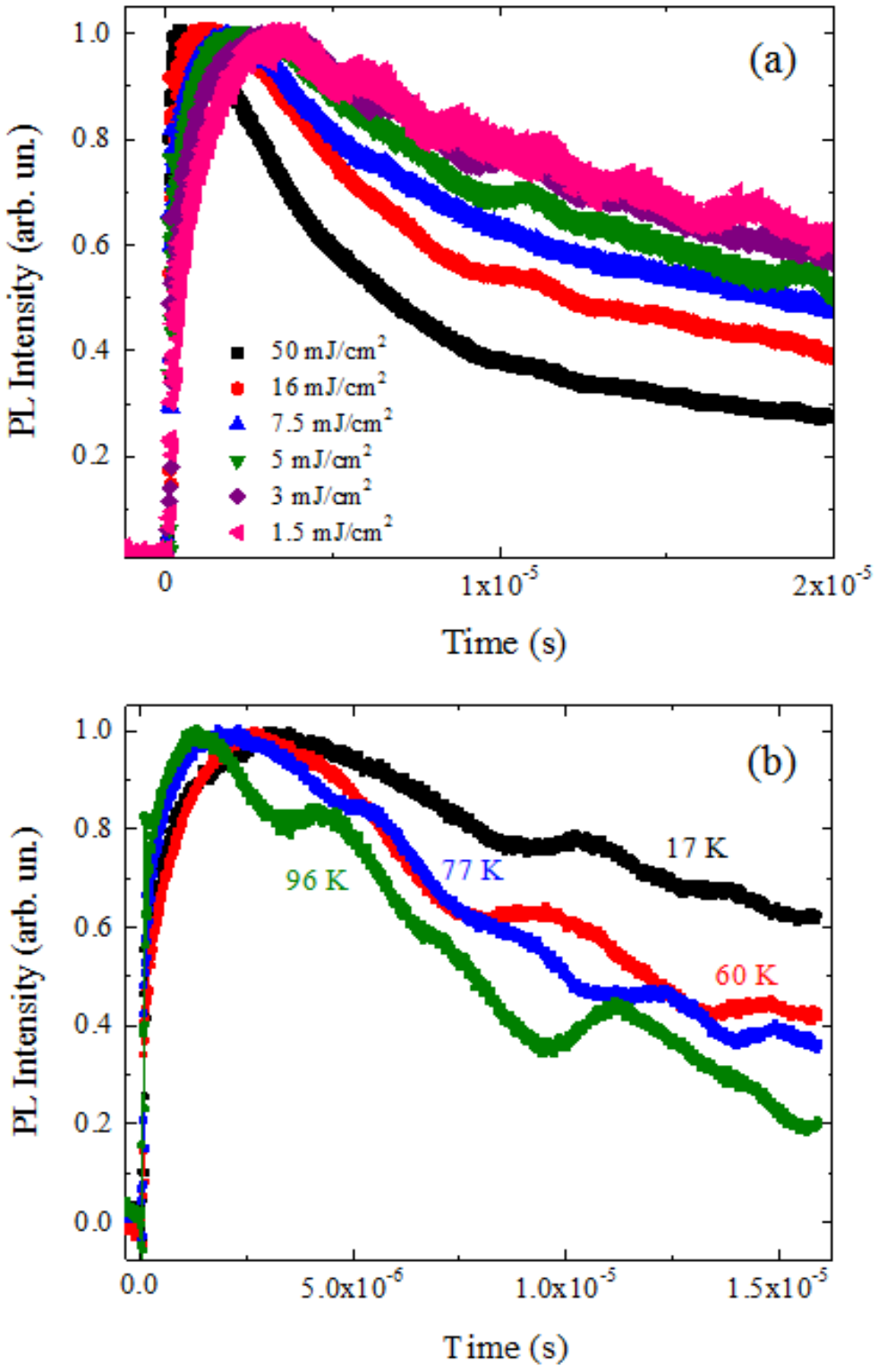

Figure 4.18 The normalized PL spectra peaked at 0.8 eV measured for different (a) excitation energy densities (E = 50 mJ/cm^2) and (b) temperatures (T = 17 K).

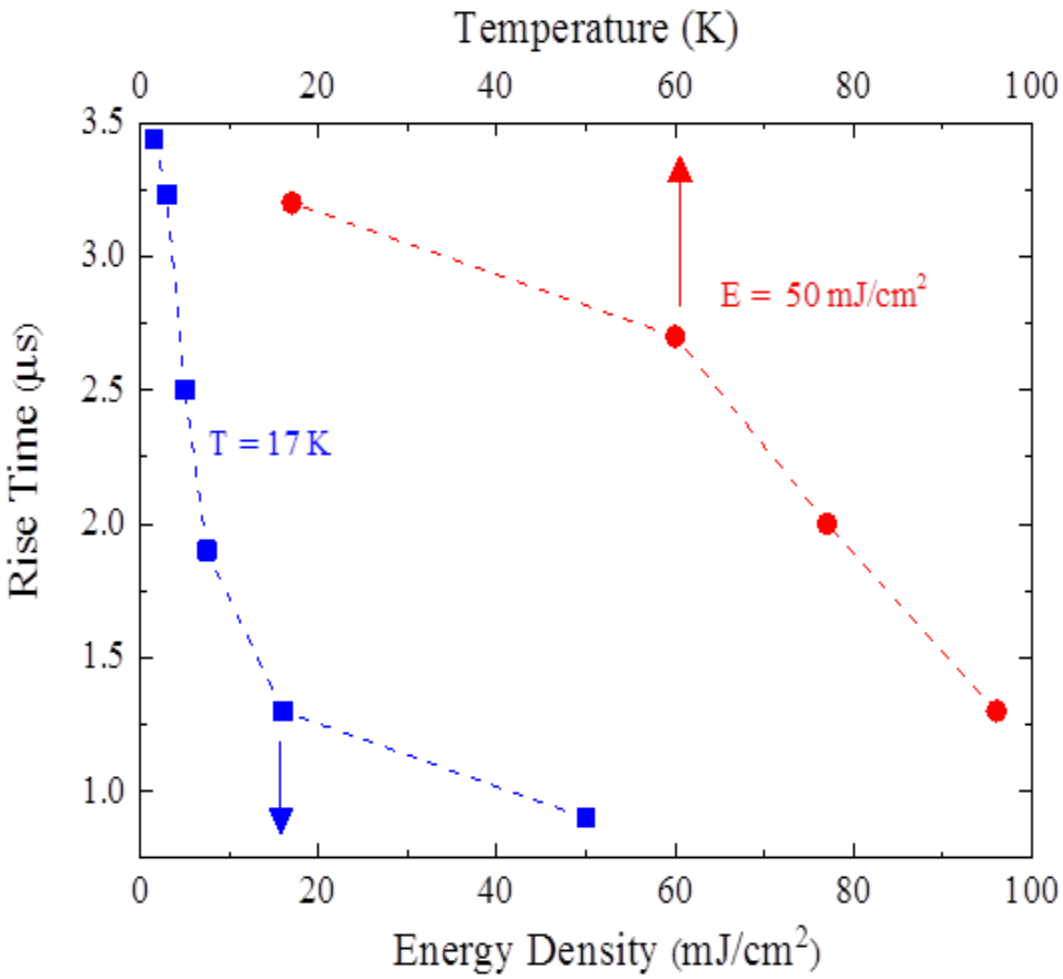

Figure 4.19 The 0.8 eV PL rise time is shown as a function of excitation energy density and temperature.

It is observed that the PL rise time decreases with the increasing excitation energy density and temperature. Note that the PL peaked at 0.8 eV has a rise time close to 2–3 μs while the 0.92 eV PL rises faster than 2.5 ns (the time resolution of the system).

Figure 4.20 presents the PL dynamics measured using 355 nm wavelength and 6 ns-long pulsed laser excitation with an energy density of ~50 mJ/cm^2. In agreement with our expectations (also, in reference [138]), the PL peaked at 0.92 eV is found to be decaying much faster compared to the PL peaked at 0.8 eV.

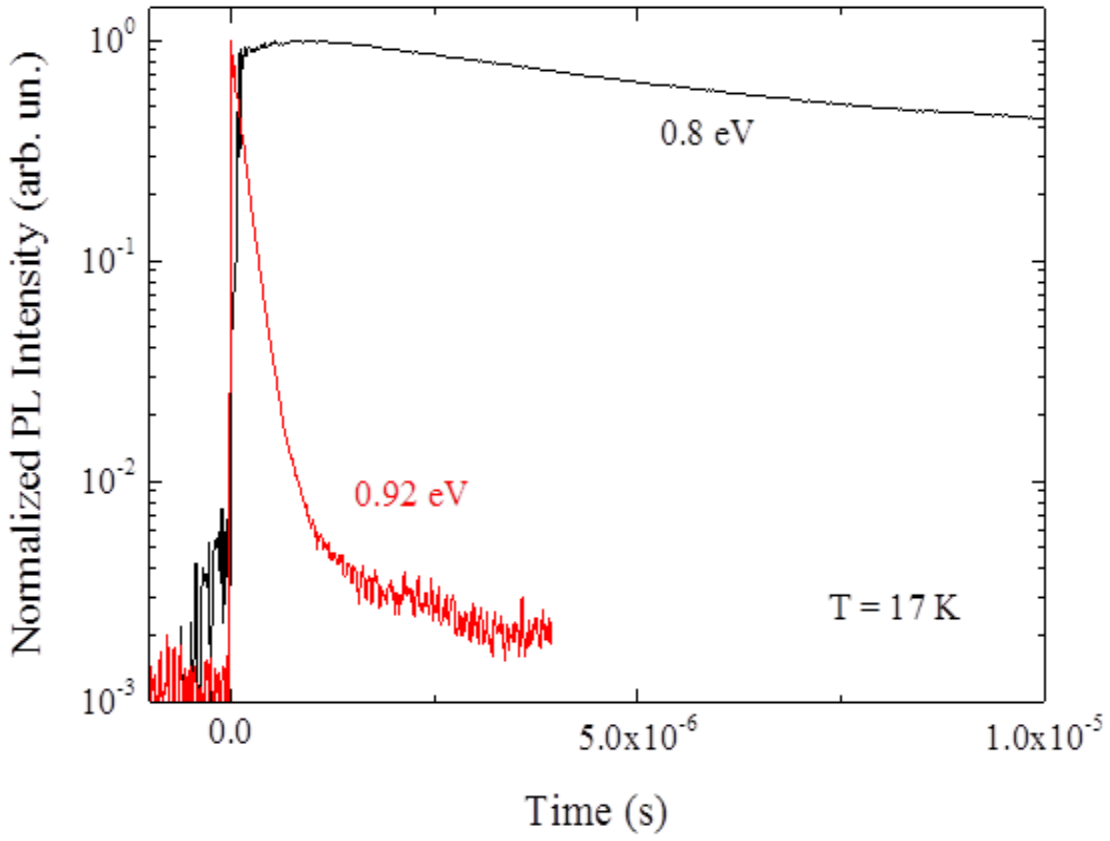

Figure 4.20 Time-resolved PL decays under pulsed excitation energy density of 50 mJ/cm^2 recorded at indicated photon energies.

Non-exponential decays are found for both PL bands of the Si/SiGe nanostructures. The observed non-exponential PL decays suggest that in both cases the carrier recombination processes are characterized by a time-dependent recombination rate, R_i. Thus, the carrier concentration n decay rate is given by:

$$\frac{dn}{dt} = R_i = -\frac{n}{\tau_i(t)}, \tag{4.14}$$

where $\tau_i(t)$ is an instant lifetime. It can be directly extracted from the PL dynamics according to the equation:

$$I_{PL}/I_0 = \exp(\frac{-t}{\tau_i(t)}), \tag{4.15}$$

where I_{PL}/I_0 is the normalized PL intensity. Figure 4.21 shows the instant carrier lifetime as a function of time fitted using equation:

$$\tau_i(t) = \tau_0 + \tau_1 \times t^{\alpha}, \tag{4.16}$$

where τ_0, τ_1, and α are the constants.

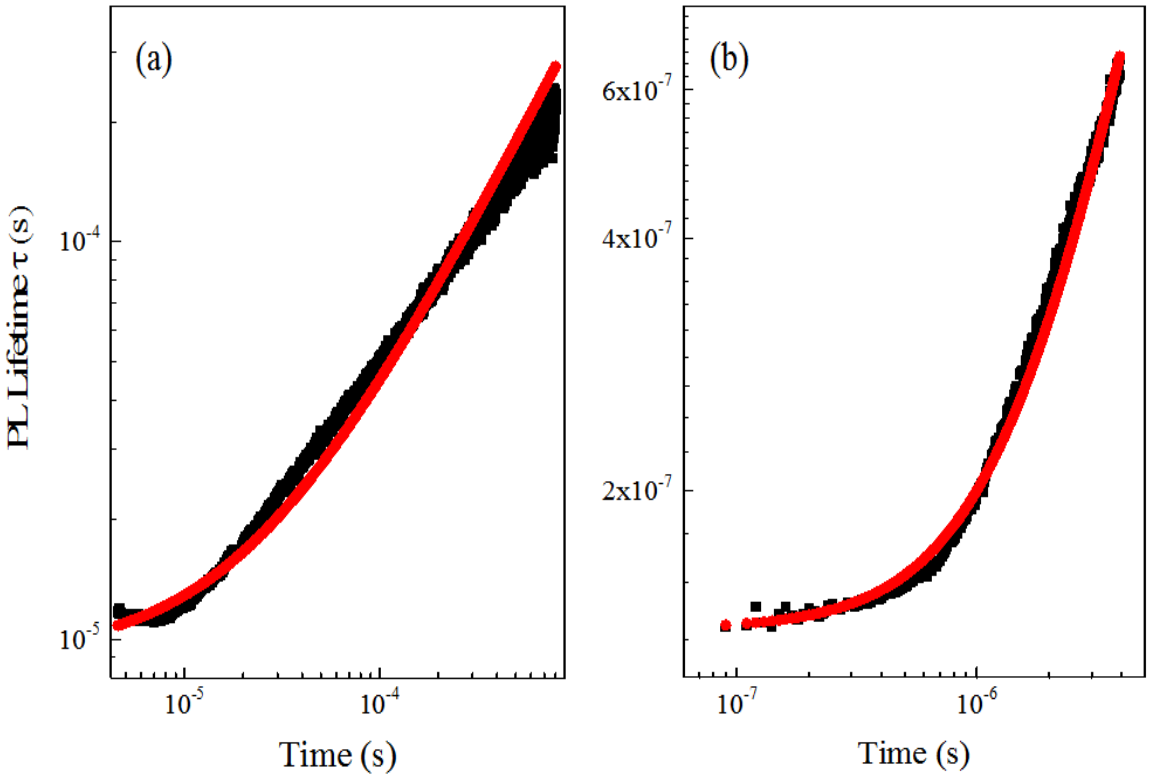

Figure 4.21 PL lifetime as a function of time extracted from the PL decay data for (a) SiGe cluster (~ 0.8 eV) and (b) SiGe NL (~ 0.92 eV). Circles show the fitting data.

Figure 4.22 presents the time-dependent recombination rate, $R_i(t) \sim \frac{1}{\tau_i(t)}$. The recombination rate for the PL band peaked at 0.8 eV is ~ 10^5 - 10^4 s^{-1}, and it is in the range of 10^6 – 10^7 s^{-1} for the 0.92 eV peaked PL.

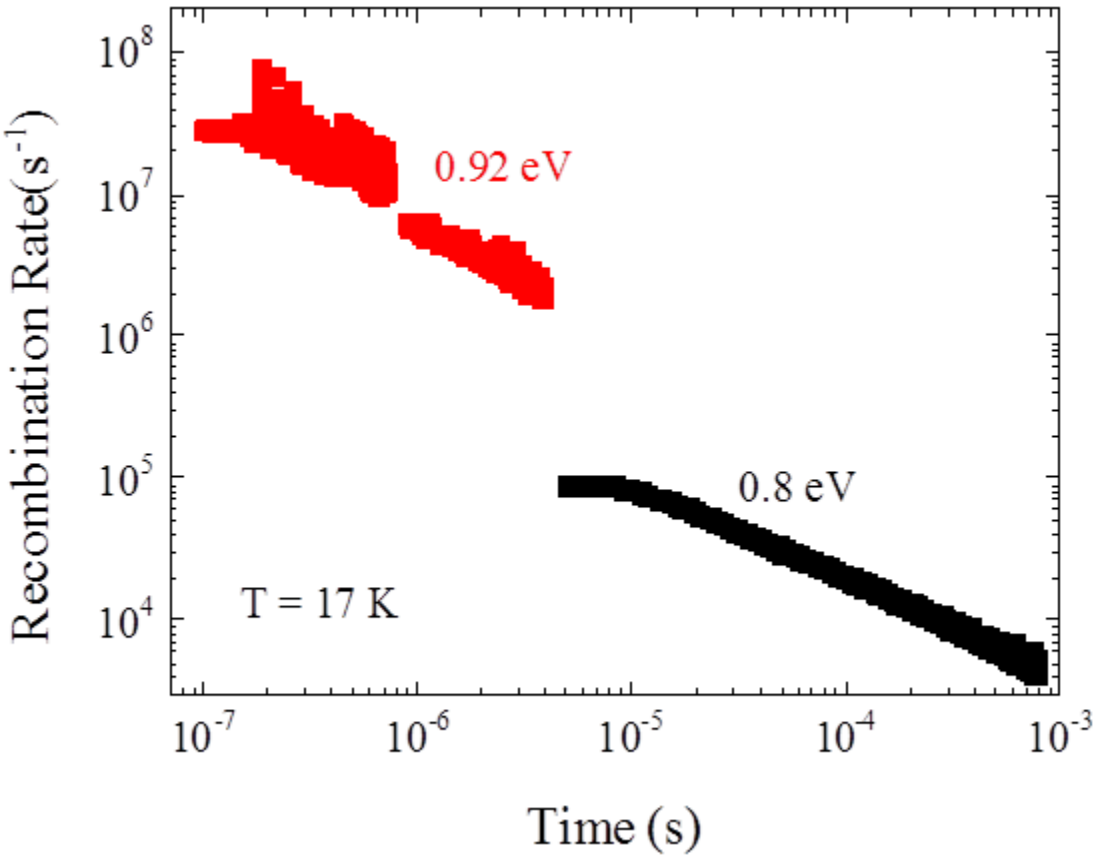

Figure 4.22 Carrier recombination rate as a function of time calculated using the PL decay data for two indicated photon energies.

4.2.2 Discussion

In Si/SiGe nanostructures at low temperature, carrier diffusion is found to be negligible [124]. Thus, the observed difference in the PL spectra obtained using shorter (325 nm) and longer (365 nm) wavelength excitation [Figure 4.14] is expected to be due to the difference in photoexcitation penetration depth, which is ~ 10^{-6} cm for the shorter and ~

10^{-5} cm for the longer wavelength excitation [10, 124]. Therefore, the PL peaked at ~0.9 eV is mostly associated with the 4-5 nm thick $Si_{1-x}Ge_x$ single NL where $x \approx 8\%$, while the PL with a maximum at ~ 0.8 eV is related to $Si_{1-x}Ge_x$ cluster multilayers with x approaching 40%. Compared to bulk $Si_{1-x}Ge_x$ alloys with similar composition x [23], the PL in $Si_{1-x}Ge_x$ clusters is shifted toward lower photon energies, which is most likely due to strain and strain-induced $Si/Si_{1-x}Ge_x$ interfacial mixing [139, 140].

Using pulsed laser excitation with 355 nm wavelength, a PL signal associated with both the SiGe NLs and SiGe clusters is obtained. The measured time-integrated PL signal (recorded using a lock-in amplifier and a millisecond accumulation time window) shows the PL peak at ~ 0.8 eV with a visible shoulder at ~ 0.9 eV [Figure 4.15]. An alternative approach to checking the PL dynamics is to use a storage oscilloscope with an adjustable time window and directly record the PL peak intensity at different wavelengths. Using this method and a shorter (~ 0.1 μs) accumulation time, the PL maximum intensity is found at ~ 0.92 eV [Figure 4.15]. This result indicates that under 355 nm pulsed excitation, the PL at 0.92 eV decays faster compared to the 0.8 eV PL. This conclusion is in an agreement with the previously reported results in Si/SiGe nanostructures showing that the PL detected at longer wavelengths, in general, has a longer lifetime [138]. Note that in both experiments no PL associated with dislocations is found (i.e., there is no sharp D-line PL at 0.81 eV, 0.86 eV, 0.94 eV, and 1.0 eV [141]).

Figure 4.17 shows that the 0.8 eV peaked PL is sub-linear while the 0.92 eV PL intensity is linear versus excitation energy density, and this explains why the 0.92 eV PL dominates at a higher excitation energy density. The linear dependence of the 0.92 eV peaked PL intensity versus excitation energy density indicates that the measured

recombination rate of 10^6 – 10^7 s^{-1} is mostly due to radiative recombination. Since radiative recombination competes with Auger recombination, the long-lived PL should saturate sooner compared to the short-lived PL. In agreement with this presumption, Figure 4.20 confirms that the 0.8 eV peaked PL decay is significantly slower compared to the 0.92 eV peaked PL decay. On the other hand, the 0.8 eV PL rise time as a function of excitation energy density shows different behavior at low and high excitation energy densities, as is shown in Figure 4.19. The observed PL rise time of ~ 2-3 μs is much longer than the laser pulse (~ 6 ns). This unusually long PL rise time could be associated with an Auger-assisted carrier spatial redistribution in Si/SiGe nanostructures known as the Auger fountain [142]. The temperature dependence of the PL rise time at high excitation density (~50 mJ/cm^2) also confirms that the Auger fountain could be responsible for the unusual PL dynamics [143].

Non-exponential PL decays have been reported previously in Si/SiGe nanostructures, and they were fitted variously by a stretched exponential function $\exp[(-t/\tau)^{\beta}]$, a power function $1/(1+\alpha t)^{m}$ or multiple exponential decays [138, 141, 144]; however, the underlying physical mechanism involved has not been identified. It has been pointed out that the stretched exponential PL decay is observed in a wide variety of systems, and it provides a good empirical fit but, most likely, has no fundamental significance [145]. As presented in this work, the direct extraction of instant carrier lifetimes from the PL decay is a simple procedure, and it is not bound to any particular model or assumption. The instant carrier lifetimes are well fitted following equation 4.16, shown in Figure 4.21. It is found that $\tau_o \approx 1.37\times10^{-7}$ s and $\alpha \approx 1.5$ for the 0.92 eV PL band and $\tau_o \approx 9\times10^{-6}$ s and $\alpha \approx 0.96$ for the PL band peaked at 0.8 eV. Figure 4.22 shows

that initially both PL bands have almost time-independent recombination rates with corresponding single-exponential decays of ~ 3×10^7 s^{-1} for the PL band peaked at 0.92 eV and ~ 9×10^4 s^{-1} for the 0.8 eV PL band. As time increases, the recombination rate decreases, and $R_i(t)\sim t^{-\alpha}$ with $\alpha \approx 0.82$ for the PL band peaked at 0.92 eV and $\alpha \approx 0.67$ for the 0.8 eV peaked PL band.

Assuming a type II energy band alignment at a Si/SiGe hetero-interface with an energy barrier mostly in the valence energy band (ΔE_V), holes are localized within SiGe and electrons are located in Si [123, 138]. In this model, two major factors contribute to the electron-hole recombination rate (i.e., speed of the PL decay). The first factor, similarly to that in donor-acceptor pair recombination model [146], it is assumes that the electron-hole time-dependent recombination rate depends on the average distance separating electrons and holes, a_{e-h}. The recombination-rate distance dependence is expressed by

$$R(a) = R_0 exp(-\frac{a_{e-h}}{a_{ex}}), \tag{4.17}$$

where R_0 and a_{ex} are the maximum recombination rate [~ 7×10^7 s^{-1}, see Figure 4.22] and a minimal radius of the localized exciton at the Si/SiGe hetero-interface (~ 1.5 nm), respectively. It is assumed that the holes are localized within SiGe and the electrons are located in Si, which is due to the previously discussed type II energy band alignment at the Si/SiGe hetero-interface. In the $Si_{1-x}Ge_x$ nano-layer with $x \approx 8\%$, $a_{e-h} \leq 5$ nm (which is comparable to the thickness of the SiGe nano-layer) is found while in $Si_{1-x}Ge_x$ clusters

with $0 \leq x \leq 40\%$, it is found 9 nm < a_{e-h} < 14 nm (Figure 4.23). These results are in a good agreement with the TEM and EDX data (Figures 3.1 (d) and 3.2 (c)).

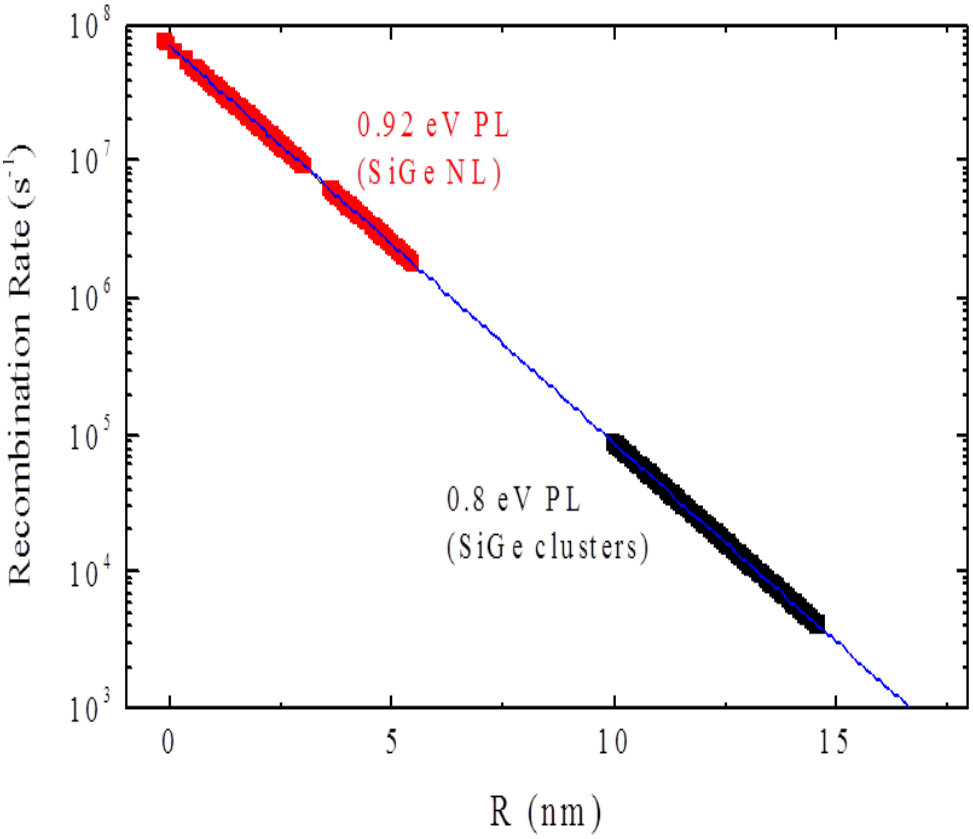

Figure 4.23 Carrier recombination rates (dots) extracted from the experimental data as a function of the distance between electrons and holes for photon detection energies associated with SiGe NL PL (~ 0.92 eV) and SiGe cluster PL (~ 0.8 eV). The solid line is the theoretically calculated electron-hole recombination rate (Equation 4.17).

The second factor is the energy barrier for holes ΔE_V, which is much greater compared to the energy barrier for electrons [10], and it can be estimated from $E_G^{Si} - E_{PL} \approx \Delta E_V$ where E_G^{Si} is the Si energy gap and E_{PL} is the photon energy of the PL peak. The data show that for NLs of $Si_{1-x}Ge_x$ with $x \approx 8\%$ the hole energy barrier is $\Delta E_V^{NL} \approx$ 0.18 eV, and for CMs of $Si_{0.6}Ge_{0.4}$ it is $\Delta E_V^{CM} \approx 0.3$ eV. Both factors contribute to the

electron-hole recombination rate; it decreases exponentially as both a_{e-h} and ΔE_V increases [147]. Thus, in a low Ge content SiGe NL, electron-hole recombination should occur ~1000 times faster compared to that in Ge-rich SiGe CMs. An alternative explanation might involve different types of luminescence centers, most likely uncontrollable impurities localized at the Si/SiGe hetero-interface. However, the MBE growth environment was very clean, and there is no clear experimental evidence (e.g., additional PL lines, etc.) pointing to the existence of such centers.

CHAPTER 5

CONCLUSION

Over the last few decades, $Si/Si_{1-x}Ge_x$ NSs are considering as promising candidates in the field of optoelectronic and thermoelectric devices. The lattice-mismatch-induced strain in growth of $Si_{1-x}Ge_x$ layers on Si can be used to tailor the physical properties of $Si/Si_{1-x}Ge_x$ NSs. This dissertation has described a complete study of structural, optical, and thermal properties of strain engineered multilayers $Si/Si_{1-x}Ge_x$ NSs using Raman and PL spectroscopy. A comprehensive quantitative analysis of Raman scattering in $Si/Si_{1-x}Ge_x$ NSs with known chemical composition, dimensions, and heterointerface abruptness is discussed in the first part of the dissertation. In the second part, detailed investigation of the PL signal in SiGe NL embedded in multilayers Si/SiGe clusters is presented and electron-hole time-dependent recombination rate is discussed using the donor-acceptor pair recombination model.

Raman experiments have been set up with the aim of measuring Raman spectra of different geometries, thicknesses, and Ge compositions of $Si/Si_{1-x}Ge_x$ NSs in a spectroscopic range of 0-1200 cm^{-1}. The observed variations in the baseline of the Raman spectrum are attributed to the sample surface imperfection and notable instrumental response associated with stray light. The baseline correction is used for precise estimation of Raman peak's position, intensity, and full width at half maximum.

The PL measurements are performed using CW and pulse laser excitation of the MBE grown Si/SiGe NSs. A fast and intense PL signal has been found in a SiGe NL at 0.92 eV embedded in multilayers Si/SiGe clusters. Electron-hole recombination in non-

uniform multilayers Si/SiGe NSs has been discussed. A model has been proposed to explain the time-dependent carrier recombination found in SiGe QW and SiGe clusters. Using different excitation light wavelengths, the dependence of the Raman scattering intensity on the light penetration depth in $Si/Si_{1-x}Ge_x$ NSs is demonstrated. The Ge content x and strain are calculated using the Raman signal integrated intensity and frequency methods, and the results are in a good agreement with the EDX data. Details of low-frequency folded longitudinal acoustic phonon modes and second-order Raman scattering in these samples are explained. Using the measured Stokes/anti-Stokes Raman spectra and the developed model of heat dissipation in the samples exposed to an intense laser radiation during Raman measurements, the sample local temperatures and thermal conductivities are calculated. It is observed that an increase in the SiGe/Si volume fraction ratio strongly contributes to the decrease in thermal conductivity of $Si/Si_{1-x}Ge_x$ NSs. The results are important for the development of quantitative and non-destructive metrological procedures and for determining the thermal properties of a wide variety of SiGe based nanoscale electronic, photonic, and thermoelectric devices.

Experimental results from PL measurements indicate that a 3-5 nm thick $Si/Si_{0.92}Ge_{0.08}$ layer with an abrupt (~ 1 nm) heterointerface incorporated into a $Si_{0.6}Ge_{0.4}$ CMs shows no structural (TEM) or spectroscopic (PL) evidences of dislocations, and it produces a remarkably strong PL signal at 0.92 eV (SiGe NL) with characteristic decay time ~ 1000 times shorter compared to that in Si/SiGe clusters. This intense and short-lived PL does not saturate as a function of excitation energy density up to 50 mJ/cm^2. The experimentally observed non-exponential PL decay in Si/SiGe nanostructures is explained to be due to variations of the distances separating electrons and holes at the

Si/SiGe heterointerface. This novel design reduces the carrier radiative recombination lifetime, increases the PL quantum efficiency, and makes these SiGe nanostructures promising candidates for applications in light-emitting devices monolithically integrated into CMOS environment.

In conclusion, Raman and PL spectroscopies are two powerful techniques used to characterize multilayer $Si/Si_{1-x}Ge_x$ NSs. Raman spectroscopy is an effective method for precise measurements of the Ge content and strain in $Si_{1-x}Ge_x$ alloy. It also allows predicting the thermal conductivity in low-dimensional Si/SiGe NSs and thus, makes possible to control the heat dissipation in thermoelectric devices. The performed PL studies are used to develop a model of electron-hole recombination in SiGe QW embedded in multilayers Si/SiGe clusters. This novel device with enhanced PL quantum efficiency will lead to the technological developments in Si photonics.

REFERENCES

1. L. Pavesi, L. D. Negro, C. Mazzoleni, G. Franzo, and F. Priolo, "Optical gain in silicon nanocrystals," Nature, vol. 408, pp. 440-444, 2000.

2. M. Nirmal and L. Brus, "Luminescence photophysics in semiconductor nanocrystals," Acc. Chem. Res., vol. 32, pp. 407-414, 1999.

3. G. F. Grom, D. J. Lockwood, J. P. McCaffrey, H. J. Labbé, P. M. Fauchet, B. White Jr., J. Diener, D. Kovalev, F. Koch, and L. Tsybeskov, "Ordering and self-organization in nanocrystalline silicon," Nature, vol. 407, pp. 358-361, 2000.

4. B. V. Kamenev, G. F. Grom, D. J. Lockwood, J. P. McCafrey, B. Laikhtman, and L. Tsybeskov, "Carrier tunneling in nanocrystalline silicon–silicon dioxide superlattices: A weak coupling model," Phys. Rev. B, vol. 69, p. 235306, 2004.

5. Z. H. Lu, D. J. Lockwood, and J-M. Baribeau, "Quantum confinement and light emission in SiO_2/Si superlattices," Nature, vol. 378, pp. 258-260, 1995.

6. B. Zheng, J. Michel, F. Y. G. Ren, L. C. Kimerling, D. C. Jacobson, and J. M. Poate, "Room temperature sharp line electroluminescence at λ=1.54 μm from an erbium doped, silicon light emitting diode," Appl. Phys. Lett., vol. 64, pp. 2842-2844, 1994.

7. D. Leong, M. Harry, K. J. Reeson, and K. P. Homewood, "A silicon/iron-disilicide light-emitting diode operating at a wavelength of 1.5 μm," Nature, vol. 387, pp. 686-688, 1997.

8. J. Liu, X. Sun, D. Pan, X. Wang, L. C. Kimerling, T. L. Koch, and J. Michel, "Tensile-strained, n-type Ge as a gain medium for monolithic laser integration on Si," Opt. Express, vol. 15, pp. 11272-11277, 2007.

9. L. Tsybeskov and D. J. Lockwood, "Silicon-germanium nanostructures for light emitters and on-chip optical interconnects," Proc. of the IEEE, vol. 97, pp. 1284-1303, 2009.

10. D. J. Paul, "Si/SiGe heterostructures: from material and physics to devices and circuits," Sem. Sci. Tech., vol. 19, pp. R75-R108, 2004.

11. H. K. Shin, D. J. Lockwood, and J-M. Baribeau, "Strain in coherent-wave SiGe/Si superlattices," Solid State Commun., vol. 114, pp. 505-510, 2000.

12. J. M. Baribeau, X. Wu, and D. J. Lockwood, "Probing the composition of Ge dots and $Si/Si_{1-x}Ge_x$ island superlattices," J. Vac. Sci. Tech. A, vol. 24, pp. 663-667, 2006.

13. Y. Shiraki and A. Sakai, "Fabrication technology of SiGe hetero-structures and their properties," Surf. Sci. Rep., vol. 59, pp. 153-207, 2005.

14. J.-M. Baribeau, X. Wu, N. L. Rowell, and D. J. Lockwood, "Ge dots and nanostructures grown epitaxially on Si," J. Phys.: Condens. Matter, vol. 18, pp. R139-R174, 2006.

15. S. T. Huxtable, A. R. Abramson, C.-L. Tien, A. Majumdar, C. LaBounty, X. Fan, G. Zeng, J. E. Bowers, A. Shakouri, and E. T. Croke, "Thermal conductivity of Si/SiGe and SiGe/SiGe superlattices," Appl. Phys. Lett., vol. 80, pp. 1737-1739, 2002.

16. F. Schaffler, "High-mobility Si and Ge structures," Semicond. Sci. Technol., vol. 12, pp. 1515-1549, 1997.

17. J. D. Cresseler, "SiGe HBT technology: A new contender for Si-Based RF and microwave circuit applications," IEEE Transactions on Microwave Theory and Techniques, vol. 46, pp. 572-589, 1998.

18. D. J. Paul, P. See, I. V. Zozoulenko, K.-F. Berggren, B. Kabius, B. Holländer, and S. Mantl, "Si/SiGe electron resonant tunneling diodes," Appl. Phys. Lett., vol. 77, pp. 1653-1655, 2000.

19. Y. H. Xie, D. Monroe, E. A. Fitzgerald, P. J. Silverman, F. A. Thiel, and G. P. Watson, "Very high mobility two-dimensional hole gas in $Si/Ge_xSi_{1-x}/Ge$ structures grown by molecular beam epitaxy," Appl. Phys. Lett., vol. 63, pp. 2263-2264, 1993.

20. E. Kasper, H. J. Herzog, and H. Kibbel, "A one-dimensional SiGe superlattice grown by UHV epitaxy," Appl. Phys., vol. 8, pp. 199-205, 1975.

21. K. Brunner, "Si/Ge Nanostructures," Rep. Prog. Phys., vol. 65, pp. 27-72, 2002.

22. P. Yu and M. Cardona, Fundamentals of Semiconductors Physics and Material Properties, Third ed., New York: Springer, 2005.

23. J. Weber and M. I. Alonso, "Near-band-gap photoluminescence of Si-Ge alloys," Phys. Rev B, vol. 40, pp. 5683–5693, 1989.

24. http://www.ioffe.ru/SVA/NSM/Semicond/index.html (accessed on 12/04/2014).

25. K. Eberl, M. O. Lipinski, Y. M. Manz, W. Winter, N. Y. Jin-Phillipp, and O. G. Schmidt, "Self-assembling quantum dots for optoelectronic devices on Si and GaAs," Physica E, vol. 9, pp. 164-174, 2001.

26. C. G. Van de Walle and R. M. Martin, "Theoretical calculations of heterojunction discontinuities in the Si/Ge system," Phys. Rev. B, vol. 34, pp. 5621-5634, 1986.

27. R. People and J. C. Bean, "Band alignments of coherently strained Ge_xSi_{1-x}/Si heterostructures on <001> Ge_ySi_{1-y} substrates," Appl. Phys. Lett., vol. 48, pp. 538-540, 1986.

28. L. Colombo, R. Resta, and S. Baron, "Valence-band offsets at strained Si/Ge interfaces," Phys. Rev. B, vol. 44, pp. 5572-5579, 1991.

29. W.-X. Ni, J. Knall, and G. V. Hansson, "New method to study band offsets applied to strained Si/$Si_{1-x}Ge_x$ (100) heterojunction interfaces," Phys. Rev. B, vol. 36, pp. 7744-7747, 1987.

30. K. Nauka, T. I. Kamins, J. E. Turner, C. A. King, J. L. Hoyt, and J. F. Gibbons, "Admittance spectroscopy measurements of band offsets in Si/$Si_{1-x}Ge_x$/Si heterostructures," Appl. Phys. Lett.,vol. 60, pp. 195–197, 1992.

31. K. Schmalz, I. N. Yassievich, H. Rucker, H. G. Grimmeiss, H. Frankenfeld, W. Mehr, H. J. Osten, P. Schley, and H. P. Zeindl, "Characterization of Si/$Si_{1-x}Ge_x$/Si quantum wells by space-charge spectroscopy," Phys. Rev. B, vol. 50, pp. 14287-14301, 1994.

32. M. L. W. Thewalt, D. A. Harrison, C. F. Reinhart, and J. A. Wolk, "Type II band alignment in $Si_{1-x}Ge_x$/Si (001) quantum wells: The ubiquitous type I luminescence results from band bending," Phys. Rev. Lett., vol. 79, pp. 269-272, 1997.

33. T. Baier, U. Mantz, K. Thonke, R. Sauer, F. Schaffler, and H. -J. Herzog, "Type II band alignment in Si/$Si_{1-x}Ge_x$ quantum wells from photoluminescence line shifts due to optically induced band-bending effects: Experiment and theory," Phys. Rev B, vol. 50, pp. 15191-15196, 1994.

34. R. L. Anderson, "Experiments on Ge-GaAs heterojunctions," Solid-State Electronics, vol. 5, pp. 341-351, 1962.

35. R. Braunstein, A. R. Moore, and F. Herman, "Intrinsic optical absorption in germanium-silicon alloys," Phys. Rev., vol. 109, pp. 695-710, 1958.

36. Y. P. Varshni, "Temperature dependence of the energy gap in semiconductors," Physica, vol. 34, pp. 149-154, 1967.

37. J. P. Dismukes, L. Ekstrom, and R. J. Paff, "Lattice parameter and density in germanium-silicon alloys," J. Phys. Chem., vol. 35. pp. 3021-3027, 1964.

38. J. W. Mattthews and A. E. Blakeslee, "Defects in epitaxial multilayers: III. Preparation of almost perfect multilayers," J. Cryst. Growth, vol. 32, pp. 265-273, 1976.

39. R. People and J. C. Bean, "Calculation of critical layer thickness versus lattice mismatch for Ge_xSi_{1-x}/Si strained layer heterostructures," Appl. Phys. Lett., vol. 47, pp. 322-324, 1985.

40. B. W. Dodson and J. Y. Tsao, "Relaxation of strained layer semiconductor structures via plastic flow," Appl. Phys. Lett., vol. 51, pp. 1325-1327, 1987.

41. B. W. Dodson and J. Y. Tsao, "Erratum: Relaxation of strained layer semiconductor structures via plastic flow [Appl. Phys. Lett. 5 1, 1325 (1987)]," Appl. Phys. Lett., vol. 52, pp. 852-852, 1988.

42. J. C. Bean, L. C. Feldman, A. T. Fiory, S. Nakahara, and I. K. Robinson, "Ge_xSi_{1-x}/Si strained-layer superlattice grown by molecular beam epitaxy," J. Vac. Sci, Technol. A, vol. 2, pp. 436-440, 1984.

43. A. T. Fiory, J. C. Bean, R. Hull, and S. Nakahara, "Thermal relaxation of metastable strained-layer Ge_xSi_{1-x}/Si epitaxy," Phys. Rev. B, vol. 31, pp. 4063-4065, 1985.

44. R. H. Miles, T. C. McGill, P. P. Chow, D. C. Johnson, R. J. Hauenstein, C. W. Nieh, and M. D. Strathman, "Dependence of critical thickness on growth temperature in Ge_xSi_{1-x}/Si superlattices," Appl. Phys. Lett., vol. 52, pp. 916-918, 1988.

45. J. H. Van der Merwe, "Crystal interfaces. Part II. Finite overgrowths," J. Appl. Phys., vol. 34, pp. 123-127, 1963.

46. R. People and J. C. Bean, "Erratum: Calculation of critical layer thickness versus lattice mismatch for Ge_xSi_{1-x}/Si strained layer heterostructures [Appl. Phys. Lett. 4 7, 322 (1985)]," Appl. Phys. Lett., vol. 49, pp. 229-229, 1986.

47. M Ohring, Materials Science of Thin Films, Second Ed., New York: Academic Press, 2001.

48. R. Hull and J. C. Bean, "Misfit dislocations in lattice-mismatched epitaxial films," Critical Reviews in Solid State and Material Sciences, vol. 17, pp. 507-546, 1992.

49. J. -M. Baribeau, X. Wu, M. -J. Picard, and D. J. Lockwood, in Group IV Semiconductor Nanostructures – 2006, L. Tsybeskov, D. J. Lockwood, C. Delerue, M. Ichikawa, and A. W. van Buuren, Eds., Mat. Res. Soc., Pittsburgh, p. 119, 2007.

50. L. Tsybeskov, E.-K. Lee, H.-Y. Chang, D. J. Lockwood, J.-M. Baribeau, X. Wu, and T. I. Kamins, "Silicon-germanium nanostructures for on-chip optical interconnects," Appl. Phys. A, vol. 95, pp. 1015-1027, 2009.

51. A. Vailionis, B, Cho, G. Glass, P. Desjardins, D. J. Cahill, and J. E. Greene, "Pathway for the strain-driven two-dimensional to three-dimensional transition during growth of Ge on Si(001)," Phys. Rev. Lett., vol. 85, pp. 3673-3675, 2000.

52. G. Medeiros-Ribeiro, A. M. Bratkovski, T. I. Kamins, D. A. A. Ohlberg, and R. S. Williams, "Shape transition of germanium nanocrystals on a Silicon (001) surface from pyramids to domes," Science, vol. 279, pp. 353-355, 1998.

53. F. M. Ross, R. M. Tromp, and M. C. Reuter, "Transition states between pyramids and domes during Ge/Si island growth," Science, vol. 286, pp. 1931-1934, 1999.

54. W. L. Henstrom, C.-P. Liu, J. M. Gibson, T. I. Kamins, and R. S. Williams, "Dome-to-pyramid shape transition in Ge/Si islands due to strain relaxation by interdiffusion," Appl. Phys. Lett., vol. 77, pp. 1623-1625, 2000.

55. T. I. Kamins, G. Medeiros-Ribeiro, D. A. A. Ohlberg, and R. Stanley Williams, "Evolution of Ge islands on Si(001) during annealing," J. Appl. Phys., vol. 85, pp. 1159-1171, 1999.

56. A. Rastelli, M. Kummer, and H. von Käne, "Reversible shape evolution of Ge islands on Si(001)," Phys Rev. Lett., vol. 87, p. 256101, 2001.

57. D. G. Cahill, W. K. Ford, K. E. Goodson, G. D. Mahan, A. Majumdar, H. J. Maris, R. Merlin, and S. R. Phillpot, "Nanoscale thermal transport," J. Appl. Phys., vol. 93, pp. 793-818, 2003.

58. B. Yang, G. Chen, in Thermal Conductivity: Theory, Properties, and Applications, T. M. Tritt, Ed., New York: Springer, 2004, pp. 167-186.

59. Z. Aksamija and I. Knezevic, "Thermal conductivity in Si/Ge and Si/SiGe superlattices," 11th IEEE Intl. Conf. on Nanotechnol., pp. 278-281, 2011.

60. H. J. Goldsmid, Thermoelectric Refrigeration, New York: Plenum Press, 1964.

61. S.-M. Lee, D. G. Cahill, and R. Venkatasubramanian, "Thermal conductivity of Si–Ge superlattices," Appl. Phys. Lett., vol. 70, pp. 2957-2959, 1997.

62. A. J. Minnich, H. Lee, X. W. Wang, G. Joshi, M. S. Dresselhaus, Z. F. Ren, G. Chen, and D. Vashaee, "Modeling study of thermoelectric SiGe nanocomposites," Phys. Rev. B, vol. 80, p. 155327, 2009.

63. D. Li, Y. Wu, P. Kim, L. Shi, P. Yang, and A. Majumdar, "Thermal conductivity of individual silicon nanowires," Appl. Phys. Lett., vol. 83, pp. 2934-2936, 2003.

64. N. Mingo, "Calculation of Si nanowire thermal conductivity using complete phonon dispersion relations," Phys. Rev. B, vol. 68, p. 113308, 2003.

65. L. D. Hicks and M. S. Dresselhaus, "Effect of quantum-well structures on the thermoelectric figure of merit," Phys. Rev. B, vol. 47, p. 12727, 1993.

66. G. Chen, "Thermal conductivity and ballistic-phonon transport in the cross-plane direction of superlattices," Phys. Rev. B, vol. 57, pp. 14958-14973, 1998.

67. J. Yang, in Thermal Conductivity: Theory, Properties, and Applications, T. M. Tritt, Ed., New York: Springer, 2004, pp. 205-237.

68. C. J. Glassbrenner and G. A. Slack, "Thermal conductivity of silicon and germanium from 3°K to the melting point," Phys. Rev., vol. 134, pp. A1058-A1069, 1964.

69. D. G. Cahill, M. Katiyar, and J. R. Abelson, "Thermal conductivity of *a*-Si:H thin films," Phys. Rev. B, vol. 50, pp. 6077-6081, 1994.

70. D. G. Cahill and R. O. Pohl, "Thermal properties of a tetrahedrally bonded amorphous solid: $CdGeAs_2$," Phys. Rev. B, vol. 37, pp. 8773-8780, 1988.

71. T. Borca-Tasciuc, W. Liu, J. Liu, T. Zeng, D. W. Song, C. D. Moore, G. Chen, K. L. Wang, and M. S. Goorsky, "Thermal conductivity of Si/Ge superlattices," in Proceedings of the Eighteenth International Conference on Thermoelectrics, IEEE, New York, pp. 201-204, 1999.

72. G. Chen, S. Q. Zhou, D.-Y. Yao, C. J. Kim, X. Y. Zheng, Z. L. Liu, K. L. Wang, X. Sun, and M. S. Dresselhaus, in Proceedings of the Seventeenth International Conference on Thermoelectrics, IEEE, New York, p. 202, 1998.

73. R. Cheaito, J. C. Duda, T. E. Beechem, K. Hattar, J. F. Ihlefeld, D. L. Medlin, M. A. Rodriguez, M. J. Campion, E. S. Piekos, and P. E. Hopkins, "Experimental investigation of size effects on the thermal conductivity of silicon-germanium alloy thin films," Phys. Rev. Lett., vol. 109, p. 195901, 2012.

74. G. Chen, "Size and interface effects on thermal conductivity of superlattices and periodic thin-film structures," J. Heat Transfer, vol. 119, pp. 220-229, 1997.

75. W. L. Liu, T. Borca-Tasciuc, G. Chen, J. L. Liu, and K. L. Wang, "Anisotropic thermal conductivity of Ge quantum-dot and symmetrically strained Si/Ge superlattices," J. Nanosci. Nanotech., vol. 1, pp. 39-42, 2001.

76. B. Yang and G. Chen, "Partially coherent phonon heat conduction in superlattices," Phys. Rev. B, vol. 67, p. 195311, 2003.

77. S. Y. Ren and J. D. Dow, "Thermal conductivity of superlattices," Phys. Rev. B, vol. 25, pp. 3750-3755, 1982.

78. G. Chen, C. L. Tien, X. Wu, and J. S. Smith, "Thermal diffusivity measurement of GaAs/AlGaAs thin-film structures," J. Heat Transfer, vol. 116, pp. 325-331, 1994.

79. P. Hyldgaard and G. D. Mahan, "Phonon superlattice transport," Phys. Rev. B, vol. 56, pp. 10754-10757, 1997.

80. S. Tamura, Y. Tanaka, and H. J. Maris, "Phonon group velocity and thermal conduction in superlattices," Phys. Rev. B, vol. 60, pp. 2627-2630, 1999.

81. R. Venkatasubramanian, "Lattice thermal conductivity reduction and phonon localization like behavior in superlattice structures," Phys. Rev. B, vol. 61, pp. 3091-3097, 2000.

82. G. Chen, "Phonon wave heat conduction in thin films and superlattices," J. Heat Transfer, vol. 121, pp. 945-953, 1999.

83. T. Borca-Tascuic and G. Chen, in Thermal Conductivity: Theory, Properties, and Applications, T. M. Tritt, Ed., New York: Springer, 2004.

84. D. Chescoe and P. J. Goohhew, The Operations of Transmission and Scanning Electron Microscopes, Oxford: Oxford University press, 1990.

85. P. B. Hirsh, A. Howie, R. B. Nicholson, and D. W. Pawshley, Electron Microscopy of Thin Crystals, Washington, DC: Butterworths, 1965.

86. D. B. Williams and C. B. Carter, Transmission Electron Microscopy: A Textbook for Material Science, New York: Plenum press, 1996.

87. L. Reimer and H. Kohl, Transmission Electron Microscopy: Physics of Image Formation, New York: Springer, 2008.

88. D. J. Lockwood and J.-M. Baribeau, "Strain-shift coefficients for phonons in $Si_{1-x}Ge_x$ epilayers on silicon," Phys. Rev. B, vol. 45, pp. 8565-8571, 1992.

89. S. Nakashima, T. Mitani, M. Ninomiya, and K. Matsumoto, "Raman investigation of strain in Si/SiGe heterostructures: Precise determination of the strain-shift coefficient of Si bands" J. Appl. Phys., vol. 99, p. 053512, 2006.

90. J. S. Lannin, "Vibrational and Raman-scattering properties of crystalline $Ge_{1-x}Si_x$ alloys," Phys. Rev. B, vol. 16, pp. 1510-1518, 1977.

91. H. D. Fuchs, C. H. Grein, M. I. Alonso, and M. Cardona, "High-resolution Raman spectroscopy of Ge-rich *c*-$Ge_{1-x}Si_x$ alloys: Features of the Ge-Ge vibrational modes" Phys. Rev. B, vol. 44, pp. 13120-13123, 1991.

92. H. H. Burke and I. P. Herman, "Temperature dependence of Raman scattering in $Ge_{1-x}Si_x$ alloys" Phys. Rev. B, vol. 48, pp. 15016-15024, 1993.

93. B. V. Kamenev, H. Grebel, L. Tsybeskov, T. I. Kamins, R. Stanley Williams, J. M. Baribeau, and D. J. Lockwood, "Polarized Raman scattering and localized embedded strain in self-organized Si/Ge nanostructures," Appl. Phys. Lett., vol. 83, pp. 5035-5037, 2003.

94. B. Dietrich, E. Bugiel, J. Klatt, G. Lippert, T. Morgenstern, H. J. Osten, and P. Zaumseil, "Measurement of stress and relaxation in $Si_{1-x}Ge_x$ layers by Raman line shift and x-ray diffraction," J. Appl. Phys., vol. 74, pp. 3177-3180, 1993.

95. J. B. Renucci, M. A. Renucci, and M. Cardona, "Volume dependence of the Raman frequencies of Ge-Si alloys," Solid State Commun., vol. 9, pp. 1651-1654, 1971.

96. M. A. Renucci, J. B. Renucci, and M. Cardona, "Raman scattering in Ge-Si alloys," Proceedings of the 2nd International Conference on Light Scattering in Solids, Flammarion, Paris, p. 326, 1971.

97. P. M. Mooney, F. H. Dacol, J. C. Tsang, and J. O. Chu, "Raman scattering analysis of relaxed Ge_xSi_{1-x} alloy layers," Appl. Phys. Lett., vol. 62, pp. 2069-2071, 1993.

98. F. Cerdeira, A. Pinczuk, J. C. Bean, B. Batlogg, and B. A. Wilson, "Raman scattering from Ge_xSi_{1-x}/Si strained layer superlattices," Appl. Phys. Lett., vol. 45, pp. 1138-1340, 1984.

99. T. S. Perova, J. Wasyluk, K. Lyutovich, E. Kasper, M. Oehme, K. Rode, and A. Waldron, "Composition and strain in thin $Si_{1-x}Ge_x$ virtual substrates measured by micro-Raman spectroscopy and x-ray diffraction," J. Appl. Phys., vol. 109, p. 033502, 2011.

100. M. I. Alonso and K. Winer, "Raman spectra of c-$Si_{1-x}G_x$ alloys," Phys. Rev. B, vol. 39, pp. 11056-10062, 1989.

101. J. C. Tsang, P. M. Mooney, F. Dacol, and J. O. Chu, "Measurements of alloy composition and strain in thin Ge_xSi_{1-x} layers," J. Appl. Phys., vol. 75, pp. 8098-8108, 1994.

102. W. J. Brya, "Raman scattering in Ge-Si alloys," Solid State Commun., vol. 12, pp. 253-257, 1973.

103. F. Pezzoli, E. Bonera, E. Grilli, M. Guzzi, S. Sanguinetti, D. Chrastina, G. Isella H. von Känel, E. Wintersberger, J. Stangl, and G. Bauer, "Raman spectroscopy determination of composition and strain in $Si_{1-x}Ge_x$/Si heterostructures," Mater. Sci. Semicond. Process., vol. 11, pp. 279-284, 2008.

104. F. Cerdeira, C. J. Buchenauer, F. H. Pollak, and M. Cardona, "Stress-induced shifts of first-order Raman frequencies of diamond- and zinc-blende-type semiconductors," Phys. Rev. B, vol.5, pp. 580-593, 1972.

105. E. Anastassakis, A. Cantarero, and M. Cardona, "Piezo-Raman measurements and anharmonic parameters in silicon and diamond," Phys. Rev. B, vol. 41, pp. 7529-7535, 1990.

106. M. Stoehr, D. Aubel, S. Juillaguet, J. L. Bischoff, L. Kubler, D. Bolmont, F. Hamdani, B. Fraisse, and R. Fourcade, "Phonon strain-shift coefficients of $Si_{1-x}Ge_x$ grown on Ge(001)," Phys. Rev. B, vol. 53, pp. 6923-6926, 1996.

107. P. H. Tan, K. Brunner, D. Bougeard, and G. Abstreiter, "Raman characterization of strain and composition in small-sized self-assembled Si/Ge dots," Phys. Rev. B, vol. 68, p. 125302, 2003.

108. J. Schmidt, G. Vogg, F. Bensch, S. Kreuzer, P. Ramm, S. Zollner, R. Liu, and P. Wennekers, "Spectroscopic techniques for characterization of high-mobility strained-Si CMOS," Mater. Sci. Semicond. Process., vol. 8, pp. 267-271, 2005.

109. J. S. Reparaz, A. Bernardi, A. R. Goni, M. I. Alonso, and M. Garriga, "Composition dependence of the phonon strain shift coefficients of SiGe alloys revisited," App. Phys. Lett., vol. 92, p. 081909, 2008.

110. F. Pezzoli, E. Bonera, E. Grilli, M. Guzzi, S. Sanguinetti, D. Chrastina, G. Isella, H. von Känel, E. Wintersberger, J. Stangl, and G. Bauer, "Phonon strain shift coefficients in $Si_{1-x}Ge_x$ alloys," J. Appl. Phys., vol. 103, p. 093521, 2008.

111. P. Y. Yu, "Comment on "Optical and acoustic phonon modes in self-organized Ge quantum dot superlattices" [Appl. Phys. Lett. 76, 586 (2000)]," Appl. Phys. Lett., vol. 78, pp. 1160-1161, 2001.

112. J. L. Liu, G. Jin, Y. S. Tang, Y. H. Luo, K. L. Wang, and D. P. Yu, "Optical and acoustic phonon modes in self-organized Ge quantum dot superlattices," Appl. Phys. Lett., vol. 76, pp. 586-588, 2000.

113. S. M. Rytov, "Acoustical properties of a thinly laminated medium," Sov. Phys. Acoust., vol. 2, pp. 68-80, 1956.

114. D. J. Lockwood, M. W. C. Dharma-wardana, J.-M. Baribeau, and D. C. Houghton, "Folded acoustic phonons in Si/Ge_xSi_{1-x} strained-layer superlattices," Phys. Rev. B, vol. 35, pp. 2243-2251, 1987.

115. P. A. Temple and C. E. Hathaway, "Multiphonon Raman spectrum of silicon," Phys. Rev. B, vol. **7**, pp. 3685-3697, 1973.

116. M. A. Renucci, J. B. Renucci, R. Zeyher, and M. Cardona, "Second-order Raman scattering in germanium in the vicinity of the E_1, $E_1+\Delta_1$ edges," Phys. Rev. B, vol. 10, pp. 4309-4323, 1974.

117. J. B. Renucci, R. N. Tyte, and M. Cardona, "Resonant Raman scattering in silicon," Phys. Rev. B, vol. 11, pp. 3885-3895, 1975.

118. Lorenzo Pavesi and Mario Guzzi, "Photoluminescence of $Al_xGa_{1-x}As$ alloys," J. Appl. Phys., vol. 75, pp. 4779-4842, 1994.

119. P. M. Fauchet, Monolithic silicon light sources, L. Pavesi and D. J. Lockwood, Eds., Si Photonics, New York: Springer, 2003, p. 177.

120. L. Tsybeskov, "Light Emission in Three-dimensional Si/SiGe Nanostructures Physics and Applications," ECE Transactions, vol. 25, pp. 67-91, 2009.

121. J. Stangl, V. Holy, and G. Bauer, "Structural properties of self-organized semiconductor nanostructures," Rev. of Modern Phys., vol. 76, pp. 725-783, 2004.

122. E.–K. Lee, L. Tsybeskov, and T. I. Kamins, "Photoluminescence thermal quenching in three-dimensional multilayer Si/SiGe nanostructures," Appl. Phys. Lett., vol. 92, p. 033110, 2008.

123. J.-M. Baribeau, D. J. Lockwood, and R. L. Headrick, "Nature and evolution of interfaces in $Si/Si_{1-x}Ge_x$ superlattices," J. Electron. Mat., vol. 24, pp. 341-349, 1995.

124. N. Modi, D.J. Lockwood, X. Wu, J.-M. Baribeau, and L. Tsybeskov, "Excitation wavelength dependent photoluminescence in structurally non-uniform Si/SiGe-island heteroepitxial multilayers," J. Appl. Phys., vol. 111, p. 114313, 2012.

125. http://www.horiba.com/us/en/scientific/products/raman-spectroscopy/raman-systems/research-raman/details/u1000-142/ (accessed on 12/05/2014)

126. http://sales.hamamatsu.com/assets/pdf/parts_R/R943-02_TPMH1115E07.pdf (accessed on 12/05/2014)

127. J. H. Neiss, "System and method for automated baseline correction for Raman spectra," US 7337066 B2, Feb 26, 2008.

128. H.-Y. Chang, L. Tsybeskov, A. Sirenko, D. J. Lockwood, J.-M. Baribeau, X. Wu, and M. W. C. Dharma-wardana, "Thermal conductivity of silicon/germanium nanostructures," Mat. Res. Soc. Symp. Proc., vol. 1145, 2009.

129. H.-Y. Chang and L. Tsybeskov, in Silicon Nanocrystals: Fundamentals Synthesis and applications, L. Pavesi and R. Turan, Eds.,Weinheim: Wiley-VCH, 2010, p. 105.

130. S. M. Sze, Physics of Semiconductor Devices, New York: John Wiley and Sons, 1981.

131. M. Holtz, W. M. Duncan, S. Zollner, and R. Liu, "Visible and ultraviolet Raman scattering studies of $Si_{1-x}Ge_x$ alloys," J. Appl. Phys., vol. 88, pp. 2523-2528, 2000.

132. L. Tsybeskov, E.-K. Lee, H.-Y. Chang, B. V. Kamenev, D. J. Lockwood, J.-M. Baribeau, and T. I. Kamins, "Three-dimensional silicon-germanium nanostructures for CMOS compatible light emitters and optical interconnects," Adv. Opt. Technol., vol. 2008, art. no. 218032, 2008.

133. G. Pernot, M. Stoffel, I. Savic, F. Pezzoli, P. Chen, G. Savelli, A. Jacquot, J. Schumann, U. Denker, I. Mönch, Ch. Deneke, O. G. Schmidt, J. M. Rampnoux, S. Wang, M. Plissonnier, A. Rastelli, S. Dilhaire, and N. Mingo, "Precise control of thermal conductivity at the nanoscale through individual phonon-scattering barriers," Nature Materials, vol. 9, pp. 491-495, 2010.

134. A. Picco, E. Bonera, E. Grilli, M. Guzz, M. Giarola, G. Mariotto, D. Chrastina, and G. Isella, "Raman efficiency in SiGe alloys," Phys. Rev. B, vol. 82, p. 115317, 2010.

135. R. Schorer, G. Abstreiter, H. Kibbel, H. Presting, C. Tserbak, and G. Theodorou, "Optical anisotropy of SiGe superlattices: Resonant Raman scattering in in-plane geometry," Solid State Commun., vol. 93, pp. 1025-1029, 1995.

136. S. A. Mala, L. Tsybeskov, D. J. Lockwood, X. Wu, and J.-M. Baribeau, "Fast and intense photoluminescence in a SiGe nano-layer embedded in multilayers of Si/SiGe clusters" Appl. Phys. Lett., vol. 103, p. 033103, 2013.

137. B. V. Kamenev, E.-K. Lee, H.-Y. Chang, H. Han, H. Grebel, L. Tsybeskov, and T. I. Kamins, "Excitation-dependent photoluminescence in Ge/Si Stranski-Krastanov nanostructures," Appl. Phys. Lett., vol. 89, p. 153106, 2006.

138. B. V. Kamenev, L. Tsybeskov, J.-M. Baribeau, and D. J. Lockwood, "Coexistence of fast and slow luminescence in three-dimensional $Si/Si_{1-x}Ge_x$ nanostructures," Phys. Rev. B, vol. 72, p. 193306, 2005.

139. B. V. Kamenev, L. Tsybeskov, J.-M. Baribeau, and D. J. Lockwood, "Photoluminescence and Raman scattering in three-dimensional $Si/Si_{1-x}Ge_x$ nanostructures" Appl. Phys. Lett., vol. 84, pp. 1293-1295, 2004.

140. O. G. Schmidt and K. Eberl, "Multiple layers of self-asssembled Ge/Si islands: Photoluminescence, strain fields, material interdiffusion, and island formation," Phys. Rev. B, vol. 61, pp. 13721-13729, 2000.

141. S. Fukatsu, Y. Mera, M. Inoue, K. Maeda, H. Akiyama, and H. Sakaki, "Time-resolved D-band luminescence in strain-relieved SiGe/Si," Appl. Phys. Lett., vol. 68, pp. 1889-1891, 1996.

142. E.-K. Lee, D. J. Lockwood, J.-M. Baribeau, A. M. Bratkovsky, T. I. Kamins, and L. Tsybeskov, "Photoluminescence dynamics and auger fountain in three-dimensional Si/SiGe multilayer nanostructures," Phys. Rev. B, vol. 79, p. 233307, 2009.

143. B. Ohnesorge, M. Albrecht, J. Oshinowo, A. Forchel, and Y. Arakawa, "Rapid carrier relaxation in self-assembled $In_xGa_{1-x}As/GaAs$ quantum dots," Phys. Rev. B, vol. 54, pp. 11532-11538, 1996.

144. A. Zrenner, B. Fröhlich, J. Brunner, and G. Abstreiter, "Time-resolved photoluminescence of pseudomorphic SiGe quantum wells," Phys. Rev. B, vol. 52, pp. 16608-16611, 1995.

145. I. Kuskovsky, G. F. Neumark, V. N. Bondarev, and P. V. Pikhitsa, "Decay dynamics in disordered systems: Application to heavily doped semiconductors," Phys. Rev. Lett., vol. 80, pp. 2413-2416, 1998.

146. D. G. Thomas, J. J. Hopfield, and W. M. Augustyniak, "Kinetics of radiative recombination at randomly distributed donors and acceptors," Phys. Rev., vol. 140, pp. 202-220, 1965.

147. J. R. Eggert, "Bivalent nearest-available-neighbor distribution in n dimensions: A Monte Carlo calculation," Phys. Rev. B, vol. 29, pp. 6664-6669, 1984.